Constraint and anisotropy during sintering of a LTCC material

Vom Fachbereich Material- und Geowissenschaften
der Technischen Universität Darmstadt

zur Erlangung des akademischen Grades
Doktor - Ingenieur
(Dr.-Ing.)

genehmigte Dissertation von
Jean-Baptiste Ollagnier
aus Saint-Chamond, Frankreich

Referent:	Prof. Dr.-Ing. J. Rödel
Korreferent:	Prof. Dr. rer. nat. Dr. h. c. R. Riedel

Tag der Einreichung:	21. Mai 2008
Tag der mündlichen Prüfung:	25. Juni 2008

Darmstadt 2008
D17

Acknowledgements

First, I would like to thank Prof. Dr. Rödel to give me the opportunity to work in his group to complete this thesis. I am particularly grateful for the supervision of my work and the degree of freedom he left me. He has been a great support since he always encouraged me despite my (temporary) frustrations.

I would like to thank Prof. Dr. Riedel to accept to be the second examiner for this thesis.

I would also like to thank Dr. Guillon who in a way acted as my second adviser. His precious help guided me during this thesis and he has always been open for all kind of discussions.

I would also like to acknowledge Prof. Dr. Green to welcome me at Penn State University and for the very friendly and interesting discussions.

I am grateful for the assistance provided by: Emil for all kind of technical problems, Herbert for his very precise work, Jean-Christophe for the help for the XRD measurements and Roswita for her patience with the paperwork I provided.

I would also like to thank my two student helpers: Kwang-Jin and Aldin who prepared and polished samples.

I am very grateful to the NAW members for the very nice work atmosphere especially Doru, Ludwig, Ender, Alain, Wook, Gundel, Johanna, Nina, Silke, Ilona, Jami, Julia, Thomas, Thorsten, Daniel, Jochen, Gerrit, Klaus, Ingo and my roommates, Stefanie (who improved a lot my German), Ruzhong (for enlivened discussion on international politics), Thorsten and Markus (for keeping me up to date on the "Bundesliga"). I am very grateful to the research visitors for the great international atmosphere and the great Basket-ball games: Julius, Simonas, Andrius, Jorge and Enzo. I also would like to thank my very good Korean friend Jaemyung for the helpful scientific discussions and the

nice time we had together. I am very grateful to Calista, Andrea, Amber, Josh, Mike, Kyle and Walter to integrate me at Penn State University. I also would like to thank other Mawis like Aiswarya, Azad and Rodrigue for the nice coffee "without coffee" breaks.

Je voudrais remercier ma famille de m'avoir poussé à continuer mes études et de m'avoir soutenu où que je sois. Merci d'avoir toujours été là!

Finally, I would like to thank my girlfriend So-Youn for her patience and kindness. She has been always positive and has known how to put her touch of fantasy in my life!

Contents

Chapter 1

Introduction

Sintering is a thermal process by which adjacent particles are brought together by reducing interfacial area and surface energies leading to densification. It is a crucial step for fabrication of a ceramic component since it is usually during sintering that the properties of the final products are controlled. The aim is to produce sintered parts with reproducible and if possible designed microstructure through control of sintering parameters. These requirements and control of the final shape are fundamental especially in the microelectronic industry.

Miniaturization of mobile communications equipment and multimedia applications such as mobile phones, laptops, video game consoles, MP3 players, digital cameras and photo printers require the use of components with ever more compact dimensions. Thus, during the two last decades, the demands on material and electrical packaging of modules have increased greatly, leading to fruitful developments in materials science of electrical packaging. Low temperature co-fired ceramic (LTCC) technology is among the most promising approaches to miniaturization of electronics packaging. It exploits both the ceramic and metallic benefits and a reliable screen-printing technology, with the unique ability to integrate a broad variety of components (such as capacitors and inductors) into a very compact arrangement. Nowadays, the LTCC technology is widely used in wireless applications, especially in the radio frequency field and the market size is significantly expanding: from $757 million in 2002, going to $833 million in 2003 and to $1,885 million in 2007. However, there are still challenges to be met: for instance, to better control the shrinkage and the dimensional variations during processing.

During the sintering process of LTCC, non-densifying layers and uniaxial compressive stresses are used to constrain the in-plane shrinkage of LTCC layers, thereby improving dimensional tolerances of the fired layers. Internal stresses develop during the densification process as a result of mismatch in the sintering rates within the component. Built-in stresses lead to reduced shrinkage rates and changes in the microstructure of the constrained layers.

Although sintering of constrained films is a common manufacturing process, there is still a lack of understanding of what the mechanisms involved in the sintering process are and how they are affected under constraint. This work is performed to obtain some of the needed experimental data and provide further insight into the densification of constrained films. Knowledge gained from this study will help engineers to optimize the design and manufacturing process that in turn will lead to higher production yields, lower costs and more reliable devices.

This work is divided into five sections.

In chapter 2, an overview of the LTCC technology is provided. Fundamental and theoretical aspects of sintering and constrained sintering are further given in details. The continuum mechanical description of sintering which is used to characterize macroscopically the densification behavior under constraint is presented.

The details of the experimental procedures performed in this work can be found in the third chapter. Sample preparation, sintering experiments and the different ways of sample characterization are described.

Then, the fourth chapter deals with the results. Sintering parameters are measured as function of density and the densification behavior under geometrical constraint is characterized. The goal is to understand how tensile or compressive loadings influence the densification behavior. Furthermore, different viscous and elastic constraining substrates are used and models are developed to take into account the mechanical properties of such materials. Two different study cases are distinguished: sintering of asymmetric and symmetric laminates.

Results are further discussed in the fifth chapter. Model predictions are compared to experimental observations. Particular attention is paid on the anisotropy development within the microstructure. Correlation between microstructure and the macroscopic sintering parameters is then highlighted.

A brief summary as well as an outlook are given at the end.

Chapter 2

Theory

2.1 LTCC technology

Nowadays, there is an increased demand on the market for use of mobile applications and the trend is going towards miniaturization.[1] As Tummala has shown,[2] the computer system performance depends on two major components: semi-conductor and packaging. It is then of high importance to improve packaging properties. Considering the important characteristics of ceramic substrates (dielectric constant, wiring density, metallization, thermal-expansion match to silicon, dimensional control and mechanical strength), LTCC technology is the most promising candidate.

LTCC provides a multilayer ceramic technology and presents many advantages compared to other thick film or high temperature co-fired ceramic (HTCC) technologies. The sintering temperature of the ceramic materials is below 900 °C and thus they can be co-fired with low-resistive conductor materials such as silver, copper, or gold[3] instead of molybdenum or tungsten for HTCC technology. Silver, gold and copper have a low melting temperature (961 °C, 1062 °C, and 1083 °C, respectively) but higher than the sintering temperature. Passive elements, such as resistors, capacitors and inductors are embedded into the ceramic package.[4] Resistors are processed with the help of special pastes, which have to be printed on the tape just like conductor lines and have to be post- or co-fired. Capacitors and inductors are built only with the help of special forms of the conductor lines (plates, spoils). Typically, in a LTCC module, there are 150-300 passive components with 50-70% capacitors, 20-40% resistors and 10% inductors.[5] Hence the size of the components decreases: the integration of passive components is made in a 3D structure instead of arranging the components in a 2D structure (figure 2.1). LTCC technology presents also a good flexibility and reliability as well as a low cost due to the production process.[6] Another advantage is that LTCC materials have a tunable range of properties, like dielectric constant and thermal expansion coefficient.[6] For example, the properties vary by changing the proportion of the ceramic filler in the glass matrix phase. This feature makes the LTCC substrate very attractive for various integrated packaging.

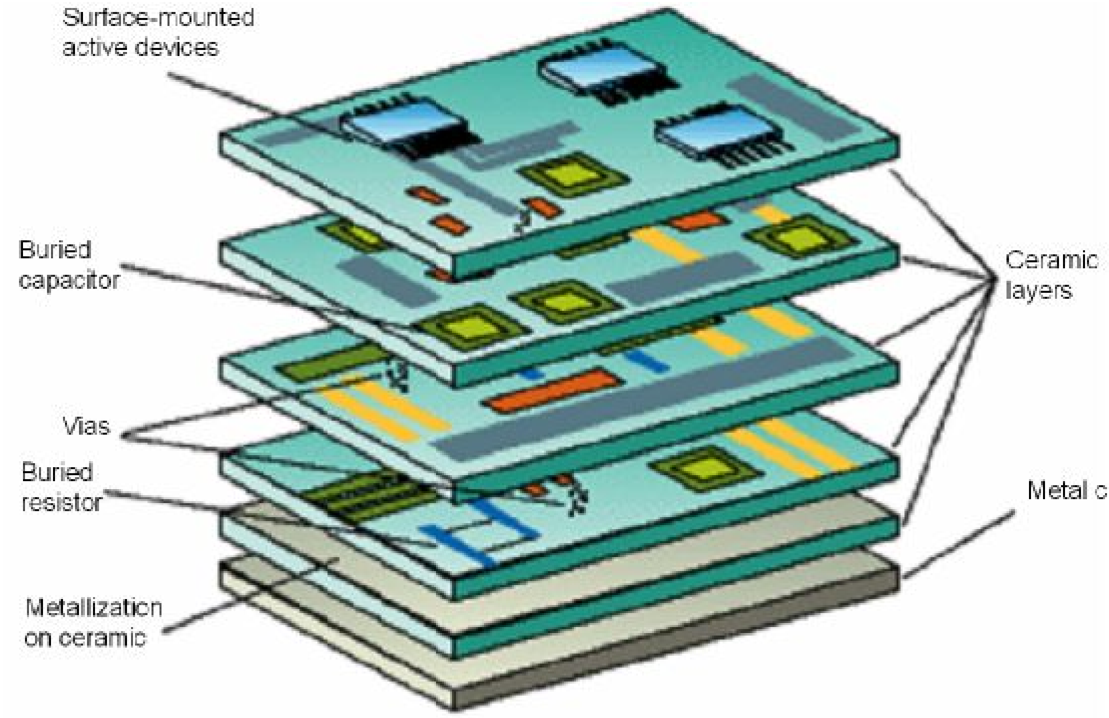

Figure 2.1: LTCC module - www.electronicproducts.com.

LTCC materials have better thermo-mechanical properties than polymers PCBs (printed circuit boards) and thus can be used in hostile environments.

A disadvantage of LTCC materials is that they have a low thermal conductivity (2-6 $W.m^{-1}K^{-1}$). One technological solution to cope with this problem is to integrate thermal vias into the structure to bring out the heat.[7;8] Moreover, the main difficulties in the development of new LTCC materials are related to their sintering behavior and their chemical compatibility.[9] The number of different phases should be kept as low as possible in order to limit the problems of chemical compatibility between the different phases; whereas, the misalignment of the different layers influences the performance of the package. Today, the main challenges are to increase the variety of material systems, to achieve tighter dimensional control, smaller metal dimensions (striplines, vias) and to optimize the process.

2.1.1 Processing

Processing of LTCC components follows different steps (figure 2.2). The preparation of the slurry for tape casting is first made. The raw powders are milled in presence of a solvent and later organics are added in order to reach the mechanical requirements for green body handling. The slurry is then tape cast and the green sheets are manipulated: via forming is typically done by punching or drilling, via filling and conductor printing is done by screen printing. Good rheology and surface energies are two major factors that influence the printing properties (the viscosity of the paste can be controlled by the

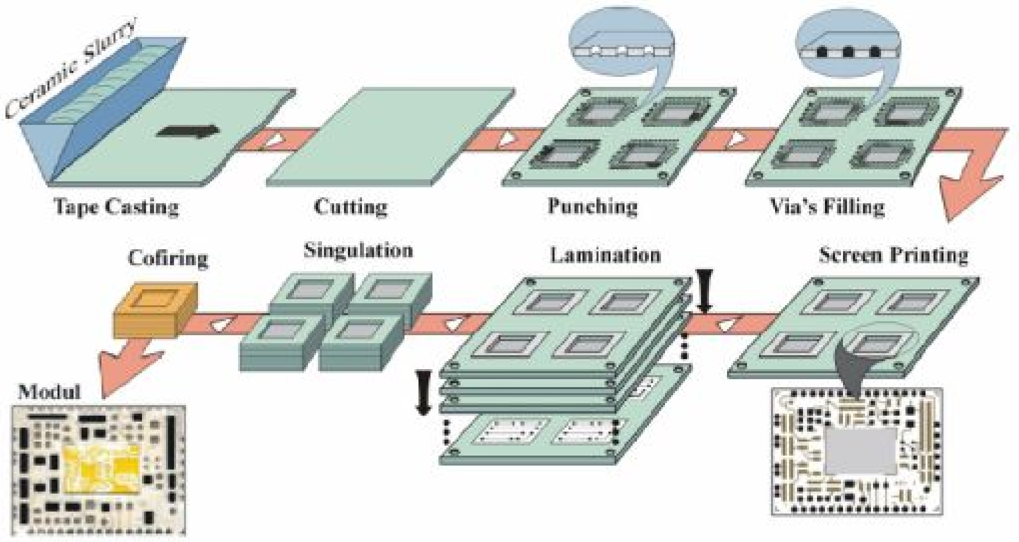

Figure 2.2: LTCC processing flow chart.

inorganic particle such as silica present in the paste).[7] After that, the different layers are laminated under controlled pressure and temperature. The laminate is cut to its final size. Burn-out of the organic additives and co-firing is made in a single step. Sintering temperature profile is well defined to control the glass crystallization. It is also important that sintering does not occur below 700 ° C. Any densification below this temperature is undesirable because carbon needs to be removed and any residual carbon would affect the dielectric constant and thus the properties of the package.[2] Finally, the LTCC module is connected with chips and board with the help of different technologies. For example, the chip-to-LTCC interconnection can be done by wire bonding or flip chip bonding whereas the LTCC-to-board interface can be done by ball grid array.[10]

Processing of LTCC permits that each layer of the circuit is processed in parallel before being laminated into the final structure. Thus, a flaw in one step of the process may require scrapping only the affected print layer and not the whole module.[8;11]

2.1.2 Applications and properties

LTCC technology is used mainly in microelectronic packaging in the radio frequency (RF) field:[1]

- Mobile telecommunication devices (0.9-2 GHz)
- Geographical positioning systems (1.6 GHz)
- Wireless networks such as Bluetooth (2.4 GHz)
- Broad band access connection system (5.8-40 GHz)

A low dissipation factor (inversely proportional to the quality factor), an appropriate permittivity (dielectric constant) and a temperature coefficient of the resonance frequency near zero are important. These three properties define the quality and the size of the RF component. Permittivity is a significant property since the propagation speed of the electrical signal is inversely proportional to the square root of the permittivity. Thus, low-dielectric-constant ceramics will have higher performances. A low dissipation factor will permit to design RF filters with low losses. Although the main losses in the frequency range from 4 to 44 GHz are conductive losses, the relative importance of dielectric losses increases as function of frequency.[10] Finally, the temperature coefficient of the resonance frequency should be kept as close as possible to 0 ppm/ °C for a stable frequency response of the integrated elements such as resonators and filters, at its operational temperature.[12;13] The coefficient of thermal expansion (CTE) should also be chosen to match closely the value of the mounting board and chip (CTE of silicon in the most common case).

LTCC technology is not only limited to packaging applications. LTCC materials can also be used for meso-system technology as sensors, actuators.[14;15] It has been shown that LTCC materials could replace silicon in Micro-Electro-Mechanical Systems (MEMS) in the meso scale range (from 10 to several 100 microns). LTCC materials are suitable since they present the right thermal, mechanical and electrical properties for these applications and they are inexpensive to process.[14;15]

2.1.3 Materials

In order to reach the desired properties, LTCC materials need to meet several requirements. Properties will vary strongly with phase composition as well as microstructure of the material. For example, the degree of crystallization of the glass phase is an important parameter as it affects both electrical and mechanical properties: the presence of the glass phase in the LTCC tape necessarily reduces the quality factor;[16–18] whereas, if the degree of crystallinity is high, it would result in good mechanical properties. Other parameters such as porosity can influence the dielectric properties of the material: low levels of porosity ($<$ 5 vol%) significantly decrease the permittivity, but do not affect the dielectric losses.[17]

LTCC materials contain a broad range of materials, as the functions these materials can fulfill are quite different. In signal propagation related cases, materials require a low permittivity, while for capacitors applications, the permittivity must be high ($>$20).[10;16;18] In any case, to be compatible with the LTCC technology, the materials should meet the following requirements: to have a low sintering temperature (below 900 °C) and to be compatible with the electrode pastes.

In order to extend the range of applications, a large variety of materials is used in the LTCC technology. Figure 2.3 illustrates the different LTCC material systems. Most

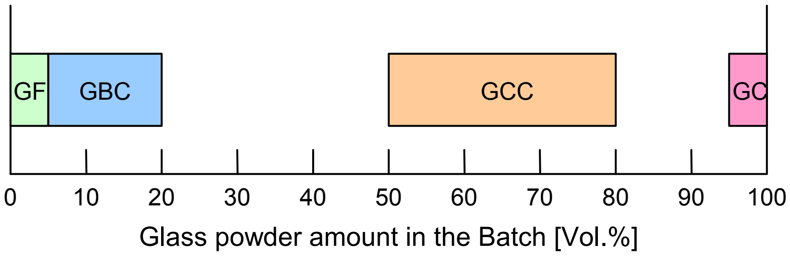

Figure 2.3: LTCC material systems - GF: glass free ceramics; GBC: glass bonded ceramics; GCC: glass ceramic composites; GC: glass ceramics.[20]

of the current commercial LTCC materials possess an amount of glass higher than 50 vol.%.[19] They can be classified in glass + ceramic (or glass ceramic composite (GCC) – e.g. DuPont 951) and glass-ceramic (GC) (or crystallizable glass – e.g. Heraeus CT 700). Two other classes of LTCC can be distinguished: glass free ceramics (GF) and glass bonded ceramics (GBC).

GCC is the most common LTCC material. It is composed of a ceramic filler (generally, Al_2O_3) in a glass matrix (generally a borosilicate glass). The ceramic particles limit the glass flow by acting as a physical barrier. They also inhibit sintering of the glass and thus facilitate better burnout of the organics.[21] During the co-firing process, the ceramic filler is partially dissolved in the glass melt which will later crystallize.

GC are normally suitable for 20–30 GHz applications, such as in military and aerospace applications, where low loss is required.[12] They are defined as ceramics formed by controlled crystallization of glass resulting in materials of high crystallinity after firing. The most common GC is the crystallizable cordierite. The glass is sintered to full density in the glassy state and subsequently crystallized to yield glass-ceramics with α - cordierite as the principal crystalline phase.[22] The dielectric constant of IBM GC has a value of 5. Another glass system can be used for GC: a calcium aluminosilicate glass of composition $CaAl_2Si_2O_8$, which crystallizes as anorthite.

With respect to both mechanical and dielectric properties, the presence of glass is not desirable in the final product. It is then of high interest to study potential LTCC materials without glass content (**GF**). Moreover, it is of great importance to reduce the number of phases present in the LTCC modules in order to avoid chemical reactions between these phases.[9] The principal difficulty encountered is then to meet the requirement of a low sintering temperature.[9;23] Possible solutions to produce glass-free ceramics are to use calcium silicates, germinates and tellurates. ZnO-TiO_2 with B_2O_3 (1 wt%) and CuO (0.5 wt%) has been also studied.

GBC is a mixture of low-melting glass and ceramic filler, but contrary to GCC, the glass is also designed to react with the filler ceramic at the sintering temperature to form high-Q crystalline phases. Titanates are normally used: the dissolution of TiO_2 in the glass and subsequent formation of titanium compounds can lead to a very low temperature coefficient of the resonance frequency.

Finally, the different materials can be assembled in one package. When at least two different LTCC materials are present in a single module, it is called *Advanced LTCC*. An example of a two-material multilayer consists of an inner material with medium permittivity and outer layers of low permittivity. Such a combination enables the integration of miniaturized microwave filters in a LTCC module.[19;24]

2.2 Fundamentals of sintering

2.2.1 Generalities

Sintering is the reduction in interfacial area by atomic transport mechanisms. Porous bodies have interface and surface energies. During sintering both energies will tend to minimize: area can be reduced by smoothing irregularities and/or closing pores. Closing pores increases density whereas smoothing surface does not. Alternate paths for matter transport during sintering may occur: viscous flow, surface diffusion, lattice diffusion, grain boundary diffusion, evaporation/condensation. The activation energy is commonly brought to the porous body by heating. An external mechanical load can be applied to enhance densification (sinter-forging, hot isostatic pressing, etc...).

Sintering can be classified into several processes:

- Sintering that proceeds by **solid-state diffusion**. Polycrystalline materials usually sinter by this process.
- Amorphous materials sinter by viscous flow and thus are considered to undergo **viscous sintering**. The sintering temperature is above the glass transition.
- When a liquid phase is present during sintering (a few percent in volume), the sintering process is known as **liquid phase sintering**. Liquid phase sintering can be used to assist solid state sintering. It enhances densification rates as the liquid phase provides a path for rapid transport, and it can produce specific grain boundary properties.

Every sintering process can be divided into three stages: initial stage, intermediate stage and final stage (figure 2.4). In the first stage, neck growth between the particles occurs in the first 5% of densification. In the intermediate stage, the pores are still interconnected. This stage takes place up to 92-94% of the theoretical density. In the final stage, the pores are isolated and disappear until the theoretical density is reached. Sintering rate depends on two parameters: temperature (which controls the diffusion rate) and particle size (which controls the diffusion length scale).

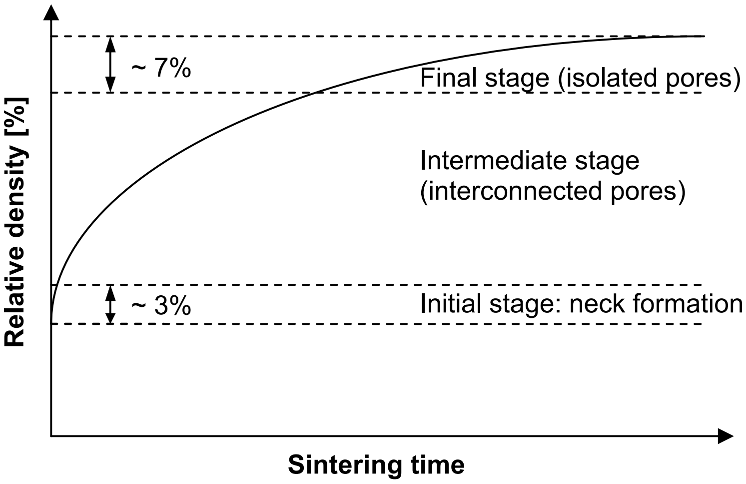

Figure 2.4: Schematic showing the densification curve of a powder compact and the three sintering stages.

2.2.2 Viscous sintering

2.2.2.1 Viscous sintering of glasses

Glasses are non-crystalline solids obtained by progressive and continuous freezing of supercooled liquids with retarded crystallization. They do not show any regular long range order of atoms positions.

Viscous sintering takes place when a compact of glassy particles is heated to a temperature high enough so that the glass flows under the action of surface tension forces. The temperature for viscous sintering should be determined so that the surface tension is high and the viscosity is low, i.e. when the glass reaches its lower viscosity without crystallizing.[25] One of the characteristics of sintering of glass particles is that it occurs at a relatively low temperature: the particles are already coalescing at one-half to two-third of the melting temperature (softening point of $10^{6.6}$ Pa.s). This is due to the fact that the glassy phase does not have any regular structure. Rearrangement of the former structure is then easier than in crystalline materials where diffusion takes place. At the sintering temperature, the material behaves like an incompressible Newtonian viscous fluid. One should be aware that because of too low a viscosity, slumping can occur only by the effect of gravity.

The driving force for the flow is the excess of free surface energy of the porous glass compared to the same quantity of a fully dense glass. In other words, viscous flow is the kinetic path through which the surface area is minimized.[26;27] Mathematical models of viscous sintering are based on the hypothesis made by Frenkel:[28] the energy dissipated in viscous flow is equal to the energy gained by reduction in surface area. Frenkel[28] applied this energy balance to describe the early stage of coalescence of two equal spherical particles (figure 2.5) and derived the following equation:[28]

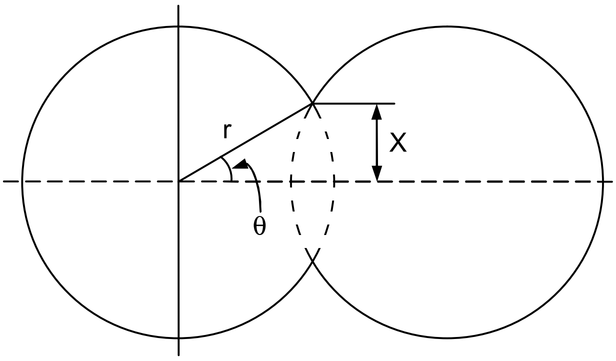

Figure 2.5: Schematic illustration of Frenkel's model.

$$\left(\frac{X}{2r}\right)^2 = \sqrt{\frac{3\gamma_s t}{2\eta r}} \tag{2.1}$$

where X is the neck radius, r the radius of the particle, γ_s is the glass-vapor surface energy, t is the isothermal sintering time and η is the viscosity.

Rewriting this equation, the relative density is given by:

$$\frac{\gamma_s n^{1/3}}{\eta}(t - t_0) = \frac{8}{3}\left(\frac{3}{4\pi}\right)^{1/3} P^{1/3}\left(1 - \frac{\rho}{\rho_0}\right) \tag{2.2}$$

where P is the number of pores per particle and n is the number of closed pores/volume of solid phase.

We can notice that the initial stage of sintering of glass particles is similar to solid state sintering as neck growth occurs due to viscous flow.[29]

In the intermediate stage, densification will occur as pores shrink. In a glass system, it can be assumed that gas, which is trapped in pores, can diffuse rapidly through the interconnected pores. The pore shrinkage is proportional to γ_s/η. As the viscosity is strongly dependent on temperature whereas γ_s is weakly dependent on temperature, pore shrinkage is enhanced by temperature. Scherer's cubic array's model is appropriate for this sintering stage[27;30] though it was developed for viscous systems with very low density such as gels and waveguide preforms (fig. 2.6).[31] Scherer investigated different geometries for his model and showed that the cell shape did not have any strong influence on the predicted densification behavior.[30] For densities higher than 94.2% the structure can no longer be described as an array of cylinders as the cell contains a closed pore.

For this model, the relative density is given by:

$$\frac{\gamma_s n^{1/3}}{\eta}(t - t_0) = -\frac{2}{\alpha}\left(\frac{1}{2}\ln\frac{\alpha^2 - \alpha y + y^2}{(\alpha + y)^2} + \sqrt{3}tan^{-1}\frac{2y - \alpha}{\alpha\sqrt{3}}\right) \tag{2.3}$$

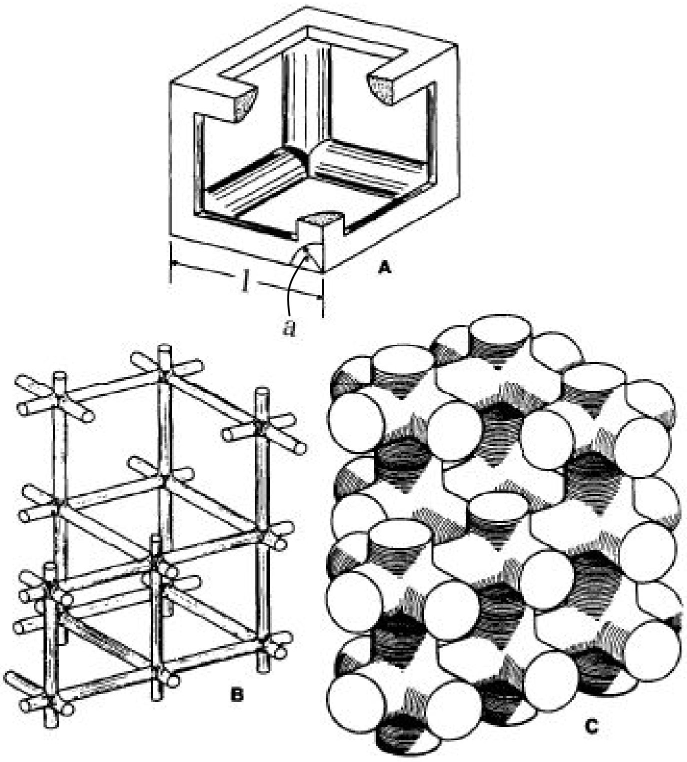

Figure 2.6: Microstructural model from Scherer consisting of cylinders in a cubic array: (A) Unit cell showing edge length, l, and cylinder radius, a; (B) model of low-density microstructure ($\rho = 0.05$); (C) model of microstructure with $\rho = 0.50$.

where $\alpha = \left(8\sqrt{2}\right)^{1/3}$, $y = \sqrt[3]{(3\pi/x) - 8\sqrt{2}}$, $x = a/l$ and $\rho = 3\pi x^2 - 8\sqrt{2}x^3$.

In the final stage, closing of the pores occurs and the densification rate of uniform spherical pores is described by the MacKenzie-Shuttleworth model.[32] The model approximates a pore with its surrounding matrix by a spherical shell (figure 2.7). For this model, the relative density is given by:

$$\frac{\gamma_s n^{1/3}}{\eta}(t - t_0) = f(\rho(t)) - f(\rho_0) \tag{2.4}$$

where,

$$f(\rho) = -\frac{2}{3}\left(\frac{3}{4\pi}\right)^{1/3}\left(\sqrt{3}tan^{-1}\left(\frac{2(1/\rho - 1)^{1/3} - 1}{\sqrt{3}}\right) + \frac{3}{2}log\left[(1-\rho)^{1/3} + \rho^{1/3}\right]\right) \tag{2.5}$$

On figure 2.8 the densification behavior for the three models is plotted. Models by Scherer[31] and MacKenzie-Shuttleworth[32] do not depend on initial density whereas Frenkel's model is strongly dependent on initial density. There is a good agreement of Scherer[31] and MacKenzie-Shuttleworth's model[32] in spite of the different microstructural geometries used.

As indicated in figure 2.8, to have a complete densification of a sintering body with

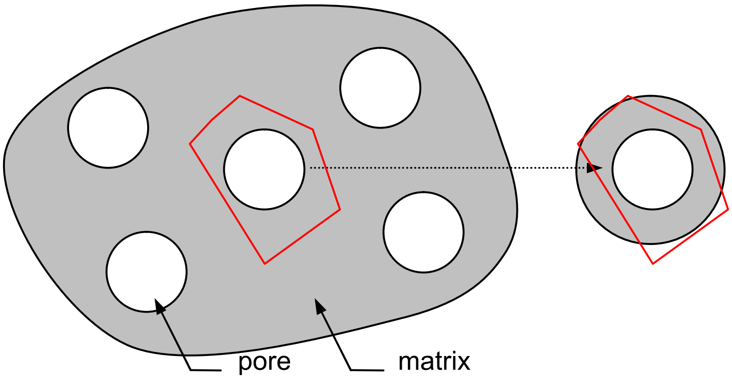

Figure 2.7: Geometrical model from MacKenzie and Shuttleworth.

an initial density of 0.52, the required time is:

$$t \approx 1 \times \frac{\eta}{\gamma_s n^{1/3}} \approx \frac{\sqrt[3]{4\pi}\eta r}{\gamma_s} \tag{2.6}$$

A smaller particle size and lower viscosity lead to shorter sintering times. However, the particle size effect ($t \propto r$) is less significant than for polycrystalline materials where the required time is proportional to r^3 or r^4.[29]

In order to describe viscous sintering over the whole range of density, Pascual *et al.* proposed the clusters model, which allows both Frenkel[28], and MacKenzie-Shuttleworth[32] models to occur simultaneously.[33] Sintering is divided into three stages: a pure Frenkel stage, a mixed Frenkel/MacKenzie-Shuttleworth stage and finally a pure MacKenzie-Shuttleworth step. The model considers the overall shrinkage as the sum of the cluster's shrinkage. Each cluster could be in one of the three stages of the sintering steps. The model is based on an experimental fact: small particles preferentially cluster in the open spaces left by larger particles and sinter faster.[33] The model was then upgraded to take into account the effect of embedded rigid fibers[34] and concurrent crystallization.[27;35]

Numerous issues about numerical simulation of viscous sintering have been published.[36–42] Simulations are also based on the hypothesis made by Frenkel:[28] the energy dissipated in viscous flow is equal to the energy gained by reduction in surface area. Jagota *et al.*[36] modeled viscous sintering of two initially spherical particles and the surface tension generates viscous creep. A finite element method was used to show that the deformation is localized in a small region near the neck and the surface velocities are outward radial everywhere. Van de Vorst used a numerical approach to simulate viscous sintering with a two-dimensional unit cell.[38] He showed that the smallest pores vanished, followed by the larger ones. Interestingly, pores, which have a large concave boundary part, initially grew and further shrank. However, pore boundary length decreased as time evolved.

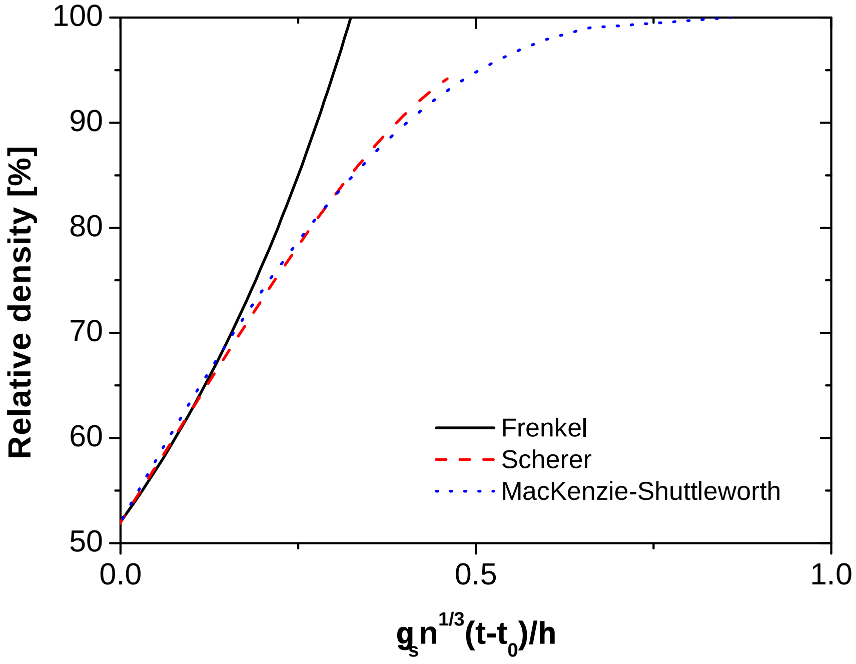

Figure 2.8: Relative density vs. time for Frenkel, Scherer and MacKenzie-Shuttleworth models. The starting relative density is $\rho_0 = 0.52$ (simple cubic packing of spheres) and corresponds to the time $\gamma_s n^{1/3}(t - t_0)/\eta = 0$. For Frenkel's model, $P = 1$.

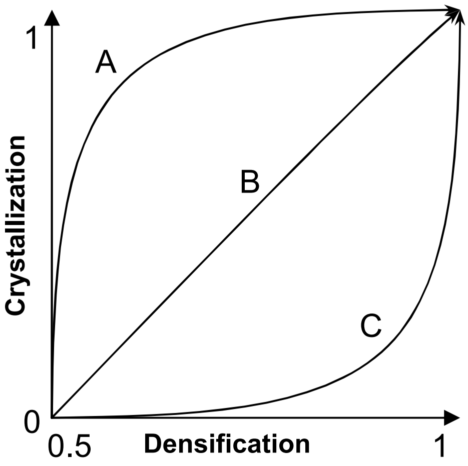

Figure 2.9: Sintering trajectory - Densification and crystallization.

2.2.2.2 Viscous sintering with concurrent crystallization

During sintering of glass material, crystallization can occur by different processes: bulk crystallization or surface crystallization (homogeneous or heterogeneous crystallization, respectively). Heterogeneous crystallization is most common. Wittman and Zanotto[43] showed for anorthite glass that the nucleation occurred along surface scratches. It was also observed that the presence of a crystalline second phase enhances the heterogeneous nucleation rate of the glass.[44]

Different paths can be followed as densification and crystallization could occur in sequence or in combination (figure 2.9). As the viscosity of a polycrystalline material is much higher than the viscosity of an amorphous one for the same composition, densification of a polycrystalline material will be significantly more difficult than the amorphous phase. The crystallized surfaces slow down the densification kinetics as they do not flow and as a consequence, viscous flow is hindered. They play the same role as pre-existing crystalline particles: only glass-glass contacts contribute to sintering.[27] In other words, trajectory C should be preferred to trajectory A and B (figure 2.9). Note that, if crystallization occurs, viscous sintering will not be anymore the sintering process but solid or liquid phase sintering processes could occur. Another point to take into account is that non-stoichiometric crystallization (the crystal composition differs from the glass composition) induces variations in the glass composition and then affects properties such as viscosity and surface energy.[27] The driving force for crystallization depends to a great extent on temperature but can also be enhanced by a load.[45] Note that the presence of crystalline particles promotes crystallization. Prado *et al.* showed that smaller particle size and better surface quality (no pre-existing crystals) favor sintering over crystallization.[27] In order to avoid crystallization, the sintering temperature should be high enough (apart from the crystallization temperature range) and should be reached quickly as the material is susceptible to crystallization during the heating path.[27;44]

2.2.2.3 Viscous sintering of glass-ceramic composites

Crystalline ceramic particles are added to a glass matrix since it can cause a significant improvement of mechanical properties (bending strength, microhardness, and fracture toughness) compared to the un-reinforced glass-ceramic.[46] Mechanical properties are improved since cracks are deflected by the presence of the ceramic particles. Ceramic particles can also improve dielectric properties such as in LTCC systems.[47]

Ewsuk[48] proposed to describe the densification behavior of a glass-ceramic composite as non-reactive liquid phase sintering (NLPS) in three stages. In the first stage, the glass becomes fluid and infiltrates the fine capillary pore structure of the ceramic filler. Both solid-liquid and solid-vapor interfaces are present in the composite and lead to a force imbalance, which induces particle rearrangement (2^{nd} stage). For the final stage of sintering, the driving force is defined by the Laplace equation and is driven by viscous flow.

The viscosity of the glass-ceramic composite, η_{GCC} can be related to the viscosity of the glass η_{Glass}:

$$\eta_{GCC} = \left(1 + \frac{\zeta v_s}{1 - \dfrac{v_s}{v_{smax}}} \right)^2 \eta_{Glass} \tag{2.7}$$

where ζ is a constant that increases with decreasing filler particle size, v_s is the volume fraction of particles and v_{smax} is the maximum fractional packing density of the particles (for a random packing of spherical particles, $v_{smax} = 0.64$[49]). The viscosity increases as the volume fraction of particles increases.

It was experimentally observed that if filler particle size increases, shrinkage rate increases. Several explanations were proposed: (i) glass redistribution occurs faster as pores are expected to be larger (ii) viscosity decreases so that the third stage is favored and (iii) for smaller particle size, the contact particle/glass is larger; hence there is less glass available for glass redistribution. Finally, it was shown that η_{Glass} controls the densification during the initial and intermediate stage whereas, η_{GCC} controls densification during the final stage. The last stage is by far the slowest stage and if the volume fraction of particles is high (η_{GCC} is large), the viscosity of the glass should be low in order to reach high densities.[50]

Jagota *et al.*[37] simulated viscous sintering of coated particles with glass. This case is similar to a glass particle composite with a wetting angle of the glass of 0 degree. It was shown that the sintering rate decreases as the particles approach each other and is limited by flow into the gap between the particles.

However, Kemethmüller *et al.*[51] showed that the wetting of the alumina particles is not necessary to obtain fully dense samples. In this case, the first and second stage of Ewsuk's model[48] are left out and it is assumed that the viscous flow is the predominant mechanism.

2.3 Continuum mechanical description of sintering

2.3.1 Theory

The sintering kinetics of porous bodies are not only determined by the properties of the powder particles and the nature of their interaction. Macroscopic factors can interfere such as in sintering of multilayers, thin films, composite materials and complex-shaped components. Sintering is then constrained. Differential shrinkage between the different materials/regions will result in the development of residual stress fields within the component.[52–55] Two types of constraint can be distinguished: (i) when an external compressive force is applied (densification is then enhanced) and (ii) when tensile stresses arise during sintering (densification is then retarded). The first case corresponds to the measurement of the sintering parameters and will be discussed in § 2.3.2. In the second case, the densification can be inhibited by sintering a film on/between non-shrinking substrate(s), sintering a heterogeneous compact (containing for example agglomerates or having a density gradient) and sintering composites (§ 2.3.5 and § 2.3.6).

In order to predict the sintering behavior of sintering bodies, a continuum mechanical framework will be used. The mechanical response of a material to a stress can be elastic, viscoelastic or viscous (figure 2.10). By considering the relaxation time τ, for a Maxwell element:

$$\tau = \frac{E^p}{E} \tag{2.8}$$

where E^p is the uniaxial viscosity and E is the Young's modulus, a body is considered to be elastic when the relaxation time is long (» 1 s); whereas, it is considered to be viscous when the relaxation time is short (« 1 s).[56]

A sintering body subjected to an applied load was assumed to show an instantaneous elastic strain and a continuous deformation controlled by viscous flow or creep.[57] However, it was shown that the elastic response has only a negligible effect on the calculated stresses and strains and therefore, sintering bodies are considered as purely viscous (relaxation time is short).[58] This theory was originally developed for materials that sinter by viscous flow, but has also been applied to materials that densify by solid state diffusion.[53] The continuum mechanical framework is based on the constitutive equations for an isotropic linear elastic solid which have the form:[45]

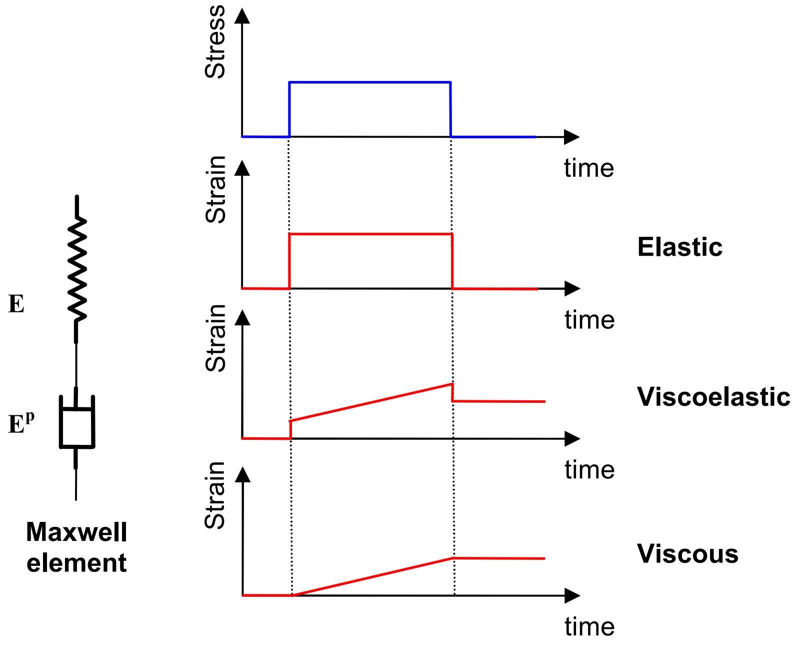

Figure 2.10: Schematic showing elastic, viscoelastic and viscous responses to an applied stress of a Maxwell element.

$$\varepsilon_i = \left(\frac{1}{E}\right)[\sigma_i - \nu(\sigma_j + \sigma_k)] \tag{2.9}$$

with i $= 1, 2, 3$ and i $\neq$ j $\neq$ k. 1, 2 and 3 are the principal axes, ν is the Poisson's ratio, σ the stress and ε the strain.

Using the viscous analogy,[53;59;60] the strains ε_i are replaced by strain rates $\dot{\varepsilon}_i$; Poisson's ratio ν is replaced by the viscous Poisson's ratio, ν^p and the Young's modulus E is replaced by the uniaxial viscosity E^p. The constitutive equations which describe the response to external constraints during sintering of a porous body thus become:

$$\dot{\varepsilon}_i^{constr.} = \dot{\varepsilon}^{free} + \left(\frac{1}{E^p}\right)[\sigma_i - \nu^p(\sigma_j + \sigma_k)] \tag{2.10}$$

$\dot{\varepsilon}^{free}$ is the free strain rate during sintering of a porous body without external constraints. Note that in the elastic case, ε^{free} is usually equal to 0 since most elastic bodies do not expand nor shrink if no load is applied.

By describing the sintering behavior by eq. 2.10, two hypotheses are assumed: the material is isotropic - the shrinkage for free sintering is the same in all directions - and linear - the response of the shrinkage rate is linear to the applied load. The parameters, $\dot{\varepsilon}^{free}$, E^p and ν^p, are specific and characteristic of the porous ceramic body. Note that there is no identification of the 3 different stages of sintering as the equations remain the same for the entire process.

Bulk and shear viscosities, respectively K^p and G^p, can be deduced from uniaxial viscosity and viscous Poisson's ratio:

$$K^p = \frac{E^p}{3(1-2\nu^p)} \tag{2.11}$$

$$G^p = \frac{E^p}{2(1+2\nu^p)} \tag{2.12}$$

Bulk viscosity is a measure of the viscous resistance to densification under hydrostatic pressure. A material with a lower bulk viscosity would sinter faster. For an incompressible and isotropic viscous liquid the Poisson's ratio has a value of 0.5, so ν^p should approach this value as the porosity goes to zero.[53] Indeed, if the viscous Poisson's ratio is higher than 0.5, it would mean that the densification rate, when an external compressive load is applied, is lower than for free sintering. The following limits can be deduced: $G^p \to G^{p\infty}$, $E^p \to 3G^{p\infty}$, $K^p \to \infty$, where $G^{p\infty}$ is the shear viscosity of the fully dense body.

With the sintering parameters defined above, the sintering stress also called sintering driving force or sintering potential can be deduced. The uniaxial sintering stress, σ_s, is expressed as a function of uniaxial viscosity and free strain rate by setting $\sigma_i = \sigma_s$, $\sigma_j = \sigma_k = 0$ and $\dot{\varepsilon}_i^{constr.} = 0$ in eq. 2.10:

$$\sigma_s = -E^p \cdot \dot{\varepsilon}^{free} \tag{2.13}$$

To compute the hydrostatic sintering stress, the viscous Poisson's ratio has to be taken into account ($\sigma_i = \sigma_j = \sigma_k = \Sigma$ and $\dot{\varepsilon}_i^{constr.} = 0$):

$$\Sigma = -\frac{\dot{\varepsilon}^{free} E^p}{1-2\nu^p} = -3K^p \cdot \dot{\varepsilon}^{free} \tag{2.14}$$

For a polycrystalline material, $\dot{\varepsilon}^{free}$ may be related to the volume diffusion coefficient and K^p may depend on grain boundary sliding[58]. From a micromechanical point of view, the hydrostatic sintering stress can be also theoretically expressed in terms of curvature and interfacial energy, as shown in the most basic form in eq. 2.15.[61;62]

$$\Sigma = \frac{2\gamma_s}{r} + \frac{2\gamma_b}{G} \tag{2.15}$$

where γ_s and γ_b are surface energy and grain boundary energy, respectively, and G and r are grain size and radius of curvature of the pore, respectively. This equation is the sum of the capillary pressure of the pores and the capillary pressure of the grains. It is obtained by calculating the derivative of total interfacial energy with total volume of the compact.

In some cases, the isotropic model is not sufficient to fully describe the behavior of a sintering body.[63] An anisotropic model should be used:[64]

$$\begin{pmatrix} \dot{\varepsilon}_1 \\ \dot{\varepsilon}_2 \\ \dot{\varepsilon}_3 \end{pmatrix} = \begin{pmatrix} \dot{\varepsilon}_1^{free} \\ \dot{\varepsilon}_2^{free} \\ \dot{\varepsilon}_3^{free} \end{pmatrix} + \begin{pmatrix} \frac{1}{E_1^p} & \frac{-\nu_{21}^p}{E_2^p} & \frac{-\nu_{31}^p}{E_3^p} \\ \frac{-\nu_{12}^p}{E_1^p} & \frac{1}{E_2^p} & \frac{-\nu_{32}^p}{E_3^p} \\ \frac{-\nu_{13}^p}{E_1^p} & \frac{-\nu_{23}^p}{E_2^p} & \frac{1}{E_3^p} \end{pmatrix} \begin{pmatrix} \sigma_1 \\ \sigma_2 \\ \sigma_3 \end{pmatrix} \tag{2.16}$$

with

$$\nu_{ij}^p = \frac{\dot{\varepsilon}_j^{free} - \dot{\varepsilon}_j}{\dot{\varepsilon}_i - \dot{\varepsilon}_i^{free}} \tag{2.17}$$

and

$$E_i^p = \frac{\sigma_i}{\dot{\varepsilon}_i - \dot{\varepsilon}_i^{free}} \tag{2.18}$$

In the particular transversely isotropic case (a special class of the orthotropic case where the properties are the same in one plane - e.g. the 1-2 plane - and different in the direction normal to this plane - e.g. the 3-axis), the following simplifications can be made:

$$\nu_{12}^p = \nu_{21}^p \quad ; \quad \nu_{31}^p = \nu_{32}^p \quad ; \quad \nu_{23}^p = \nu_{13}^p \quad and \quad \dot{\varepsilon}_1^{free} = \dot{\varepsilon}_2^{free} \tag{2.19}$$

Thus, for the case of a transversely isotropic porous body, not only three sintering parameters ($\dot{\varepsilon}_z^{free}$, E^p, ν^p) are needed to fully describe the sintering behavior of the material, but seven ($\dot{\varepsilon}_1^{free}$, $\dot{\varepsilon}_3^{free}$, E_1^p, E_3^p, ν_{12}^p, ν_{31}^p, ν_{23}^p).

2.3.2 Experimental determination of the sintering parameters

The free sintering rate can be easily measured in a dilatometer. To measure both other sintering parameters (E^p and ν^p), the sintering body is placed under stresses and the response to the mechanical loading is macroscopically monitored. Various techniques such as sinter-forging, cyclic loading dilatometry and bending creep test are used. Up to now, only the isotropic formulation has been widely used since the experimental measurement of anisotropic parameters is very challenging.[65]

2.3.2.1 Bending creep test

The bending creep test can be used to measure the uniaxial viscosity of porous materials during sintering.[66;67] Yttria stabilized zirconia beam shape samples were supported on both ends point and loaded in the center.[66] By measuring the deflection rate in the center of the specimen, the uniaxial viscosity is deduced from the viscous analogue of deflection beam theory. The drawback of this method is that the density of the specimen is not available at any time, as it has to be previously measured in a dilatometer.

2.3.2.2 Cyclic loading dilatometry

Cyclic loading dilatometry is an alternative technique to measure the uniaxial viscosity.[56;67] A constant uniaxial load is applied intermittently (for a small range of density) on a cylindrical sample. Strains in the axial direction are recorded as a function of time and allow computing the uniaxial viscosity. It is thought that the load-free periods are effective in removing the stress-induced microstructural alteration due to the loading periods (§ 2.4). The advantage of this technique is that only a single run is needed to compute the uniaxial viscosity over the whole density range.

2.3.2.3 Sinter-forging

Sinter-forging is a similar technique to cyclic loading dilatometry. A constant uniaxial load is applied on a cylindrical sample. Both axial and radial strains are recorded as a function of time and density. Both uniaxial viscosity and viscous Poisson's ratio can then be computed. This technique was successfully applied for experimental investigations on different materials such as glass,[68–70] alumina,[71–75] and other materials.[76;77] This method has been used in this work and is explained in § 3.3 in further detail.

2.3.3 Models

Sintering parameters depend on several variables. It is widely accepted that the uniaxial viscosity can be written as follows:[78]

$$E^p = E^{p0} \cdot E^{p1}(\rho) \cdot E^{p2}(G) \cdot E^{p3}(T) \tag{2.20}$$

where E^{p0} is a scaling factor, $E^{p1}(\rho)$ the uniaxial viscosity dependence on the relative density ρ, $E^{p2}(G)$ the uniaxial viscosity dependence on grain size, G and $E^{p3}(T)$ the uniaxial viscosity dependence on temperature T. The uniaxial viscosity is thermally activated and the temperature dependence follows an Arrhenius law. Uniaxial viscosity of materials which sinter by solid-state sintering is affected by grain growth: $E^{p2}(G)$ is proportional to the cube of the grain size. The density dependence is more prone to discussion and will be considered below in the presentation of the different models.

Models describing the sintering behavior of materials under constraints can be classified into micromechanical[55;79–84] and phenomenological models.[73;85;86] Here, few models are described as well as the hypothesis on which they are based.

Micromechanical models

Micromechanical models are based on geometrical assumptions of the powder compact. As mentioned earlier, an elementary cell can be composed of two spheres[28] (or more),[87] cylindrical particles[31] or an isolated pore in a matrix.[32] In order to compute the sintering stress, three methods can be applied:[81]

- the energy difference method - the sintering stress is associated with the change of total energy by a virtual change of pore volume in equilibrium
- the curvature method - the sintering stress consists of two terms; the first term is proportional to pore curvature, and the second term is also associated with the change of total energy by a virtual change of pore volume in equilibrium
- the force balance method - for an equilibrium state, the sintering stress just balances the internal surface tension forces so that the porous material does not shrink

As we have seen before, Frenkel[28], Scherer[31] and MacKenzie and Shuttleworth[32] proposed their own model based on the force balance method. Wakai *et al.*[81] used these three methods and showed that the sintering stress was identical for these three methods for idealized porous materials in equilibrium, in which the pore surface had a constant curvature at any point. Results lead to an increase of the sintering stress with density. Riedel and co-workers[79;80] used the curvature method. They computed equilibrium surfaces of open porosity like it was suggested by Beere[61] for the intermediate and late stage of sintering. Grain boundary diffusion was the dominant mass transport mechanism. Sintering stress was obtained as function of the dihedral angle and the relative density.[80] Du and Cocks[55] modeled stress fields due to heterogeneities with the help of the finite element analysis. They separated evolution laws for densification and grain growth. MacMeeking and Kuhn[88] proposed a constitutive law taking into account the distortion of the particles, the boundary diffusion and sliding. Hsueh's model[89] is essentially a linear-viscoelastic description of the process. However, micromechanical creep models of porous materials and grain growth were employed in the development of the final constitutive relationships. Using the force balance method, the micromechanical modeling can also be based on a discrete element method (DEM), which accounts for the granular nature of the material by treating every grain as a distinct element (particle).[65;82;90;91] The movement of each particle is calculated through the mechanical force equilibrium of Newton's equation of motion with other particles in contact. Parhami *et al.*[82] simulated the early stage of sintering. Investigation by Martin *et al.*[90] enables new contacts to be detected and particle coarsening was introduced. By using DEM, anisotropic sintering parameters can be also predicted.[65]

Phenomenological models

The first phenomenological models used a viscoelastic analysis.[57] Maxwell and Voigt elements (spring and dashpot models) described the response of a sintered body to mechanical applied stresses. The Laplace transformation was performed on the relevant stress equations and the time-dependent stresses and strain rates were calculated from the elastic solution. Bordia and Scherer[58;92;93] pointed out some problems since the viscoelastic analogy could not be applied. As the elastic modulus is a function of time, no simple Laplace transformation can be done. However, it was noticed that the strains during densification are enormous compared to the elastic strains and only a viscous analogy is necessary. Later work of Cai *et al.*[56] on alumina at high temperature observed the transitions between elastic, viscoelastic and viscous stage. Alumina was sintered in the viscous temperature range and thus it is consistent with Bordia and Scherer arguments.[58;92]

Raj and Bordia[57] studied the case of the sintering behavior of a bi-modal powder compact. The constitutive properties of a porous material are represented by spring-dashpot elements. The analysis combines densification with deviatoric creep, as the shear response is modeled by a Maxwell element and the densification response by a Kelvin-Voigt element. Moreover, they assumed a constant shear modulus. The model describes a glass matrix constrained by rigid inclusions well. Based upon the stochastic approach, Skorokhod[94] suggested expressions for effective shear and bulk viscosities for porous material in terms of the viscosity of the solid phase and porosity. The model by Venkatachari and Raj[73] is based on sinter-forging measurements on alumina. The applied stress was larger than the sintering stress and had a strong influence on densification. The load bearing fraction, ϕ, which is an indicator of the contact between particles, is supposed to be proportional to the relative density. Rahaman's model[85] is based on experimental results on CdO. The applied stress was much lower than the sintering stress. The model was derived by using Coble's creep mechanism for densification[95] and relies on Beere's geometrical relationship for a definite grain/pore configuration.[96] Creep rate and densification were treated as independent processes and the different parameters were then deduced from the creep equation. The load bearing area was found to depend exponentially on porosity. The fitting parameter of the empirical function describes the pore shape and low values indicate a high load bearing area. Based on sinter-forging experiments on glass, Ducamp and Raj[68] proposed a similar expression of the load bearing area.

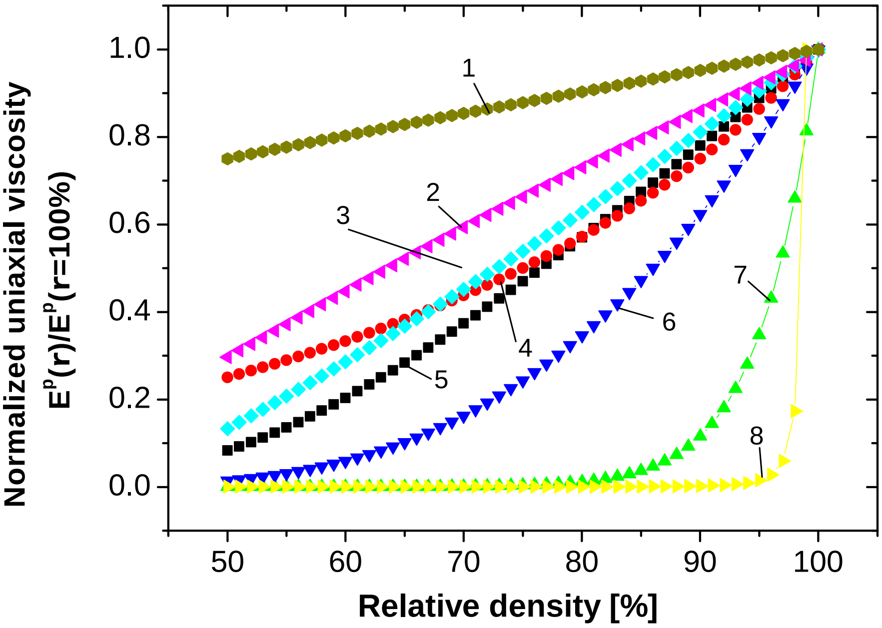

Figure 2.11: Density dependence of the normalized uniaxial viscosity by the value obtained at full density. Curve labels: 1=Raj and Bordia[57], 2=Venkatachari[73], 3=MacKenzie and Shuttleworth[32], 4=Scherer[31], 5=Skorokhod[94], 6=Ducamp[68], 7=Rahaman[85], 8=Hsueh.[89]

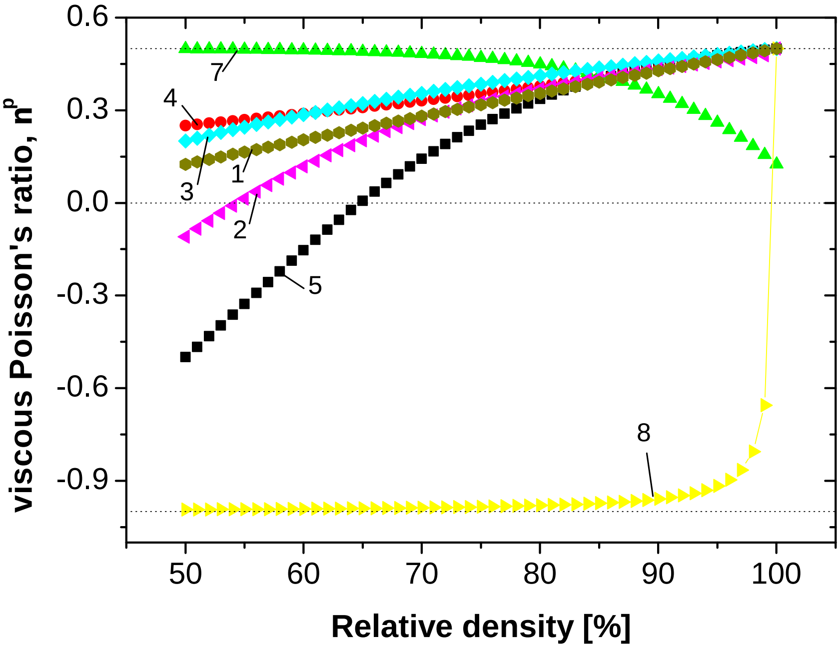

Figure 2.12: Density dependence of the viscous Poisson's ratio. Curve labels are the same as for figure 2.11.

Equations for the normalized uniaxial viscosity (figure 2.11) and the viscous Poisson's ratio (figure 2.12) can be found in appendix A. In figure 2.11, the uniaxial viscosity is plotted for some micromechanical and phenomenological models. For sake of comparison, the uniaxial viscosity is normalized by the value obtained at full density. Each model predicts an increase of the uniaxial viscosity with density. For Hsueh's model,[89] where the grain size is implicitly taken into account, the uniaxial viscosity increases drastically at relative densities higher than 95%. Raj and Bordia's model[57] predicts a value of uniaxial viscosity of a dense sample 1.1 times larger than the uniaxial viscosity of a sample with a relative density of 75% ; whereas, Ducamp's model[68] predicts an increase by a factor of 4.1.

Viscous Poisson's ratio is plotted in figure 2.12. Each model, unless Rahaman's model,[85] predict an increase of the viscous Poisson's ratio with density and reach 0.5 at full density. Venkatachari's[73], Skorokhod's[94] and Hsueh's[89] models predict negative values at low densities. As the models by Skorokhod[94] and Scherer[31] fit quite well in the range of interest of densities, the isotropic viscous Poisson's ratio is believed to be not sensitive to pore morphology.

Several points of criticism can be raised against the different models. For the phenomenological models, sinter-forging experiments were performed under a constant load during the whole densification period. As we will see later, the sintering parameters can be strongly affected if anisotropy is induced. Grain growth was found to be reduced by continuous sinter-forging:[72] the grain sizes of freely sintered samples are larger than those of sinter-forged samples at the same density and the difference tends to increase with time. Moreover, density alone as used in several previous models is not precise enough to give a good approximation of the load-bearing area.[83] The way to process the bulk samples should be taken into account.[78] Sura and Panda[97] also noticed that pore shape evolves strongly with densification and thus corrected uniaxial viscosity with a pore shape factor (derived from the elastic model from Nielsen[98]) varying with density.

2.3.4 Creep

Creep defines the time-dependent irreversible deformation under the influence of stresses leading to a change of shape of the specimen. During constraint creep and densification occur simultaneously. The creep strain, ε_c is:[99]

$$\varepsilon_c = \frac{2}{3}\sqrt{\frac{1}{2}[(\varepsilon_1 - \varepsilon_2)^2 + (\varepsilon_2 - \varepsilon_3)^2 + (\varepsilon_1 - \varepsilon_2)^2]} \tag{2.21}$$

In the case of uniaxial sinter forging $\varepsilon_1 = \varepsilon_z$ and $\varepsilon_2 = \varepsilon_3 = \varepsilon_r$, eq. 2.21 becomes:

$$\varepsilon_c = \frac{2}{3}|\varepsilon_z - \varepsilon_r| \tag{2.22}$$

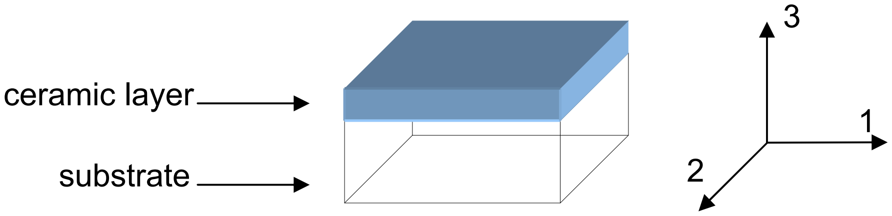

Figure 2.13: Schematic showing a film on a substrate.

This corresponds to the deviatoric strain of the strain tensor.[73] In pure densification (where the axial strain is equal to the radial strain), the deviatoric strain is equal to 0. For a constant applied stress, the ratio of the creep rate to the densification rate of a glass is almost independent of both temperature and density.[70] Chu and De Jonghe[100] studied the effect of temperature on both densification and creep by separating creep strain from total densification strain during sinter-forging, concluding that the ratio of creep rate to densification was independent of temperature and density. The creep rate was found to be linearly dependent on the uniaxial applied stress, while the densification rate depends on the mean hydrostatic stress.[70] Note that creep and densification can be treated as independent processes even if the load applied is greater than the sintering stress.[73] Creep is an important phenomenon as it relaxes the constraints. The following parameter can be defined:[101]

$$\beta = \frac{K^P}{G^P} \tag{2.23}$$

β represents the ability to relax the shear stress during sintering. A high value of β is desirable so that shear relaxation occurs faster than densification rate. For glass, it was shown by Ducamp and Raj[68] that β is always higher than 1 and increases with density.

2.3.5 Constrained sintering of laminates

Sintering of constrained films (figure 2.13) has been the subject of several investigations.[52;53;56;102–114] In this section, we consider (i) the sintering of a symmetric laminate and (ii) the sintering of an asymmetric laminate. In the first case, the camber is prohibited as the structure is symmetrical. In the second case, the laminate will camber. The camber can also be largely reduced if the substrate is rigid enough compared to the shrinking layer at a given sintering temperature.[115] In this particular case, the stress state in the shrinking layer is assumed to be similar to the one in the shrinking layer between constraining

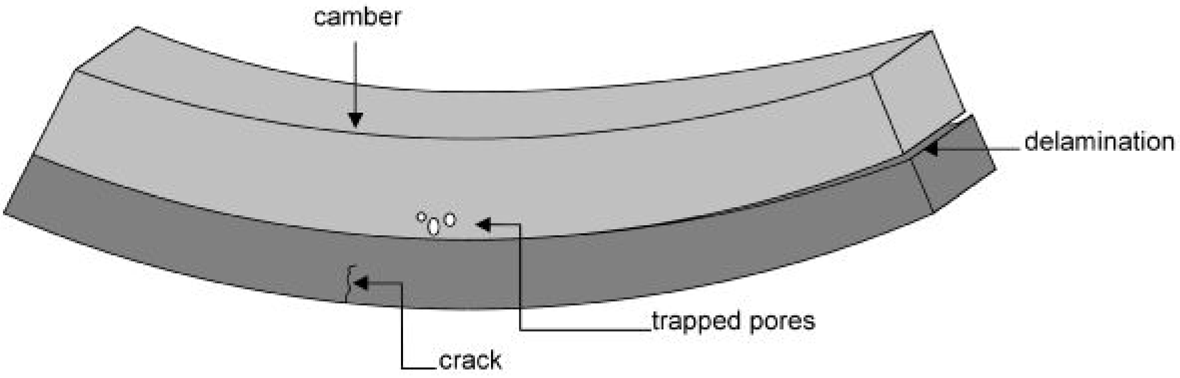

Figure 2.14: Schematic of the possible defects during constrained sintering of a bi-layer.

substrates. In any case, two materials sinter at different rates. Shear stresses are thus generated and act as internal stresses. These stresses lead to creep and are opposed to the sintering stress. Sintering will thus be inhibited.[73]

Damage

Tensile stress will lead to some defects such as cracks, delamination, camber...[56;106–108] (figure 2.14 and figure 2.15). Note that defects can be generated in films during the drying process (before sintering) and also during cooling down from the sintering temperature to room temperature. Residual stresses are formed due to the different thermal expansion between the two materials. Incompatibility stresses during sintering can be relaxed by creep. If the rate of relaxation is faster than the rate of sintering, the magnitude of the incompatibility stresses are kept to a minimum. Bordia and Raj[52] showed that the stress relaxation is governed by the shear response of the material. They showed also that the highest incompatibility stresses are reached during the initial stages of sintering. This was experimentally observed by Cai *et al.*[56;107] Cracks either opened during sintering or acted as pre-existing flaws for thermal expansion mismatch cracks. In order to avoid cracks, reduction of the heating and/or cooling rate was suggested. This enhances the reduction of mismatch stresses present during constrained sintering.

Bordia and Jagota[113] investigated crack growth for polycrystalline and glass materials. They determined the conditions for crack growth of pre-existing cracks. Proposed by Jagota *et al.*,[103] a friction parameter between the substrate and the film was defined. A critical value was found for crack growth in glass films but not for alumina films. Moreover, a damage zone was present in alumina films but not in glass films. It has also been shown that polycrystalline films in multilayered structures are observed to be more prone to the development of microstructural flaws than glass films during co-sintering.[106] The incorporation of a glassy phase could be a solution in order to improve the stress relaxation in polycrystalline films.

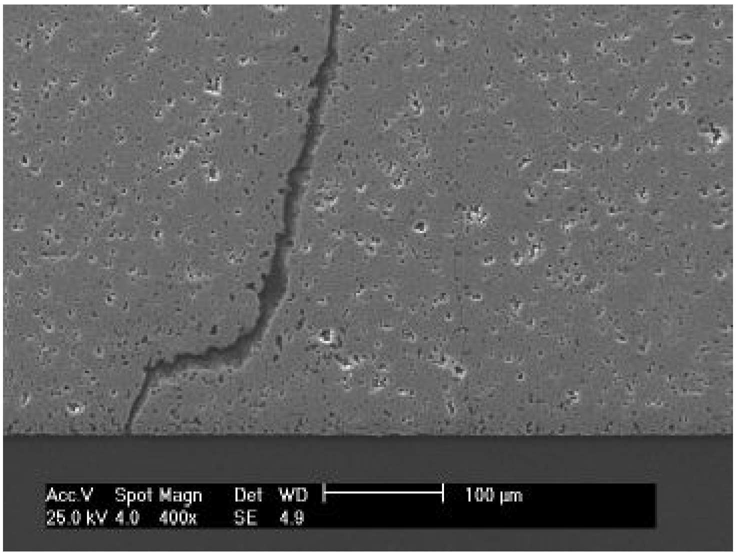

Figure 2.15: Crack in a LTCC film. The constraining substrate, at the bottom, has been removed.

2.3.5.1 Constrained sintering of a symmetric laminate

The lateral constraint imposed by a rigid substrate allows shrinkage only in the direction perpendicular to the film, $\dot{\varepsilon}_1 = \dot{\varepsilon}_2 = 0$. The film is then under a state of biaxial tensile stress. This tensile stress is equal in the plane 1-2, $\sigma_1 = \sigma_2 = \sigma^{\infty}$:[116]

$$\sigma^{\infty} = -\frac{\dot{\varepsilon}^{free} E_p}{1-\nu_p} \tag{2.24}$$

Retardation in densification

The densification rate of a constrained film, $\left(\frac{\dot{\rho}^{cons}}{\rho}\right)$ can be correlated with the densification rate of a freely sintered body, $\left(\frac{\dot{\rho}^{free}}{\rho}\right)$, via the viscous Poisson's ratio, ν^p:[58]

$$\left(\frac{\dot{\rho}^{cons}}{\rho}\right) = \frac{1}{3}\left(\frac{1+\nu^p}{1-\nu^p}\right)\left(\frac{\dot{\rho}^{free}}{\rho}\right) \tag{2.25}$$

Retardation in densification was first thought to be due to the incompatibility stresses which developed in the film.[109] However, as the hydrostatic stresses calculated by Scherer[54] are between 2 and 22% of the sintering pressure, the stresses were too low to account for the retarded densification kinetics. This was experimentally observed by Choe *et al.*[110] Another solution was proposed by Scherer: the interaction between densification and grain growth in an inhomogeneous powder compact could be the cause for the retarded densification kinetics. Garino *et al.*[105] observed that the reduction in densification rate is more pronounced for polycrystalline films than for glass films.

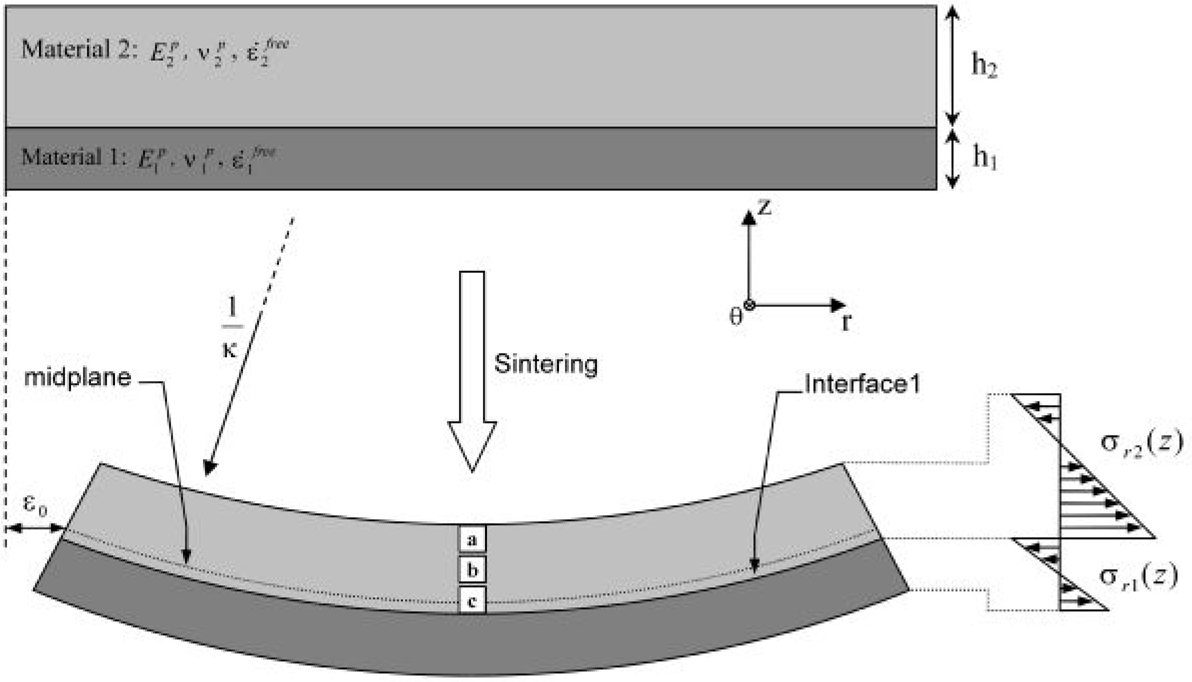

Figure 2.16: Schematic of the sintering of an asymmetric laminate.

2.3.5.2 Constrained sintering of an asymmetric laminate

During constrained sintering of an asymmetric laminate, an asymmetric stress state will arise due to the differential shrinkage and lead to the camber of the sample. Three different models can be used to predict the camber: (i) Kanters' model[102] which is believed to be the most accurate; (ii) Cai's model[107;117] which does not take into account the stress built-in due to constraining, and (iii) the Stoney equation,[115;118–120] which is a simplification of Cai and Green's model and is suitable when one layer thickness is negligible compared to the other.

Kanters' model

Let's consider the asymmetric laminate (figure 2.16). Both shrinking material and substrate are viscous with a uniaxial viscosity E_i^p, a viscous Poisson's ratio ν_i^p and a free sintering rate $\dot{\varepsilon}_i^{free}$ (i= $1, 2$ referring to the corresponding material). h_1 and h_2 are the thicknesses of the material 1 and 2, respectively.

Considering the Kirchhoff assumptions:[121]

- the plate is initially flat,
- normals remain straight, unstretched, and normal,
- the deflection (the normal component of the displacement vector) of the midplane is small compared with the thickness of the plate,

- the stress normal to the middle plane, σ_z, is small compared with the other stress components and may be neglected in the stress-strain relations.

The radial strain of the laminate can be defined with the kinematical approach as follows:

$$\varepsilon_r(z) = \varepsilon_0 - z\kappa_k \tag{2.26}$$

where κ_k is the laminate camber (inverse of the curvature radius) and ε_0 is the radial strain for $z = 0$. By convention $z = 0$ is the laminate midplane. Derivation of eq. 2.26 with respect to time gives:

$$\dot{\varepsilon}_r(z) = \dot{\varepsilon}_0 - z\dot{\kappa}_k - \dot{z}\kappa_k \tag{2.27}$$

The viscous equation in the $r - \theta$ plane is derived from eq. 2.10 with $\sigma_r = \sigma_1 = \sigma_2$ and $\sigma_3 = 0$:

$$\dot{\varepsilon}_r = \dot{\varepsilon}^{free} + \frac{1 - \nu^p}{E^p}\sigma_r \tag{2.28}$$

Combining eq. 2.27 and eq. 2.28, the stress along the laminate thickness is expressed by:

$$\sigma_r(z) = \frac{E^p(z)}{1 - \nu^p(z)}(\dot{\varepsilon}_0 - z\dot{\kappa}_k - \dot{z}\kappa_k - \dot{\varepsilon}^{free}(z)) \tag{2.29}$$

By applying the force and torque equilibrium over the thickness on the whole compound, one obtains two equations:

Force equilibrium:

$$\int \sigma_r dz = 0 \tag{2.30}$$

Torque equilibrium:

$$\int \sigma_r z dz = 0 \tag{2.31}$$

The two unknowns, κ_k and ε_0, are deduced from eq. 2.30 and eq. 2.31.

The stress induced in the laminate, $\sigma_r(z)$ is calculated from eq. 2.29. Radial and axial strain rates are deduced from eq. 2.28 and the viscous equation in the z direction:

$$\dot{\varepsilon}_z = \dot{\varepsilon}^{free} - \frac{2\nu^p}{E^p}\sigma_r \tag{2.32}$$

Sintering parameters (E^p, ν^p and $\dot{\varepsilon}^{free}$) are then corrected with the new calculated density for the next calculation step (see Appendix B).

Cai's model

Cai's model[107;117] is directly derived from the elastic solution of the bending of an asymmetric laminate where a mismatch strain exists between the two layers.[122;123] Cai *et al.*[107;117] applied the viscous analogy and obtained the following solution for the camber rate:

$$\dot{\kappa}_G = \left(\frac{-6(m+1)^2 mn}{m^4n^2 + 2mn(2m^2+3m+2)+1}\right)(h_1+h_2)\Delta\dot{\varepsilon} \tag{2.33}$$

where $\dot{\kappa}_G$ is the camber rate defined by Cai *et al.*[107;117], $n = \left(\frac{E_1^p}{1-\nu_1^p}\right)\left(\frac{1-\nu_2^p}{E_2^p}\right)$, $m = \frac{h_1}{h_2}$ and $\Delta\dot{\varepsilon} = \dot{\varepsilon}_2^{free} - \dot{\varepsilon}_1^{free}$

The **Stoney formula** is based on old paper.[124] Lu *et al.*[118] applied the viscous analogy and the obtained formula can be seen as simplification of Cai's model (eq. 2.33) with $m << 1$:

$$\dot{\kappa}_S = \frac{-6m^2 n\Delta\dot{\varepsilon}}{h_1} \tag{2.34}$$

where $\dot{\kappa}_S$ is the camber rate defined by Stoney.

In-plane stresses can be deduced from these three different models.

2.3.6 Sintering with rigid inclusions

Sintering with rigid inclusions has been the interest of a lot of studies.[54;57;76;89;93;125–127] In the general case, the inclusions reduce the densification rate (and sometimes the final density) and crack-like defects are induced. Two cases can be envisaged: (i) the inclusions sinter faster than the matrix or (ii) the matrix sinters faster than the inclusions. In the second case, which has been extensively studied, the retardation of densification is observable at all volume fractions of inclusions and the retardation is more severe as the volume fraction of inclusions increases. The stresses have their maximum values at the matrix-inclusion interface and decrease as 1/r^3 in the matrix. Scherer developed the composite sphere model[54] which is analogous to the problem of thermal expansion mismatch. The stress in the inclusion is compressive and in the matrix is tensile so it opposes to the compressive sintering stress. The tensile stress is often called a backstress.

Raj viscoelastic model[57] predicted large tensile stresses as high as hundred times the hydrostatic sintering stress, whereas Scherer[54] predicted small backstresses:

$$\frac{\sigma_m}{\Sigma} = \frac{-v_i}{v_i + 3K_m^p/4G_m^p} \tag{2.35}$$

where σ_m is the transient stress in the matrix, v_i is the volume fraction of the inclusions and the subscript m refers to the matrix. The backstress can be up to 2 times higher than the hydrostatic sintering stress if the viscous Poisson's limits are between 0 and 0.5. Linear densification rate, $\dot{\varepsilon}_c$, of the composite is predicted to be:

$$\dot{\varepsilon}_c = \frac{(1 - v_i)\dot{\varepsilon}_m^{free}}{1 + \frac{4}{3}\frac{G_m^p}{K_m^p} v_i} \tag{2.36}$$

Scherer[54] proposed a second model, the self-consistent model. The shear viscosity of the matrix is replaced by the shear viscosity of the composite, G_c^p. An approximation to G_c^p is obtained from the Hashin-Shtrikman equation.[128] For fractions less than 20 vol% the predictions of the two models are almost identical but they deviate significantly at higher values. The self consistent model predicts higher densification delays. However, the model still underestimates the effects of inclusions. For glass-matrix composites, the effect of non-densifying inclusions on the densification rate of the glass matrix has been found to be small as long as the inclusions do not form a percolating network. For instance it was shown, for a glass matrix, that if the volume fraction of inclusions was below $\sim$ 12%,[126;129] the sintering behavior was in good agreement with Scherer's model prediction.[54] One possible reason of the discrepancies with higher inclusion content could be that the elastic analysis, on which Scherer's model is based, is valid for non-interacting stress fields and so does the viscous analysis. Indeed, a percolating network will be reached when the volume fraction of particles is 16% in three dimensions (the structure is then mechanically rigid). The percolation threshold depends on aspect ratio and orientation of the particles.[130] If the inclusions form strong bonds, the densification rate will be reduced significantly and the viscosity increased; whereas, if there is a phase between the inclusions, higher inclusions content can be accommodated without a drastic reduction in the densification rate.

The retardation can be also attributed to the existence of different types of porosity.[33] Pores may be embedded in matrix material only, and pores are also possible in interstices between matrix powder particles and inclusions. The different pore types will have different surface energies, and thus, they will lead to an overall different driving force for sintering in the composite powder compact in comparison with the inclusion-free compact. It could lead to density saturation.[34] Density saturation could also be attributed to insoluble gases entrapped in the initial pores, and bubbles formed by the release of dissolved gas (which can be catalyzed by crystallization).[27] He and Zhao[131] studied the influence of inclusion shape on viscous sintering. If the aspect ratio of the particles was different than one, the overall shrinkage was lower than for spherical particles, whereas the average stress in the matrix was higher.

Inclusions also affect the uniaxial viscosity. Salamone *et al.*[76] studied by sinter-forging the effect of rigid inclusions on the densification and constitutive parameters of liquid-phase-sintered $YBa_2Cu_3O_{6+x}$ powder compacts. It was reported that the inclusions reduce the densification rate and increase its viscosity compared to glass. The viscous Poisson's ratio was found to fit Scherer's model.[31]

2.4 Anisotropy

Anisotropy can be characterized at different scales. At a microscopic level, anisotropy is present in the microstructure, as pores and particles may have a preferred orientation. At a macroscopic level, anisotropy is evidenced by the difference of shrinkage and viscous properties in the different directions. Both scales are related to each other. Anisotropy can be induced into the compact body from different ways: green bodies can already be anisotropic from processing, porous bodies can become anisotropic during sintering when stresses are either applied or induced by constraining conditions.

2.4.1 Anisotropy in the green body

2.4.1.1 Die pressing

Giess[132] observed different shrinkage in the axial and radial direction for glass compacts composed of non spherical crushed glass particles. Particle orientation during pressing is believed to be the source for anisotropy during sintering: flat sides of the particles tend to align horizontally.[33] Exner and Giess[133] found a correlation between the shrinkage anisotropy factor k and the degree of orientation of the pore/solid interface. k is defined as following:

$$k = \frac{\Delta L/L_0}{\Delta D/D_0} = \frac{\varepsilon_z}{\varepsilon_r} \tag{2.37}$$

Irrespective of particle size or shape, the shrinkage is always smaller in the pressing direction. Indeed, Olevsky[134] showed that the sintering stress is larger in the direction of the larger pore axes because of the smaller value of the radius of curvature in this direction.

Shrinkage anisotropy could also arise from other factors such as particle rearrangement and inhomogeneous density distribution in the green compact.

2.4.1.2 Tape casting and lamination

Anisotropy in the plane induced by tape casting was studied by Raj and Cannon[135]. Tape cast substrates exhibit large sintering shrinkage anisotropy in the plane. Shrinkage in the transverse direction is always higher than that in the casting direction. The anisotropy is higher in the initial stages of sintering and decreases as sintering progresses. High shear rates, obtained with increased casting speed and smaller doctor blade gap, resulted in increased anisotropy. Image analysis of the surface of green tapes showed significant correlation between particle orientation and shrinkage anisotropy: shrinkage was found to be higher in the transverse direction, though the particles were oriented in the casting direction. While the Laplacian pressure in the direction of larger pore axis is higher, the viscosity will be larger in the same direction, thereby reducing the overall anisotropy effect.

Lamination without a die press increases strongly the anisotropy in the plane perpendicular to the axial direction.[136] For alumina, it was found that the final in-plane shrinkage is in any case higher than the axial shrinkage.[63;136] It was related to the packing structure being denser in the axial direction[136] and pores oriented parallel to the plane.[63]

2.4.2 Anisotropy under uniaxial load during sintering

Gravity has to be taken into account and provides an external stress inducing anisotropy. Olevsky[137;138] elaborated a mathematical model showing the gravity effect. It resulted in isosceles trapezoid shaped samples. At the beginning of sintering (when density is lower than 72%) greater intensity of shrinkage anisotropy is provided by diffusional creep mechanism than by viscous flow. On the other hand, the viscous flow mechanism causes higher anisotropy at higher densities ($72\% < \rho < 100\%$).

Boccaccini and Olevsky[139] plotted qualitatively the anisotropy factor, k (eq. 2.37), for different cases of glass-powder compacts under a constant uniaxial load. They distinguished two different cases:

- The viscous deformation induced by sintering is initially higher than the viscous deformation induced by the external uniaxial stress (figure 2.17(a)).
- The viscous deformation induced by the external uniaxial stress is initially higher than the viscous deformation induced by sintering (figure 2.17(b)).

In both cases, k is dependent on time and after a certain time the anisotropy factor reaches a limit which corresponds to the inverse of the effective Poisson's ratio. In the first case, the load is smaller than the sintering stress only initially (I). The sintering stress

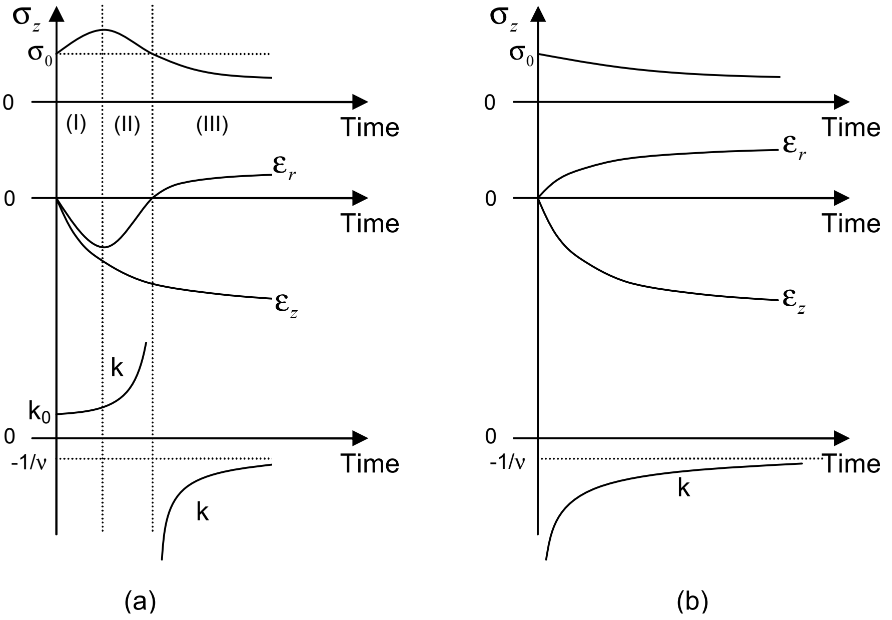

Figure 2.17: Schematic diagram showing the evolution of the relevant variables during sintering of glass-powder-compacts under a constant uniaxial load. (a) The viscous deformation induced by sintering is initially higher than the viscous deformation induced by the external uniaxial stress, (b) the viscous deformation induced by the external uniaxial stress is initially higher than the viscous deformation induced by sintering.[139]

further decreases as densification proceeds and the applied load becomes larger than the sintering stress. It is then corresponding to the first case.

To measure the sintering parameters, whatever the technique used, an external load is applied. This load will have an effect on the shrinkage anisotropy, microstructure and density. Isotropic equations used during the experiment may be not valid anymore. The goal is to get rid of these effects. One envisaged solution is to use loads smaller than the sintering stress. However, for glass based systems, even small loads can result in significant shear due to low intrinsic shear viscosity of the glass phase[139;140] (nevertheless, if the load is kept below ~ 5 kPa, the shrinkage anisotropy factor will be hardly dependent on stress). In order to avoid this problem, optical dilatometers could be used.[141] Another envisaged solution is to reduce the time when the load is applied. Bordia[58;92] and Zuo[72;74] noticed the importance of the microstructural verification such as pore size and orientation as well as grain growth. In the case of continuous sinter forging (the load is applied for a large increase of density), it was observed that pores elongate along the loading direction as the externally applied load promotes neck growth, whereas, for free sintering no preferred pore orientation was observed.[72] Both effects change the values of the uniaxial viscosity and the viscous Poisson's ratio. To avoid microstructural modifications, Zuo performed discontinuous sinter-forging.[74] Free sintering takes place up to various predefined densities and subsequent sintering at various constant uniaxial loads for a small increase of densities

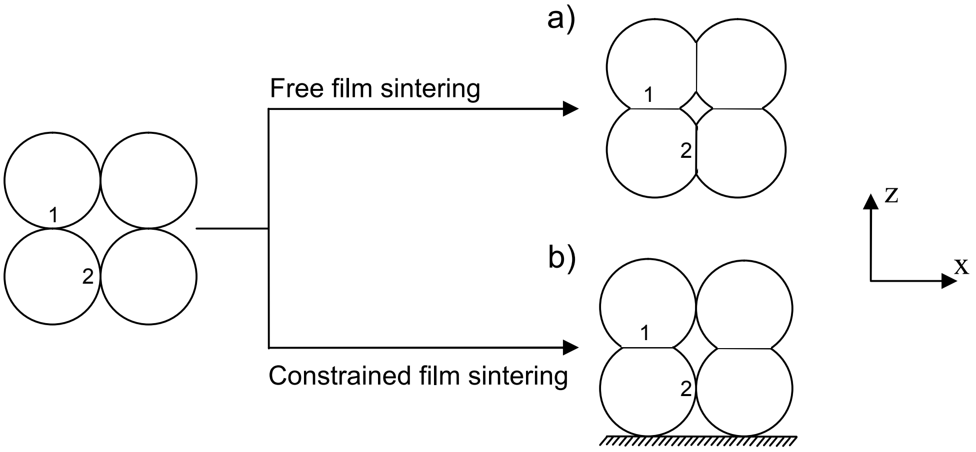

Figure 2.18: Schematic diagram of particle morphology of free (a) and constrained (b) polycrystalline films during sintering.

(= 5% in the case of alumina[74]). Cai *et al.*[56] proposed cyclic dilatometry to measure the viscosities and eliminate the stress history effects. The stress history effect (changes in shrinkage anisotropy and sample microstructure) is minimized as between the loading regimes, unloading regimes take place and allow the material to recover toward a stress-free state. It was shown that a constant load test overestimates the viscosity by an order of magnitude compared with the cyclic loading test.[142] Grain size of a loaded specimen and a freely sintered specimen were compared and did not show any variation.[56]

2.4.3 Constrained sintering of laminates

Macroscopically, this is a boundary case as the layer cannot shrink in the plane and the anisotropy factor tends to infinity. An orientation of the pores may result during sintering (figure 2.18).[63] Considering four particles, the probability of neck formation at the position 1 and 2 for a film freely sintered is the same, whereas, when the film is constrained, the neck formation in position 1 is favored to the neck formation in position 2 as the particles in the x direction cannot approach each other. As indicated in figure 2.18, pores elongate along the z direction. This was experimentally observed by Guillon *et al.*[63] Moreover, densification retardation and preferential pore orientation were found to be more important for thinner films. The authors define two levels of geometrical constraint: in the vicinity of the substrate, a lower density and finer microstructure were observed compared to the center of the layer. The presence of this interface layer is suggested to result from hindered particle rearrangement.[63]

2.4.4 Sintering with rigid inclusions

Non-sintering particles in a glass matrix influence also anisotropy. For glass-ceramics, Boccaccini and Olevsky[130] showed that sintering anisotropy decreases as content of inclusions increases compared to the sintering behavior of the glass. In any case, samples were found to shrink more in the radial than in the axial direction. However, if the inclusions are oriented, anisotropic shrinkage is intensified.[130] Shrinkage anisotropy can be also influenced by partial or total crystallization: the new crystallites are playing the same role as non-sintering particles.

2.5 Sintering of LTCC

2.5.1 Densification behavior of freely sintered laminates

Freely sintered laminates show an anisotropic shrinkage behavior in all 3 directions.[143] Anisotropy is directly linked to particle shape and size distribution and is therefore strongly affected by powder processing.[143] If the anisometry of particles can be reduced, anisotropic shrinkage is shown to be reduced.

2.5.2 Measuring sintering parameters

In order to achieve reliable predictions of shape and dimensional changes during manufacturing of LTCC packages, knowledge of the sintering parameters and their evolution during sintering is essential.[142;144–150] Many theoretical models have been proposed to describe the mechanical behavior of sintering systems. However, adequate data are needed to test these models. Recent publications reported sintering parameters experimentally measured for different LTCC materials and the results are presented below.

2.5.2.1 Uniaxial viscosity

Temperature and heating schedule have an important effect on the uniaxial viscosity: E^p can be determined at an isothermal temperature[142;146;148] or during a heating ramp.[147–149] In the first case, the uniaxial viscosity depends only on density and increases as densification proceeds. In the second case, the temperature has a great impact on the uniaxial viscosity. At the beginning of densification, E^p decreases (due to the increase of temperature) whereas it increases at higher densities (densification effect).

Xie[146] measured the uniaxial viscosity by continuous sinter-forging for three different commercial LTCC materials at a constant temperature. The viscosity varied non-linearly with relative density, starting from a very low value in the low-density region and increasing rapidly after a threshold density. His results fitted quite well with Ducamp's model[68] but conflicted with Scherer's model.[31] Discrepancies were attributed to non-circularity of the pores.

The cyclic loading dilatometry technique was used to measure the viscosity of three commercial glass based materials used in the LTCC technology.[142;145;148;149] Since the radial shrinkage is not accessible using the cyclic loading dilatometry device, Mohanram *et al.*[142;148] made the hypothesis of a constant anisotropy factor, k, defined in eq. 2.37 to calculate the density at any time. Uniaxial viscosities were ranging from 0.1 to 100 GPa.s. The authors paid attention to the microstructural changes due to the load. The presence of low density regions was more pronounced in the case of the specimen under a constant-loading than for freely sintered or cyclic loaded samples. This can be explained by the fact that an external load reduces radial shrinkage and thus more porosity is observed under the loading surface in the axial direction. Furthermore, isolated pores were present in freely sintered specimens and not in the constant loaded specimens. In comparison to a cyclic load test, a constant-load method underestimates the strain rate, because of the gradual decrease in driving force for sintering in the axial direction. This results in an overestimation of the viscosity, since the viscosity is inversely related to the strain rate (eq 2.10). The obtained uniaxial viscosity of the three commercial LTCC materials was compared with the models of Scherer[31], Rahaman[85], Ducamp[68] and MacKenzie and Shuttleworth.[32] Experimental results differed significantly from the model predictions. The uniaxial viscosity showed a stronger dependence on density. Mohanram *et al.*[142;148] attributed the large increase of the uniaxial viscosity (two orders of magnitude) to crystallization and the change of composition of the glass. LTCC containing a filler had higher uniaxial viscosities than glasses. Similar results were found for other materials.[144;145;149;150]

2.5.2.2 Viscous Poisson's ratio

Mohanram *et al.*[147] developed a novel method to calculate the viscous Poisson's ratio. By measuring the free shrinkage rate, $\dot{\varepsilon}_z^{free}$, and constrained shrinkage rate, $\dot{\varepsilon}_z^{cons.}$, of a film, viscous Poisson's ratio can be calculated as follows:

$$\nu^p = \frac{\dot{\varepsilon}_z^{cons.} - \dot{\varepsilon}_z^{free}}{\dot{\varepsilon}_z^{cons.} + \dot{\varepsilon}_z^{free}} \tag{2.38}$$

Several assumptions are made to derive the above equation: radial shrinkage of the constrained specimen is zero through the thickness, the free shrinkage rate is not influenced by the constraining stress and the constraining stresses are constant through the thickness. The viscous Poisson's ratio of a Pb-borosilicate glass system with alumina filler particles (DuPont 951GreenTape^{TM}) was found to be in good agreement with the models of Venkatachari[73] and Scherer.[31] However, a change in microstructure is expected as the film cannot densify in the plane (§ 2.4) and the measured viscous Poisson's ratio should be anisotropic. As the results are fitted by the models, the glass is believed to relax the stresses such as the transient stresses do not influence the shrinkage behavior and hence limited anisotropy is induced.

2.5.3 Camber and constrained sintering

LTCC modules are co-fired in one step. Constraints appear due to the mismatch in sintering kinetics between the different materials composing the LTCC module. Different cases can be distinguished: mismatch in sintering kinetics between (i) conductors and LTCC substrates, (ii) different LTCC materials and (iii) LTCC material and constraining substrates. To achieve better geometrical tolerances and to reduce the defects present in the final compound, different strategies are adopted.

2.5.3.1 Mismatch in sintering kinetics between conductors and LTCC substrates

Silver, which is a common conductor in the LTCC technology, densifies with boundary diffusion control whereas the LTCC substrates sinter by viscous flow. Thus, the densification temperature ranges of both materials are different. It has been observed that the silver layer stops densifying when the LTCC material begins to densify.[119;120] Hence, during sintering of a bi-layer, three steps can be distinguished: the sample cambers upward, then becomes flat and finally cambers downward (silver is printed on top of the LTCC substrate). The first step corresponds to metal densification and the last step to LTCC substrate densification.

The conductor layer is much thinner than the LTCC layer and the Stoney equation (eq. 2.34) was applied to predict the camber. The camber rate depends on three different factors: (i) geometrical factors with both thickness of the metal and ceramic layer - note that the camber rate increases with decreasing the thickness of the ceramic layer and increasing the thickness of the metal layer; (ii) viscous properties of the material such as the uniaxial viscosity and the viscous Poisson's ratio; (iii) processing parameters: by increasing the differential sintering rate between both materials, the camber rate increases. It is interesting to notice that if the difference in densification kinetics between metal and ceramics is absent, no camber should develop.

Lu *et al.*[118] found that the densification kinetics of the LTCC constrained by the rigid substrate are almost identical to the kinetics of the free material. It would mean that the viscous Poisson's ratio should be close to 0.5 (i.e. should be incompressible). Lu determined the stress developed in the LTCC layer by measuring the camber and found that values ranged from 60 kPa to 6 MPa. The maximum stress observed occurred at the faster densification rate.[151]

Note that the camber may not only be due to the different sintering kinetics of the LTCC substrate and the paste conductor as the LTCC substrate itself can undergo non-uniform dimensional behavior that leads to localized curvature[152] as inhomogeneities in density are common.[153] Because of particle sedimentation it is reasonable to imagine that the upper layer would consist of smaller particles. This upper layer will then shrink faster than the bottom layer. Curvature was also found to be different whether the layer tape-casted on the substrate is perpendicular or parallel to the casting direction: the particle alignment and segregation lead to differences in shrinkage rate.

In order to match the sintering behavior of the silver film and the LTCC material, glass powder has been added to the silver paste.[7;115] The addition of LTCC material reduces the total shrinkage but shifts the densification behavior to temperature closer than the sintering temperature of the LTCC material. It was shown that it has a great impact as the camber can be reduced by a factor 1.5 and 3 if 15 and 30 vol. % of glass content were added.[115] However the conductivity of the new silver paste is reduced, and the crystallization kinetics of the LTCC substrate can be modified. In order to reduce the shrinkage mismatch between the metal conductor and the ceramic matrix, other solutions can be envisaged : optimization of ceramic particle size, softening point, lamination parameters and firing profile.

2.5.3.2 Mismatch in sintering kinetics between LTCC materials

A new approach for the LTCC technology is to cofire two or more LTCC substrates together (*advanced LTCC*).

Chang *et al.*[145] studied the sintering behavior of a GC/GCC bi-layer. Densification range of both materials was lying in the same temperature range: the tensile stress that developed in both layers was found to be less than the sintering stress (few hundred kPa) and no defects could be observed such as de-densification, de-bonding or cracks.

2.5.3.3 Mismatch in sintering kinetics between LTCC material and constraining substrates

The constraining layer serves several functions: it provides a uniform high friction contact layer and it provides an escape pathway for the volatile components of the ceramic tape prior to sintering.[154] To design constrained sintering, several parameters have to be taken into account for the constraining layer, such as mechanical properties - it should be stiff enough to prevent buckling -, thermal properties - the layer should not shrink or expand during the sintering cycle -, it should also remain porous - the glass phase should not penetrate into the constraining layer in order to remove it more easily (the wetting angle and the viscosity of the glass phase of the LTCC material are then critical parameters).[154]

Stress development during the constrained sintering of a sandwich structure of Alumina / Glass / Alumina was studied. During sintering, glass infiltrates porous alumina during constrained sintering.[155] In order to remove easily the green tape after sintering, this phenomenon is not desired. Addition of a small amount of alumina ($\sim$ 5 wt%) into the glass material eliminates this problem. The transient tensile stress was determined using a finite element code and has been found to decrease from the interface between the substrate and the shrinking layer to the middle of the shrinking layer. Pore density increased from the free edge to the center of the sample. Density was found to be also dependent on the thickness of the glass layer. As the thickness of the shrinking material decreased, densification was hindered. However, calculation of the tensile stress with different thickness did not bring significant change. A concave morphology was observed at the free edges and was more pronounced as the glass layer was thicker.

Bang and Lu[156] studied the sintering behavior of a borosilicate glass + silica system (20 vol.%) on a rigid silicon substrate. Densification rates were reduced in the constrained film. The authors compared experimental results with the prediction of different models (Skorokhod,[94] Scherer[31] and MacKenzie and Shuttleworth[32]) for K^p and G^p. None of the models seemed to give a satisfactory fit to the measured densification profiles. It was thought that it could be due to differences in microstructure between the free and constrained films.

Zero-shrinkage technology

The zero shrinkage technology has been developed in order to achieve better dimensional control.[20;154;157;158] Tolerances in the shrinkage of LTCC modules freely sintered can reach up to ± 0.5%. Typically ± 0.2% for r and θ direction is achieved (figure 2.19). It still causes problems for device mounting: over the length of a sheet of 200×200 mm^2, this variation results in a positional uncertainty of ± 40 μm. Three solutions can be envisaged to reduce these tolerances:[158] (i) the pressureless constrained sintering (PLCS); (ii) the pressure assisted constrained sintering (PACS) and (iii) self-constraining laminates (figure 2.19).[20] For PLCS, only constraining layers prevent the in-plane shrinkage, whereas for PACS, an additional load is applied to enhance the axial shrinkage. PACS achieves better tolerances (± 0.05%) whereas in PLCS, the tolerances achieved are about ± 0.1%.[158] Moreover, PACS allows a higher number of layers to be co-sintered and suppresses the concave morphology observed at the edges if the PLCS technique is used. Self-constraining laminates arise from the combination of LTCC tapes with separate ranges of sintering temperature.[19] The inner layer, LTCC 1, densifies completely up to a temperature T_1. Subsequently, the two outer layers LTCC 2 start to densify. The advantage of this technique is that no sacrificial layers are used and thus, a post processing step is avoided compared to PLCS or PACS.

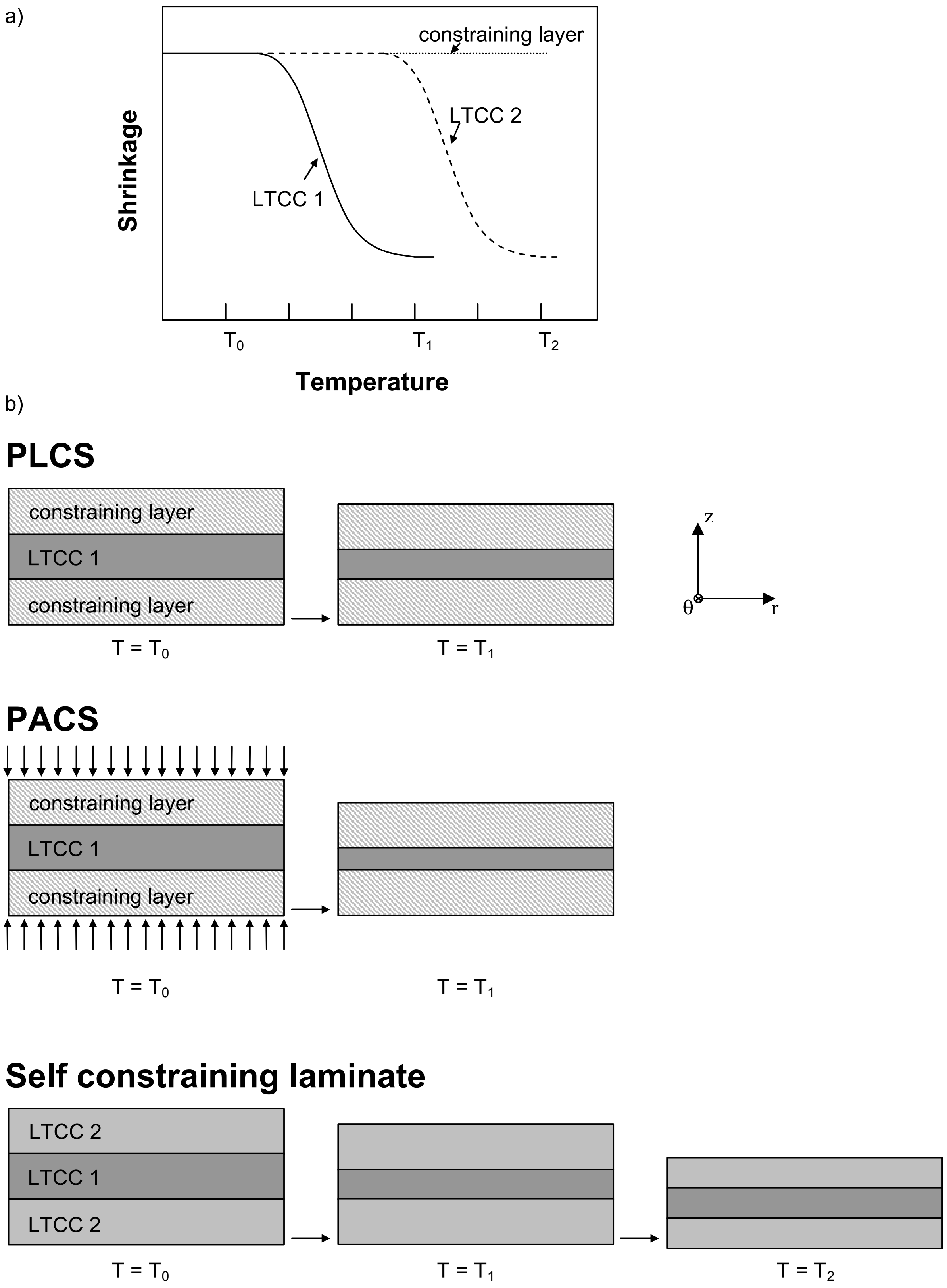

Figure 2.19: Schematic illustrations for: a) different densification range for LTCC 1, LTCC 2 and constraining layer and b) PLCS, PACS and self constraining laminate.

Chapter 3

Experimental methods

3.1 Material

The material studied is the commercial Ceramtape GC (CeramTec AG, Plochingen, Germany). It consists of a calcium aluminosilicate glass with an alumina ceramic filler. Proportion of alumina particles is 43% by weight (= 35% by volume).[143] The composition of the glass has been determined by Inductively Coupled Plasma (ICP)* and is given in table 3.1. Composition in the ternary diagram is indicated by a black point in figure 3.1. Theoretical density of 2.92 g/cm^3 is provided by the manufacturer.

Oxides	**SiO_2**	**Al_2O_3**	**CaO**	**B_2O_3**
	63.4%	9.7%	20.8%	6%

Table 3.1: Composition of the glass.

3.2 Sample preparation

Two kinds of samples are prepared: bulk samples and laminates.

3.2.1 Bulk samples

Material powder is obtained after burn-out of the commercial tapes at a temperature of 450 °C for 2 hours. Mean particle size is about 1 μm. Cylindrical specimens are uniaxially dry pressed at 150 MPa for 20 s and then cold isostatically pressed at 700 MPa for 1.5 min. Obtained samples are free of defects and did not show any delamination, end caping or ring caping. Green bodies have the following dimensions: 16.85 ± 0.05 mm in height and 11.44 ± 0.03 mm in diameter, with a relative green density of 68.0 ± 0.2%. Density of sintered samples is measured by the Archimedes method (ASTM C 20-92[159]).

---

*measured by Martin Rauscher (Friedrich-Alexander University of Erlangen-Nuremberg)

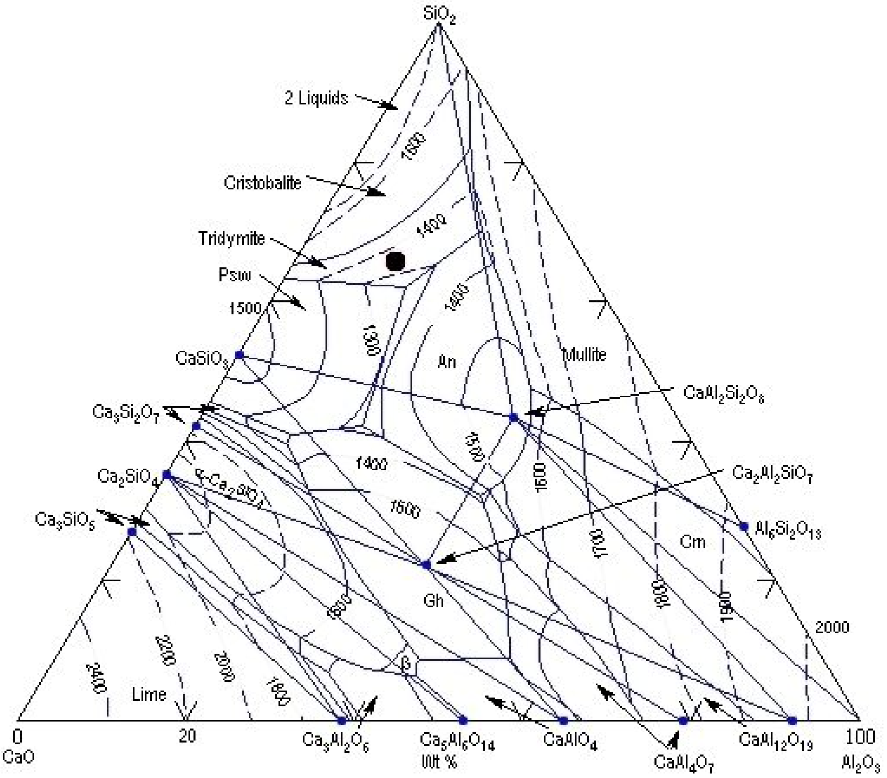

Figure 3.1: Ternary phase diagram SiO_2-Al_2O_3-CaO. The composition of glass is indicated by a black dot.

3.2.2 Laminates

Tape cast LTCC green sheets, provided by the manufacturer, are initially 284 μm thick with a relative green density of 53%. Green sheets are alternatively laminated at 10 MPa at 80 ° C for 10 min (COLLIN press, Dr. Collin GmbH, Ebersberg, Germany) in a steel die with a square section of 5×5 cm^2. Considering A as the tape cast direction and B as the perpendicular direction, laminates show the following sequence: A-B-A-B-A...B-A. Laminates are cooled down to room temperature under load. Between the laminate and the metal die, a mylar film is used to prevent sticking of the ceramics on the metal. After lamination and disregarding the binder present in the green body, the green relative density is 59% (note that this relative green density is much lower than for bulk samples).

To laminate LTCC green sheets on dense and brittle substrates, additional LTCC green sheets with a mylar film are placed between the sample and the die such as these sheets act as "cushions" and prevent cracking of the substrate. Samples are afterwards cut to desired dimensions.

Burn-out of laminates is carried out at 450 ° C for 2 hours. Burn-out of laminates laminated with a dense substrate is more crucial than for laminates without any dense substrate: the path for the binder removal is made difficult as the constraining substrate acts as physical barrier. The heating ramp is then reduced from 5 ° C/min (for free-standing laminates) to 1 ° C/min (for laminates with a dense substrate).

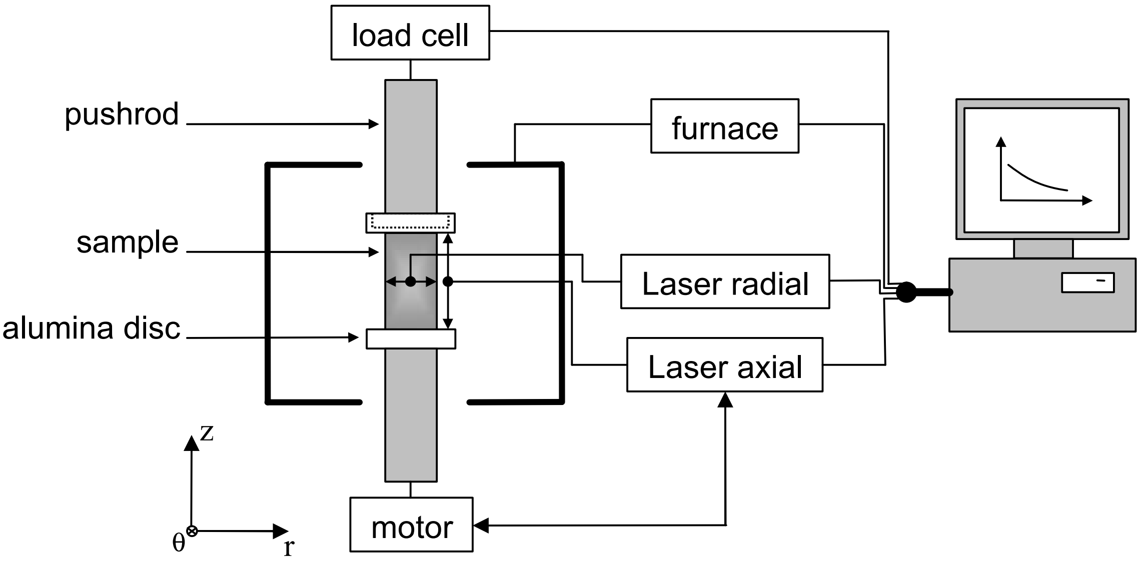

Figure 3.2: Schematic of sinter-forging.

3.3 Sinter-forging

3.3.1 Continuous and discontinuous sinter-forging

Sinter forging is one of the more precise and reliable techniques to determine the sintering parameters of bulk samples. Note that sinter-forging is not only used as a technique to measure sintering parameters but it can also be used as a pressure-assisted densification technique to improve densification.[77]

A load, F, is applied to a cylindrical dry pressed specimen (figure 3.2). Diameter and height are measured simultaneously with two high-resolution laser scanners (± 2 μm).[160] Alumina discs are placed between the pushrods and the sample to allow the height measurement. For free sintering, the force exerted by the alumina disc has been shown to have an effect on the sintering behavior. Hence, the procedure has been optimized by drilling an annular hole into the alumina disc (represented by the dash lines in figure 3.2). Radial and axial strains (ε_r and ε_z, respectively) are defined as follows:

$$\varepsilon_r = \ln \frac{D(t)}{D_0} \tag{3.1}$$

$$\varepsilon_z = \ln \frac{H(t)}{H_0} \tag{3.2}$$

where $D(t)$ and $H(t)$ are the diameter and the height of the sample as a function of time and D_0 and H_0 are the initial diameter and height, respectively. Knowing the green body density, ρ_0, the density as a function of time, $\rho(t)$, can be determined:

$$\rho(t) = \rho_0 \cdot exp\left[2 \cdot \varepsilon_r(t) + \varepsilon_z(t)\right] \tag{3.3}$$

Friction at the loaded ends of the specimen may influence the stress distribution and results in a heterogeneous stress state and barreling. A true uniaxial stress state is difficult to achieve. To avoid this problem, the ratio of height to diameter of the sample used is about 1.5 and boron nitride is used as a lubricant to reduce the friction and to prevent the bonding between the two Al_2O_3 disks and the cylindrical sample. A boron nitride thin film is coated on one side of the Al_2O_3 disks by placing a drop of a mixture of boron nitride powder and isopropanol.

The applied axial load, F, is kept constant during sintering. Since the cross-sectional area of the specimen, $A(=\pi(D/2)^2)$, changes with time, the axial stress σ_z is time-dependent:

$$\sigma_z = \frac{F}{\pi(D_0/2)^2} \cdot exp\left[-2 \cdot \dot{\varepsilon}_r(t)\right] \tag{3.4}$$

Axial and radial strain rate are calculated by taking the derivative of the axial and radial strains with respect to time. Rewriting eq. 2.10 in cylindrical coordinates for the sinter-forging case ($\sigma_r = \sigma_\theta = 0$), we obtain:

$$\dot{\varepsilon}_r = \dot{\varepsilon}^{free} - \frac{\nu^p \sigma_z}{E^p} \tag{3.5}$$

$$\dot{\varepsilon}_z = \dot{\varepsilon}^{free} + \frac{\sigma_z}{E^p} \tag{3.6}$$

E^p is determined by the inverse of the slope of the plot $\dot{\varepsilon}_z$ vs. σ_z (eq. 3.6). Several experiments are performed at constant loads for calculating the uniaxial viscosity.

Up to now, viscous Poisson's ratio has been calculated using its definition:[74]

$$\nu^p = \frac{\dot{\varepsilon}^{free} - \dot{\varepsilon}_r}{\dot{\varepsilon}_z - \dot{\varepsilon}^{free}} \tag{3.7}$$

However, a second method has been derived. It is believed to be more robust as more than two experiments (free and sinter-forged experiments) can be taken into account to compute it. The overall driving force, p, during sinter-forging is:

$$p = \frac{\sigma_z}{3} + \Sigma \tag{3.8}$$

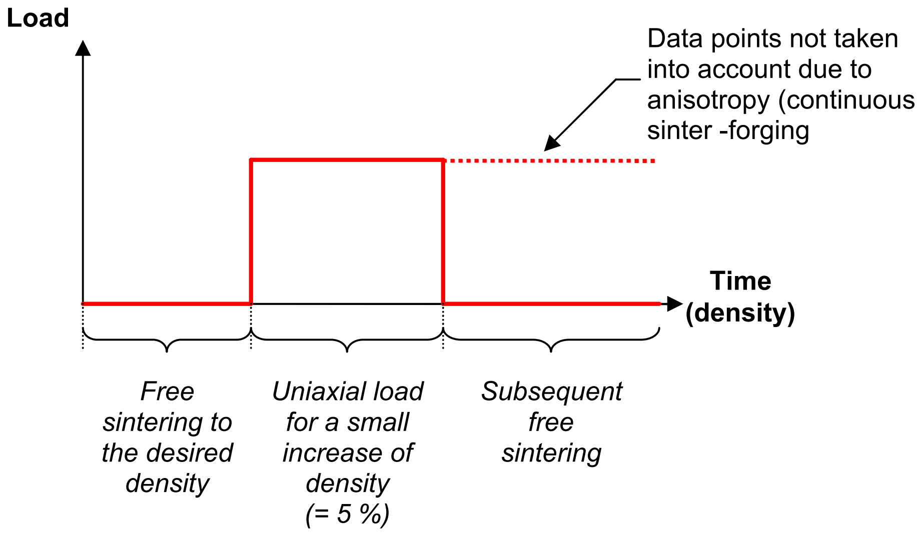

Figure 3.3: Continuous and discontinuous sinter forging.

Note that the application of an external load acts as an additional driving force for densification.

The volumetric densification rate is expected to vary as the first power of the driving force:[73]

$$\dot{\varepsilon}_v = 2 \cdot \dot{\varepsilon}_r + \dot{\varepsilon}_z = \frac{1}{K^p} \cdot p \tag{3.9}$$

where $\dot{\varepsilon}_v$ is the volumetric strain rate. From eq. 3.8 and eq. 3.9 we can deduce:

$$\dot{\varepsilon}_v = 3 \cdot \dot{\varepsilon}^{free} + \frac{1}{K^p}\frac{\sigma_z}{3} \tag{3.10}$$

Similarly to the calculation of the uniaxial viscosity, the bulk viscosity is determined by the inverse of the slope of the plot $\dot{\varepsilon}_v$ vs. $\frac{\sigma_z}{3}$. Having previously measured the uniaxial viscosity, the viscous Poisson's ratio is then calculated from the equation derived from eq. 2.11:

$$\nu^p = \frac{3K^p - E^p}{6K^p} \tag{3.11}$$

Continuous and discontinuous sinter-forging

As we have seen previously, to compute the uniaxial viscosity and the viscous Poisson's ratio as function of density, a load needs to be applied during densification. Two methods

Sintering temperature	76%	80%	85%	90%	95%	97%
820 ° C	10, 20, 40 N	10, 20, 40, 80 N	10, 20, 40, 80 N	20, 40, 80 N	20, 40, 80 N	20, 40, 80 N
840 ° C	10, 20, 40 N	10, 20, 40 N	10, 20, 40 N	20, 40, 80 N	20, 40, 80 N	20, 40, 80 N

Table 3.2: CSF experiments carried out at 820 ° C and 840 ° C with different loads.

to apply the load during sinter-forging are distinguished (figure 3.3):

- continuous sinter-forging (**CSF**)
- discontinuous sinter-forging (**DSF**)

For CSF, the load is applied from a defined density and is maintained until the final density is reached. This method assumes implicitly that the load has no effect on the measured sintering parameters. For DSF, the load is either applied (i) for a small increase of density or (ii) up to the final density. However, for the second case, the sintering parameters are only computed for a small increase of density. After the small increase of density where the load is applied, anisotropy is believed to be introduced (§ 2.4).

Sinter-forging experiments were performed at two isothermal temperatures of 820 ° C and 840 ° C. The heating rate was 30 ° C/min in order to limit the densification before the isothermal plateau is reached. The magnitude of the loads was ranging from 10 to 80 N ($\approx$ 0.1 to 0.8 MPa, respectively). The experiments are summarized in table 3.2.

3.3.2 Subsequent free sintering

At a defined density, the load can be released (figure 3.3). Radial and axial strains are recorded as a function of time. The ratio of axial to radial strains is compared to free sintering experiments (when no previous load is applied). The difference indicates if anisotropy is induced in the bulk sample and allows to adjust the density range for which DSF may be performed.

3.3.3 Zero radial shrinkage

During densification, the shrinkage in the r-θ plane of cylindrical samples (figure 3.2) can be achieved by adjusting continuously the applied uniaxial stress. The applied uniaxial stress is coupled with the measured radial strain. This mode is activated as soon as the sample begins to shrink. Both radial and axial strains as well as the uniaxial load maintaining the zero radial strain are recorded simultaneously. This experiment is similar to constraining a film on a rigid substrate. However, in this case, the applied stress is compressive and thus enhances the densification.

Constraining substrate	Symmetric/ Asymmetric	LTCC thickness	Substrate thickness
Dense alumina	Asymmetric	1 layer (245 μm)	624 μm
Green alumina tape	Asymmetric	12 layers (2940 μm)	3 layers (735 μm)
Green alumina tape	Symmetric	12 layers (2940 μm)	3 layers (735 μm)
Dense LTCC	Asymmetric	8, 5, 3 layers (1960, 1225, 735 μm)	180-230 μm

Table 3.3: Experiments on constrained sintering.

3.4 Sintering of laminates

3.4.1 Free sintering

The densification behavior of laminates freely sintered is measured in the sinter-forging facility. Therefore, twelve layers are laminated together to ensure a minimal thickness measurable by the laser scanner. Green laminate dimensions are: 30×10×3 mm^3.

3.4.2 Constraining substrates

Three different constraining substrates are used:

- ceramtape A (CeramTec AG, Plochingen, Germany)
- rubalit 708 S (CeramTec AG, Plochingen, Germany)
- dense LTCC

Ceramtape A is a green alumina tape and does not densify below 900 ° C. The green tape is 284 μm thick. Rubalit 708 S is a dense alumina substrate and is 624 μm thick. As Cai *et al.*[56] mentioned, alumina below 950 ° C can be considered to be purely elastic. Dense LTCC substrates (Ceramtape GC) are previously sintered at 840 ° C for 2 hours under a small load in order to remain perfectly flat. Layer thicknesses are 180, 220 and 230 ± 3 μm. Experiments which are presented in the next 3 sections are summarized in table 3.3.

3.4.3 Rocking arm

Measurement of the shrinkage behavior of constrained films is challenging. Normal dilatometry techniques are not able to measure properly the sintering behavior of films as the pushrods exert a non-negligible load on to the sample. Thus, few techniques have been developed in order to measure the shrinkage behavior of films. An optical technique can be used: a silicon wafer is placed above the film, and depending on its orientation deviates a laser beam which allows to compute the film thickness.[110;156]

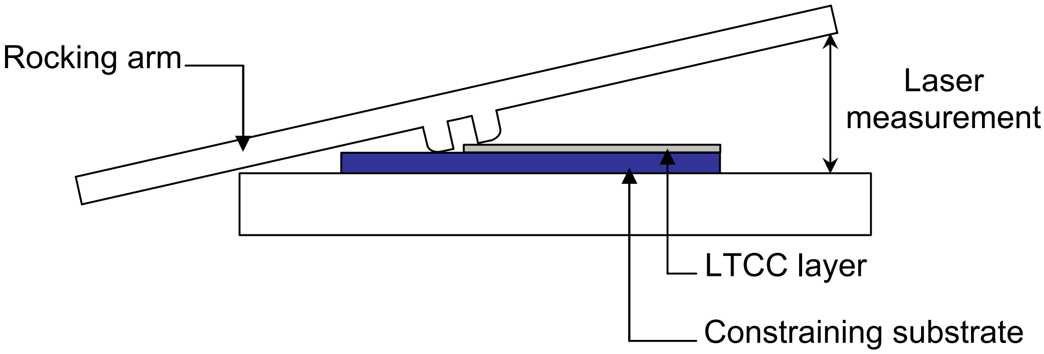

Figure 3.4: Schematic of the rocking arm.

A new method has been developed in the ceramics group at TU Darmstadt. One leg of a beam rests on the substrate, whereas the other one rests on top of the film (figure 3.4). Owing to the specific geometry, negligible load is applied onto the surface (no effect could be observed with HR-SEM). The distance between the bottom alumina substrate and the rocking arm is measured by a vertical laser scanner (resolution ± 0.5 μm). Film strains are geometrically amplified by a factor of 10. Hence, the resolution of the measure of the film thickness is ± 50 nm.

Densification behavior is measured for a single layer laminated on a dense alumina substrate. Density during sintering of the constrained film is calculated by setting $\varepsilon_r = 0$ in equation 3.3. The sintering temperature program is identical as before: the heating is $30\,^\circ$C/min up to $840\,^\circ$C.

3.4.4 Sintering of a symmetric laminate

To prevent camber, the LTCC layer is constrained on both sides (symmetric laminate). Green alumina tapes are used as constraining substrates and offer the advantage that they can be easily removed after sintering. Densification behavior is determined by measuring the density by the Archimedes method[159] for several samples sintered at $840\,^\circ$C for different times.

3.4.5 Sintering of an asymmetric laminate

Camber is investigated for asymmetric laminates (bi-layers - figure 2.16) with two different constraining materials: dense LTCC substrates and green alumina tapes. With dense LTCC substrates as constraining substrates, camber is investigated for 3 different initial thickness ratios: m = 3, 5 and 10 (eq. 2.33). With green alumina tapes as constraining substrates, camber is investigated for an initial thickness ratio of 3. Investigated bi-layers have a width and length of 4 mm and 27 mm, respectively.

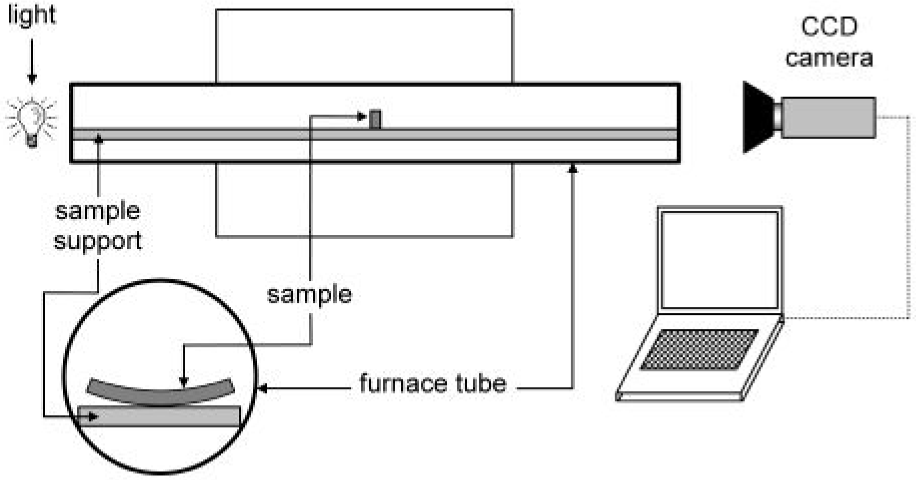

Figure 3.5: Schematic of the measurement of the camber.

A tube furnace with a transparent window is used (LK model tube furnace, HTM Reetz, Berlin, Germany) (figure 3.5). During the experiment, one picture is taken every 15 s (Canon - EOS 350D, Tele-converter 2X Soligor C/D7, 70-300 mm 1:4-5.6 APO - SIGMA). The obtained picture size is 3456×2304 pixel^2 and the resolution is 10 μm/pixel. Camber is then measured by fitting a circle on the contour of the bi-layer (National Institute of Health, Bethesda, Maryland - "contact angle" plug-in).

3.5 X-ray diffraction

X-ray diffraction is based on Bragg's law: when a monochromatic X-ray beam with wavelength λ is projected onto a crystalline material at an angle θ, diffraction occurs only when the distance traveled by the rays reflected from successive planes differs by a complete number n of wavelengths (constructive interference). The condition is expressed by:

$$n\lambda = 2d \cdot sin\theta \tag{3.12}$$

where λ is the wavelength of X-rays, d is the spacing between the planes in the atomic lattice, θ is the angle between the incident ray and the scattering planes and n is an integer. By varying the angle θ, the Bragg's Law conditions are satisfied by different d-spacings in polycrystalline materials. Plotting the angular positions and intensities of the resultant diffracted peaks of radiation produces a pattern, which is characteristic of the crystal.

To detect the presence of crystalline phases, X-ray diffraction is carried out on milled samples previously sintered at 840 ° C for different times and loads.

3.6 SEM and microstructure characterization

3.6.1 Polishing

Microstructure observation is performed on polished samples. Bulk samples are cut in the longitudinal plane parallel to the loading direction (plane r-z in figure 3.2), whereas laminates are cut in the plane along the thickness (plane r-z in figure 2.16). Samples are cold mounted in a resin (Buehler Epoplast). After curing the epoxy for 24 h in air at room temperature, the cross-sections are ground and polishing is firstly performed with SiC papers with grits from 320 to 1200 with water as lubricant; secondly with pastes of 6, 3, 1 and 0.25 μm diamond particles.

3.6.2 SEM

Micrographs are taken with a high-resolution scanning electron microscope (HRSEM, Model No. XL 30 FEG, Philips Electronic Instruments, Mahwah, NJ). As samples are electrically non-conductive, an ultra thin coating of gold/palladium is deposited by a sputter coater with a current of 40 mA for 40 s (Sputter Coater SCD050, Balzers).

3.6.3 Image characterization

Obtained SEM micrographs are analyzed quantitatively with the software Image J (National Institute of Health, Bethesda, Maryland). After contrast enhancement, images are filtered and then binarized (figure 3.6). Pore and particle orientations are determined by assimilating them to ellipses of equivalent area (figure 3.6). Note that pores or particles at the image borders are not fitted. Each pore / particle is characterized by its major axis, minor axis (a and b, respectively) and its orientation, θ (figure 3.7). The aspect ratio, R, is defined by:

$$R = \frac{a}{b} \tag{3.13}$$

To further characterize the microstructure, a few parameters are introduced:

- average pore / particle area
- proportion of elongated pores
- pore / particle orientation factor

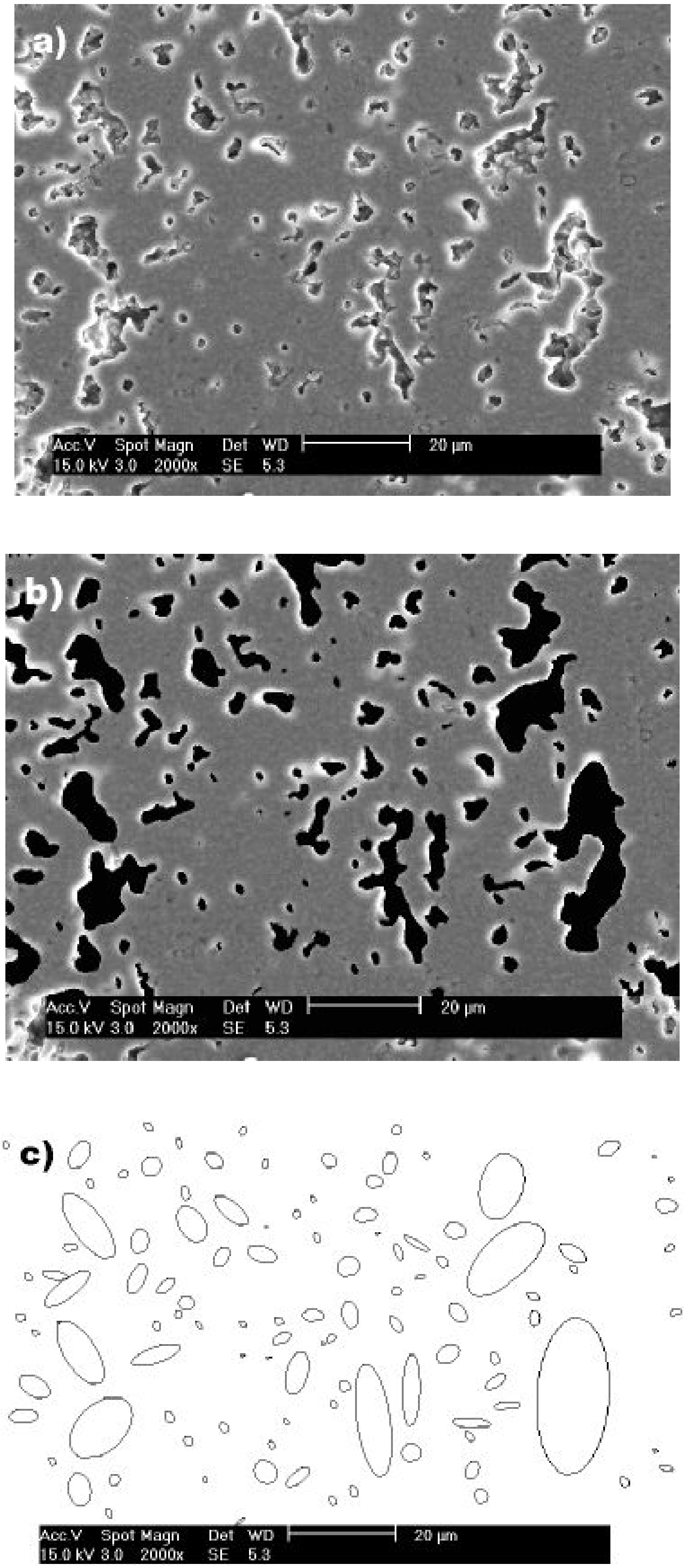

Figure 3.6: SEM micrographs, example of pore analysis: a) no image processing, b) pores are filled in black and c) pores are assimilated to ellipses.

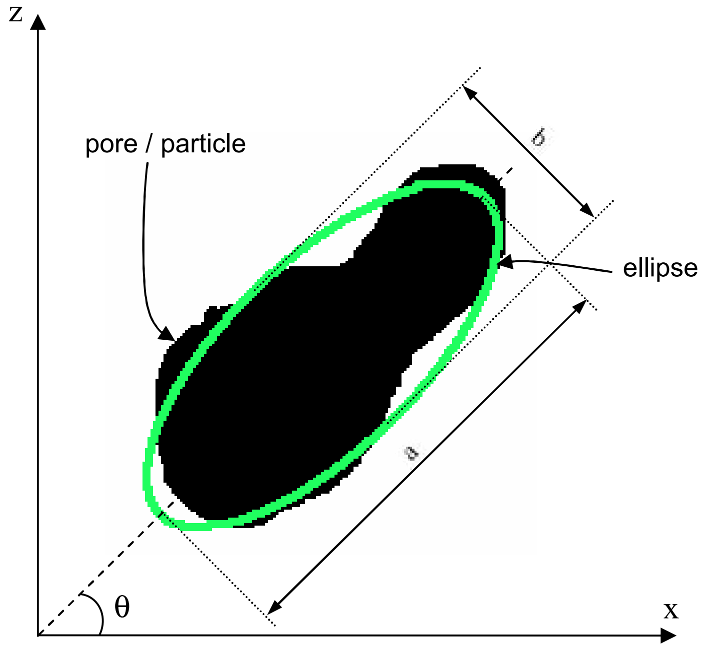

Figure 3.7: Pore / particle assimilated to an ellipse.

At least 300 pores and 400 particles for each sample are taken into account for quantitative analysis.

Note that the pore / particle area measured in 2D is smaller than the actual pore / particle size in 3D.

Pore shape is considered and the proportion of elongated pores, χ, is defined as:

$$\chi = \frac{n_{elong}}{n_{tot}} \tag{3.14}$$

where n_{elong} is the number of pores which have an aspect ratio higher than 2.5 and n_{tot} is the total number of pores.

To quantify anisotropy, the following pore / particle orientation factor, k_p, is defined as:

$$k_p = \frac{L_{horiz}}{L_{vert}} \tag{3.15}$$

where L_{horiz} is the cumulative length of pores / particles with an orientation lying between 0° and 30° and 150° and 180° and L_{vert} is the cumulative length of pores / particles with an orientation lying between 60° and 120° (0° corresponds to the r axis). The error bar is determined by the standard deviation of the data of the different pictures.

3.7 Mercury porosimetry

Pore size distribution is also measured by a mercury porosimeter (Pore Sizer 9320, Micromeritics, Norcross, GA) - ASTM D 4284[161]. The technique is based on capillary rise: a non wetting liquid (mercury) is forced to flow into the capillary. The pressure is a direct measure of the capillary radius by applying the equation of Young and Laplace:

$$p = \frac{-2\gamma_{LV}\cos\theta}{r} \tag{3.16}$$

where p is the pressure, γ_{LV} is the surface tension of the liquid-vapor interface, θ the contact angle between the liquid and the solid and r is the radius of the capillary. The following values are taken: $\gamma_{LV} = 0.485$ N/m and $\theta = 130°$.

The sample is placed in a penetrometer (sample holder). The penetrometer is firstly evacuated and then filled with mercury. Afterwards, a pressure is gradually applied and the volume of mercury intruded into the sample is recorded. Pore sizes in the range of ~ 5 nm to 200 μm can be measured. Two limitations for this measurement can be noticed: (i) only samples with open porosity ($<$ 92% of relative density) can be measured and (ii) pores are assumed to be circular in cross section. In reality, pore shape is more like ink-bottle-shaped; hence, eq. 3.16 gives a measure of the neck size and not of the actual pore size. Pore size distribution for laminates as well as bulk samples was measured for a density range from 70% to 90% of relative density.

3.8 Resonance frequency

Young's modulus is measured with a testing set-up RFDA-HT1750 (IMCE, Diepenbeek, Belgium - ASTM C 1259[162]). Samples with a rectangular shape are tested (figure 3.8). At room temperature, samples are supported by threads at the nodes. Nodes are located at $0.224\times L$ from each end (figure 3.8). A mechanical impulse is given to the sample. The specimen vibration is recorded by a microphone which is placed above an anti-node of the vibration mode (at the extremities or in the middle of the sample). The signal is further analyzed by applying a Fast Fourier Transformation.

Elastic modulus is calculated from the fundamental resonance frequency in the flexural mode, f:

$$E = \frac{0.94645 C m f^2 L^3}{w t^3} \tag{3.17}$$

where m is the weight, L the length, w the width, t the thickness and C is a shape factor depending on geometry factors and Poisson's ratio:

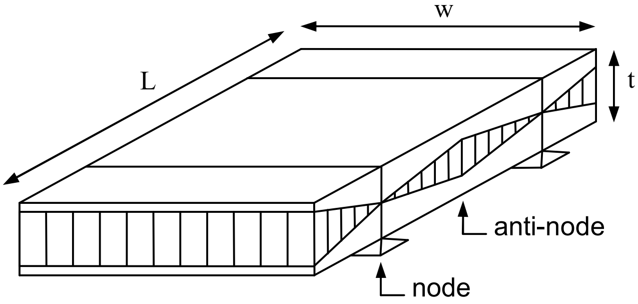

Figure 3.8: Schematic of the flexural vibration mode of rectangular bars.

$$C = \left\{ \begin{array}{l} 1 + 6.585\,(1 + 0.0752 \cdot \nu + 0.8109 \cdot \nu^2)\,(t/L)^2 - \\ \dfrac{100.083\,(1 - 0.2023 \cdot \nu + 2.173 \cdot \nu^2)\,(t/L)^4}{12 + 76.06\,(1 - 0.14081 \cdot \nu + 1.536 \cdot \nu^2)\,(t/L)^2} - 0.86806\,(t/L)^4 \end{array} \right\} \qquad (3.18)$$

At room temperature, measurement of the Young's modulus is performed on LTCC bulk samples at various relative densities (from 68% to 100%). Samples are cut longitudinally along the length of a bulk specimen. Sample size is about 2×8×18 mm^3.

The temperature dependence of Young's modulus is also measured for a fully sintered LTCC sample. The sample is placed in a furnace and is held by platine wires. The sample is cut from a laminate with a size of 2.5×12×30 mm^3.

Young's modulus of the green laminate is also measured during a heating ramp of 20 ° C starting from 600 ° C with a temperature plateau of 840 ° C. Twelve layers are laminated together and cut to the following dimensions: 3×12×35 mm^3. Burn-out of the binder and measurement is done during the same heating cycle. The data of interest are in the temperature range where the LTCC sinters, i.e. at temperatures higher than 700 ° C. At lower temperatures, Young's modulus is tricky to compute as the weight of the sample varies as function of temperature.

Chapter 4

Results

4.1 Free sintering

4.1.1 Bulk sample

Shrinkage behavior of freely sintered bulk samples is measured in the sinter-forging facility. Both axial and radial strains are computed as function of time (eq. 3.1 and eq. 3.2). Sintering begins during the heating ramp at a temperature of 780 ° C. A density of about 74.0% is measured at the beginning of the isothermal plateau. As can be seen in figure 4.1, bulk samples show a slightly anisotropic free sintering behavior: the difference between the axial and radial strains varies from +1.0% to -1.0% for a density range from 72% to 100%. The axial strain rate is initially lower than the radial strain rate but overtakes the radial strain rate at a relative density of about 74%. Axial strains become lower than radial strains at a relative density of about 91%.

4.1.2 Laminate

Shrinkage behavior of freely sintered laminates is also measured in the sinter-forging facility. Laminates begin to shrink at lower temperatures (about 730 ° C) than bulk samples (about 780 ° C). Anisotropy is more pronounced for laminates than for bulk samples: the difference between the axial and radial strains varies from +1.3% to -2.2% for a density range from 67% to 100% (figure 4.1). The axial strain rate is initially lower than the radial strain rate but overtakes the radial strain rate at a relative density of about 68%. Axial strains become lower than radial strains at a relative density of about 84%. No anisotropic shrinkage behavior in the plane of the laminate is expected as the sheets are alternatively laminated.

Density for both sample types is calculated at any time using eq. 3.3. Densification behavior of bulk samples and laminates is compared in figure 4.2. Laminates sinter slower

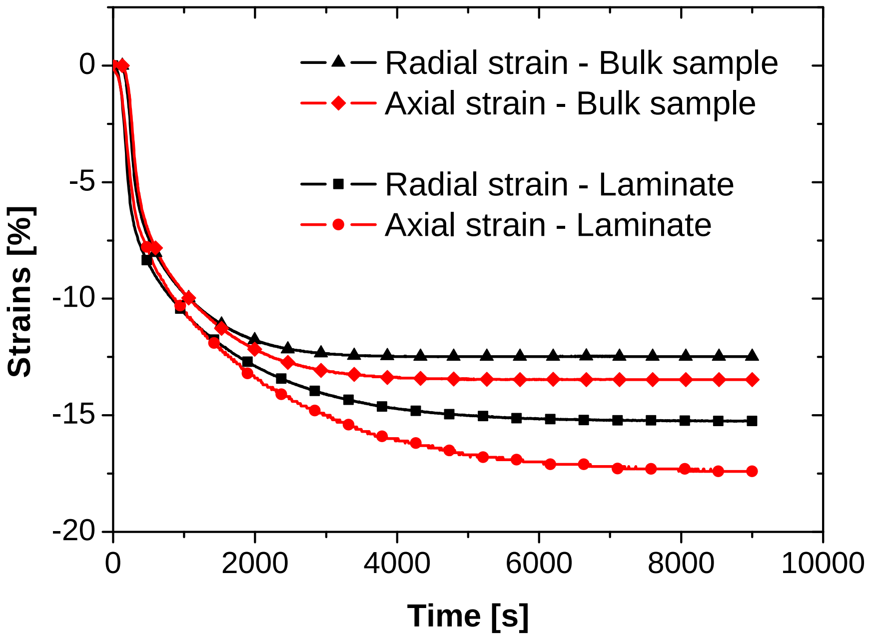

Figure 4.1: Axial and radial strains for a laminate and a bulk sample sintered at 840 ° C.

than bulk samples. Starting from a relative density of 70%, the time required to obtain full density is approximately the double for laminates than for bulk samples.

Pore size distribution was measured for laminates and bulk samples by mercury porosimetry (figure 4.3). Pores are larger in size for laminates than for bulk samples. During densification (from 70% to 90% of relative density), pore size remains constant for bulk samples but slightly decreases for laminates (figure 4.4).

4.1.3 XRD

Crystallization is not desired because of two reasons: (i) it can impede densification of the glass and (ii) affect the sintering parameters. Our goal is to study the sintering behavior over the largest range of density and to limit the variables under consideration. Indeed, if crystallization occurs, glass crystallizes mainly in anorthite.[143] Considering the ternary phase diagram in figure 3.1, the glass composition differs from anorthite: it is poorer in alumina. It implies that crystallization dissolves the alumina particles. Hence, the composition of the glass changes as densification /crystallization proceeds.

To detect the presence of crystalline phases, XRD has been used. Figure 4.5 displays the obtained XRD pattern for a milled bulk sample previously sintered at 840 ° C for 2 hours. The obtained samples are dense (figure 4.2). A single crystalline phase is recognizable: alumina (corundum), the filler present in the glass matrix. The amorphous phase

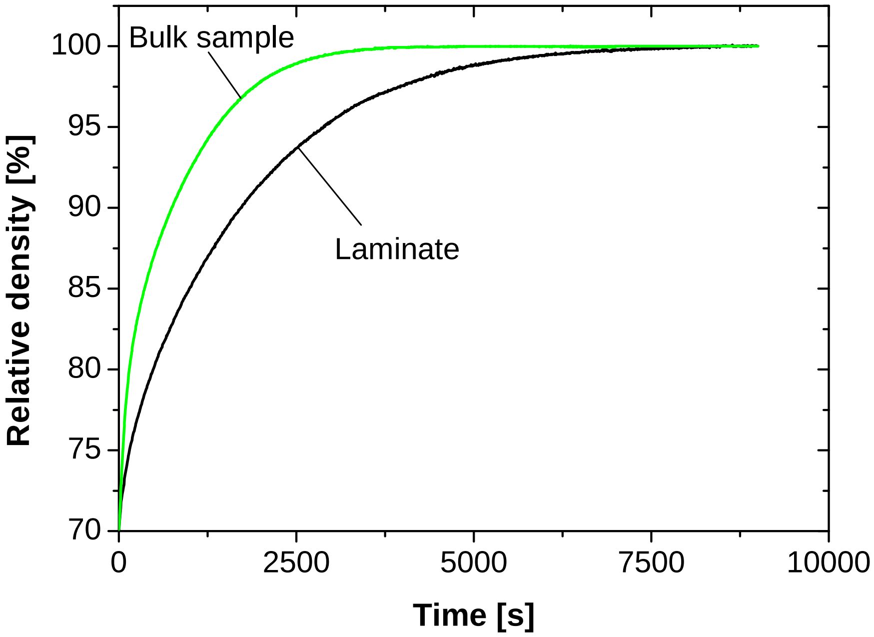

Figure 4.2: Densification behavior of bulk sample and laminate at 840 ° C.

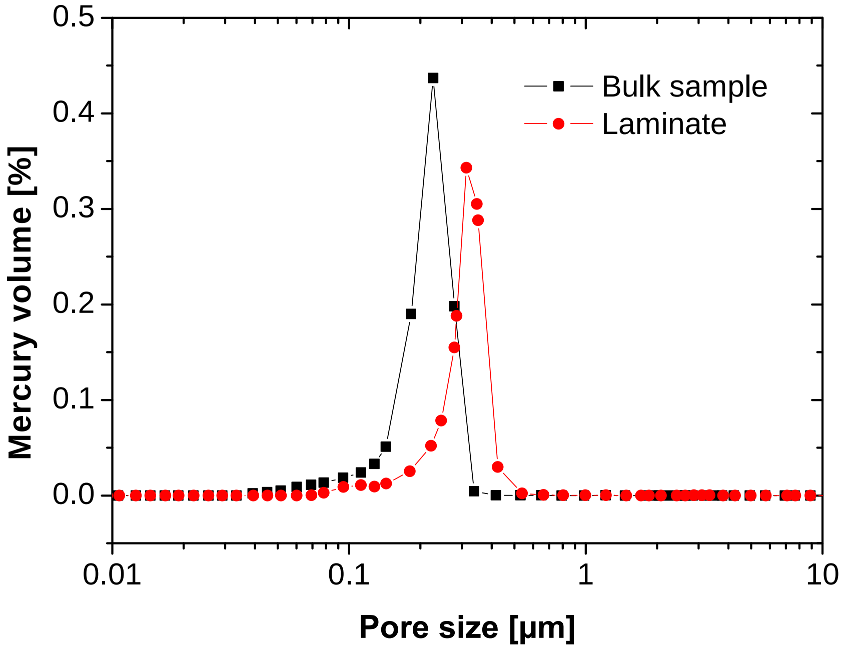

Figure 4.3: Pore size distribution of bulk sample and laminate at 90% of relative density.

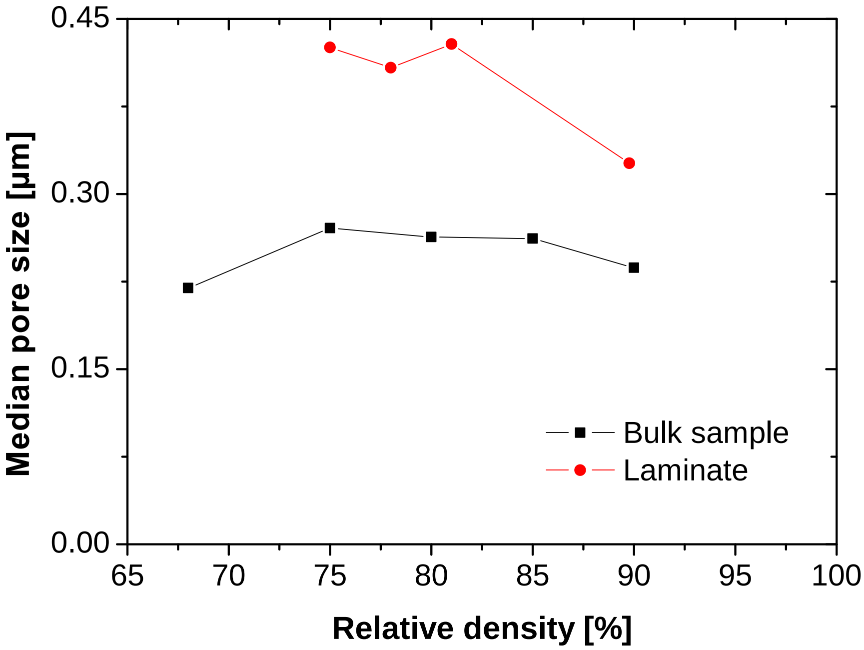

Figure 4.4: Median pore size as function of relative density for bulk samples and laminates freely sintered.

is detected indirectly via a broad and diffuse peak between 8 and 15°. Load application (from 10 to 80 N) and different sintering times did not influence crystallization.

4.2 Sinter-forging

4.2.1 Determination of the sintering parameters

In this section, the sintering parameters (E^p, ν^p and $\dot{\varepsilon}^{free}$) are measured as function of density. Particular attention is paid on the effect of loading on the uniaxial viscosity during the measurement. Density range for which the load is applied (CSF and DSF) and magnitude of the loads are investigated.

4.2.1.1 Free strain rate

Free strain rate is the first sintering parameter and is shown in figure 4.6 as function of relative density for two isothermal temperatures of 820 ° C and 840 ° C. Compared to the two other sintering parameters (uniaxial viscosity and viscous Poisson's ratio), no load needs to be applied to compute the free strain rate. Free strain rate decreases as densification proceeds and tends to zero as density tends to 100%. For the same density, free strain rates are higher at 840 ° C than at 820 ° C because densification is thermally activated.

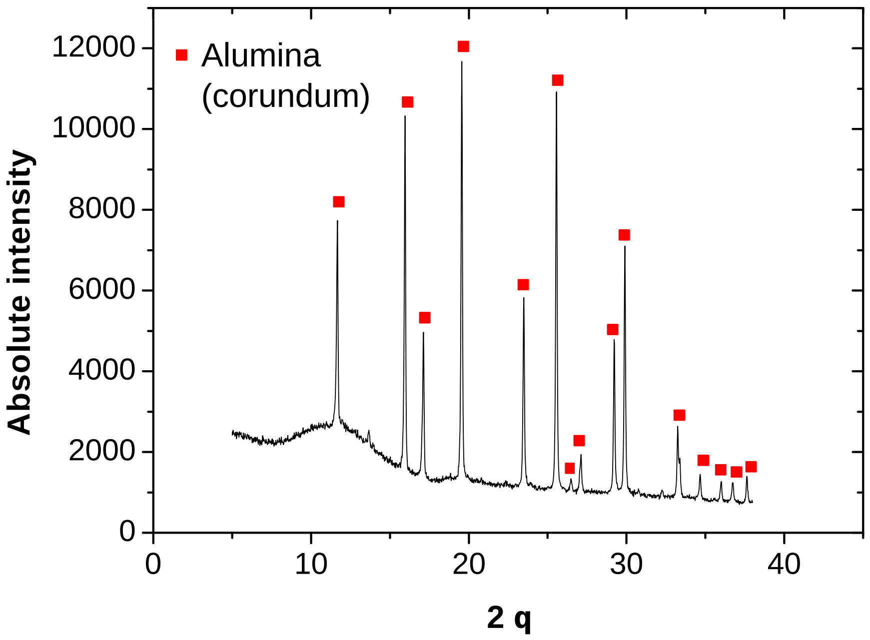

Figure 4.5: X-ray diffraction pattern on a milled bulk sample previously sintered at 840 ° C for 2 hours.

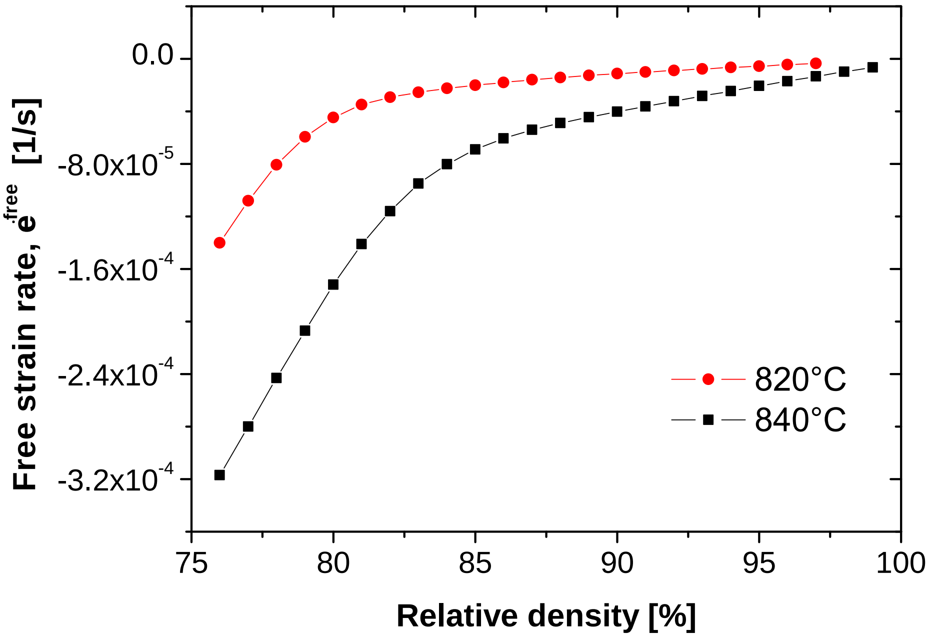

Figure 4.6: Free strain rate as function of relative density for bulk samples freely sintered at 820 ° C and 840 ° C.

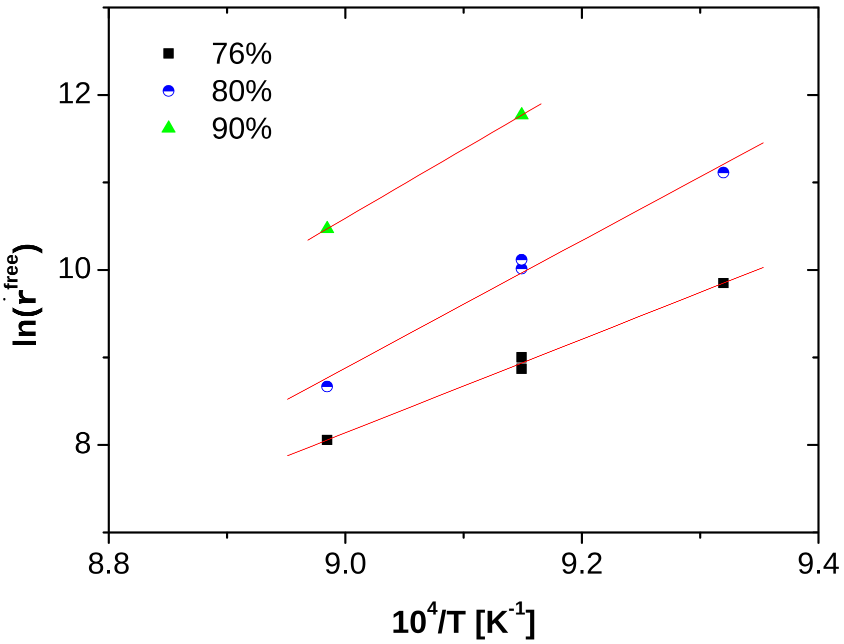

Figure 4.7: Densification rate as function of the inverse of temperature for relative densities of 76%, 80% and 90% for bulk samples freely sintered.

Activation energy

To determine the temperature dependence for densification, the activation energy has been determined considering the Arrhenius equation:

$$\dot{\rho}^{free} = \dot{\rho}_0^{free} exp\left(\frac{Q}{RT}\right) \tag{4.1}$$

where $\dot{\rho}_0^{free}$ is the pre-exponential factor, Q the activation energy and R the gas constant.

Three experiments on bulk samples are conducted at the isothermal temperatures of 800°C, 820°C and 840°C. According to eq. 4.1, the activation energy is determined by the slope of the plot $ln(\dot{\rho}^{free})$ vs. $(1/RT)$ at a given relative density. Figure 4.7 represents this plot for the relative densities of 76%, 80% and 90%. The activation energy remains approximatively constant during sintering: 611 ± 12 kJ/mol. Considering eq. 2.10 and since the viscous Poisson's ratio does not depend on temperature, uniaxial viscosity has the same activation energy as densification.

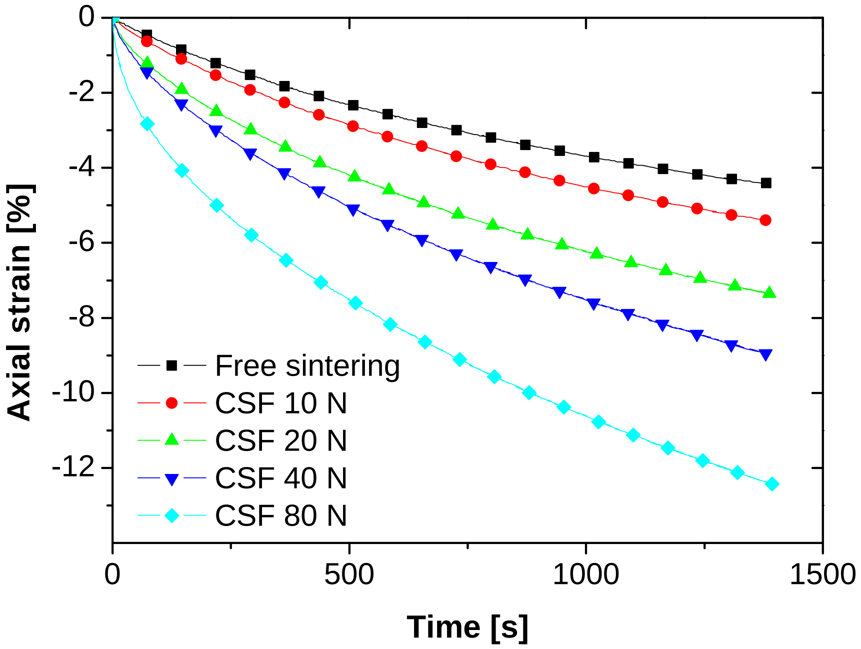

Figure 4.8: Axial strain curves: loads of 10, 20, 40, and 80 N are applied from 85% of relative density at 840 ° C.

4.2.1.2 Uniaxial viscosity

CSF and DSF

In a first step, CSF is performed from different relative densities (76%, 80%, 85%, 90%, 95% and 97%) with different loads (10, 20, 40 and 80 N $\approx$ 0.1, 0.2, 0.4 and 0.8 MPa, respectively) at 840 ° C. It is worth noticing that sample barreling is insignificant because of the use of low applied loads and the viscous nature of the material tested.

In figure 4.8, the axial strains for different CSF experiments starting from 85% of relative density ($t = 0$) are presented. As the load is applied, the axial strain increases (figure 4.8). The load promotes shrinkage in the axial direction and hinders shrinkage in the radial direction. In order to calculate the uniaxial viscosity, the sintering strain rates are obtained by fitting exponential functions to the curves shown in figure 4.8 and their time derivative is taken. The strain rates in the axial direction are found to vary linearly with the applied load at a given density. It is in good agreement with eq. 3.6. First, CSF curves are used to compute the uniaxial viscosity (figure 4.9). The purpose is to evaluate the density range after load application for which the load has no influence on the sintering uniaxial viscosity. Curves do not overlap, which means that the choice of 5% density data range of validity of the constitutive equations is too broad. It even seems to lie below 2%. For example, the uniaxial viscosity for a relative density of 86% calculated from the sinter-forging experiment where the load is applied at a relative density of 85% is higher

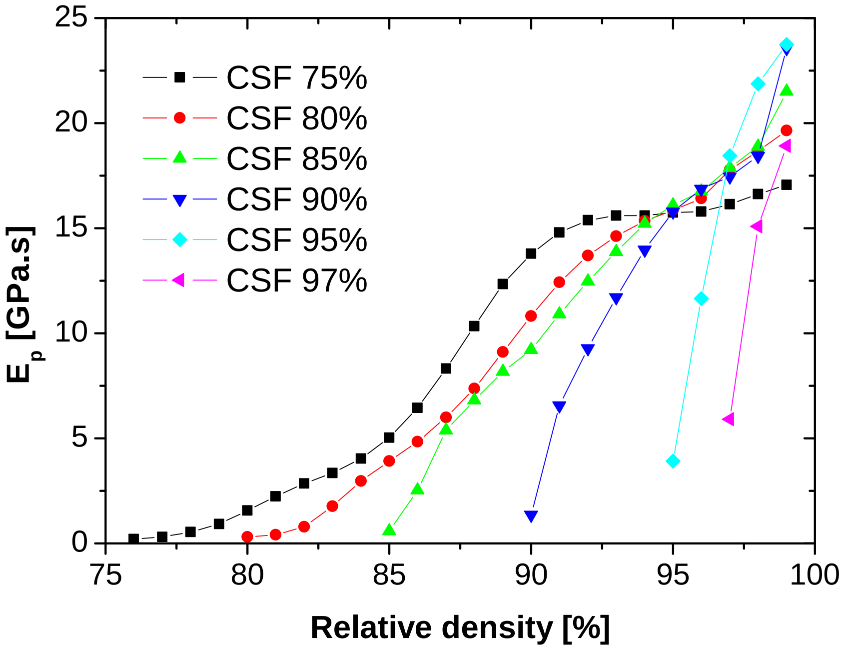

Figure 4.9: Uniaxial viscosity, E^p, as function of relative density for continuous sinter-forging experiments from 75%, 80%, 85%, 90%, 95%, and 97% of relative density at 840 ° C.

than the uniaxial viscosity at 90% calculated from the sinter-forging experiment where the load is applied at 90%. This result is ambiguous, as we expect the uniaxial viscosity to increase continuously with density (figure 2.11). The data in figure 4.9 therefore suggest that different degrees of anisotropy are induced in the different specimens.

To rationalize these results, the different axial strain rates for free and sinter-forging experiments with a load of 40 N are plotted in figure 4.10. The uniaxial viscosity is directly calculated from these data using eq. 3.6. As soon as the load is applied, the axial strain rate overtakes the free strain rate. The rate then decreases to a threshold value with increasing time of load application. The axial strain rate during a sinter-forging experiment then does not seem to depend on the starting density for which the load is applied. This effect is smaller but occurs faster for high densities. At this point, we assume that anisotropy occurs shortly after applying the load and that a maximum degree of anisotropy is reached. For E^p, this trend is less clear, as the uniaxial viscosity curves obtained for CSF experiments show a similar trend but do not clearly overlap.

At this stage, the most accurate data for the uniaxial viscosity are the first data points of each CSF curve, i.e. where the uniaxial load is believed not to induce anisotropy and hence does not influence the sintering parameters. The obtained curve is plotted in figure 4.11 (DSF). Results will be further validated.

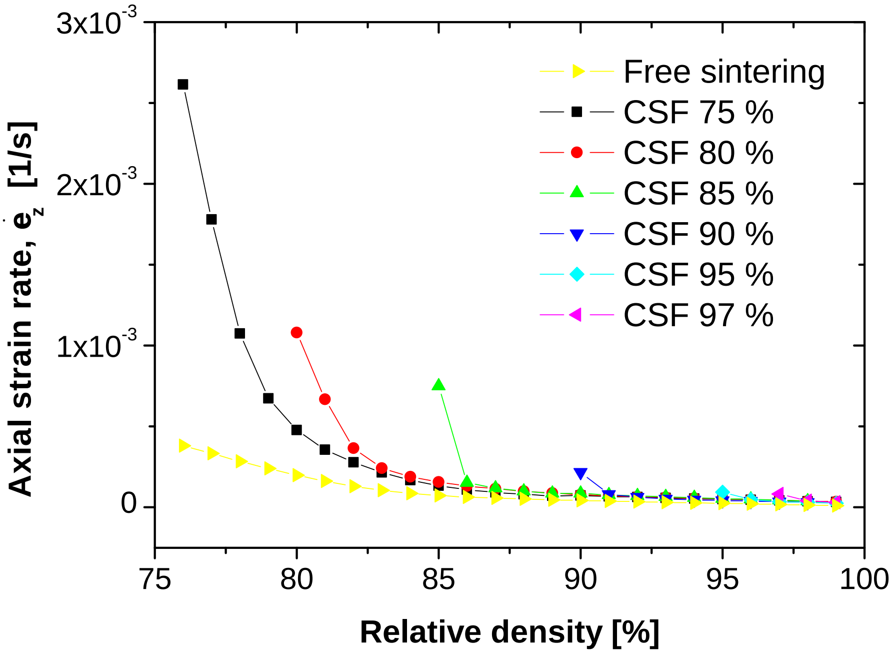

Figure 4.10: Axial strain rate, $\dot{\varepsilon}_z$, as function of relative density at constant load of 40 N for continuous sinter-forging experiment from 75%, 80%, 85%, 90%, 95%, and 97% of relative density at 840 ° C.

Magnitude of the load

To prevent the sintering material from developing anisotropy, another solution has been envisaged: to apply smaller loads and investigate its effect on the sintering parameters. CSF with small static loads of 1 and 2 N ($\approx$ 10 and 20 kPa) are performed. In these cases, weights are used and thus loads are applied during the entire firing cycle. Figure 4.11 represents the uniaxial viscosity calculated from two CSF experiments. With a small compressive stress of 1 N, the discontinuous and the continuous curves overlap until 90% of relative density. After 90%, the uniaxial viscosity values obtained from CSF experiments are lower. This phenomenon can be explained by the fact that, as the uniaxial viscosity increases, a load of 1 N is not large enough to induce a clear change in the axial strain rate compared with the free sintering case (eq. 3.6). This leads to a decrease of accuracy for the measured data. With a load of 2 N, the agreement is acceptable only below 82% of relative density. At higher densities, obtained values are higher than the uniaxial viscosity determined by DSF. At 97% of relative density, uniaxial viscosity is, however, smaller (10 GPa.s) than the one determined by CSF with large loads ($\sim$ 15 - 25 GPa.s) - figure 4.9.

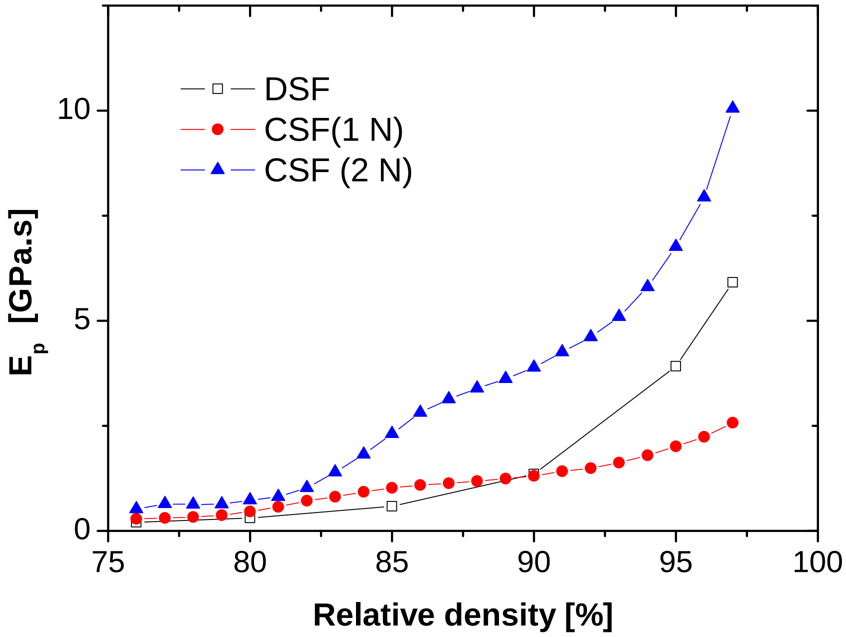

Figure 4.11: Uniaxial viscosity, E^p, as function of relative density for discontinuous sinter-forging experiment and for continuous sinter forging with load of 1 and 2 N at 840 ° C.

Validation of the results obtained

In order to validate the DSF results, we propose to compare free sintering experiments and subsequent free sintering for four different samples sintered at 840 ° C up to 90% of relative density (figure 4.12):

1. Freely sintered sample until 90% of relative density-**A1**
2. Sinter-forged sample for which a load of 40 N is applied between 89.5% and 90% of relative density-**A2**
3. Sinter-forged sample for which a load of 40 N is applied between 85% and 90% of relative density-**A3**
4. Sinter-forged sample for which a load of 40 N is applied between 75% and 90% of relative density-**A4**.

When both curves overlap, it means that the load, previously applied for a sinter-forging experiment, does not influence the sintering behavior and thus does not induce any anisotropy in the microstructure.

Directly after the load is removed, the sample expands in the axial direction and shrinks in the radial one (figure 4.13). We refer to this as "recovery effect". Note that

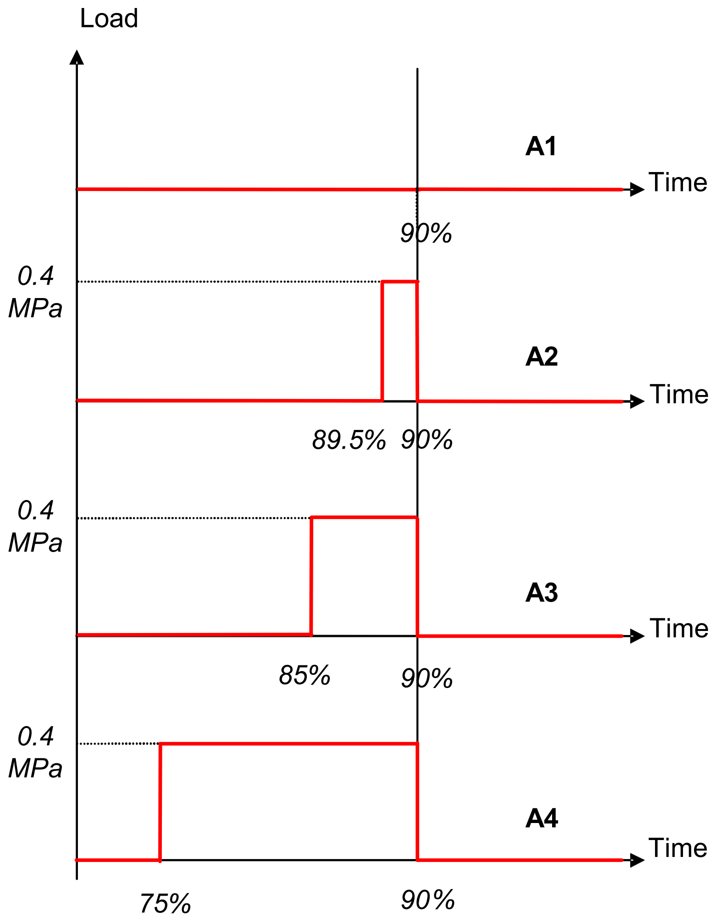

Figure 4.12: Freely sintered sample until 90% of relative density-A1, sinter-forged sample for which a load of 40 N is applied between 89.5% and 90% of relative density-A2, sinter-forged sample for which a load of 40 N is applied between 85% and 90% of relative density-A3, sinter-forged sample for which a load of 40 N is applied between 75% and 90% of relative density-A4.

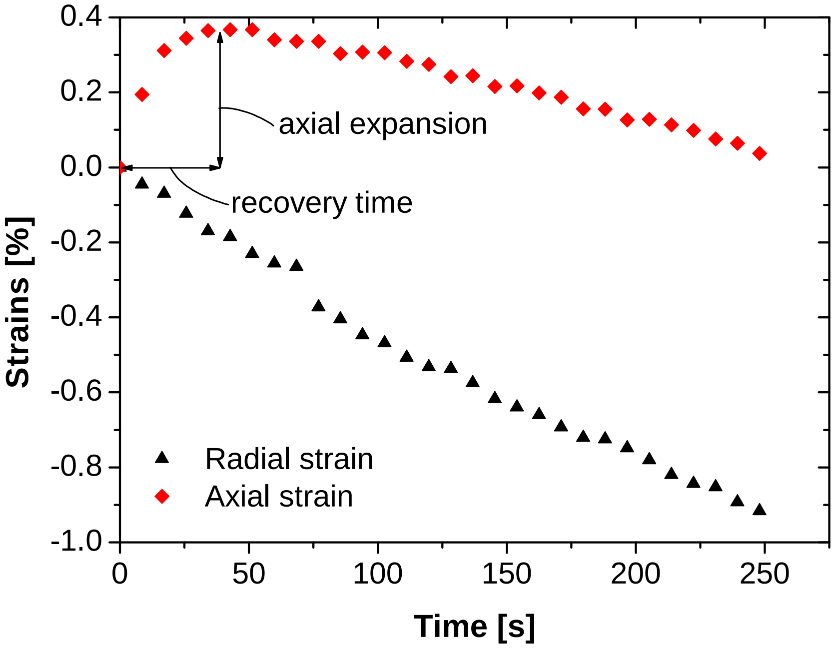

Figure 4.13: Subsequent axial and radial strains after applying a load of 40 N between 75% and 90% of relative density-A4.

this effect is not measurable in a standard loading dilatometer since the pushrod has to be in contact with the sample in order to measure the axial strains. The axial expansion as defined in figure 4.13 is 0.1, 0.25 and 0.39% for the samples A2, A3 and A4, respectively. After a short time (recovery time - figure 4.13), the sample shrinks again in the axial direction. Axial strains are then plotted in figure 4.14. If a load of 40 N is applied for a density increment of 0.5% (from 89.5% to 90% of relative density), the subsequent free sintering matches well with the free sintering experiment. This experiment validates each first data point of each sinter-forging experiment starting from different densities: the first data point is computed after load application for a 0.5% density increment (due to stabilization of the load). For both sinter-forging experiments, where the same load as before (40 N) is applied from 85% to 90% and from 75% to 90% of relative density, the subsequent axial strain has lower values than the free sintering experiments. Both curves of these two former sinter-forging experiments coincide, which suggests that anisotropy does not develop further if the load is applied for a larger density range. Therefore, we can conclude that a maximum of anisotropy is reached. This will be further confirmed by microstructural analysis in § 4.2.1.4.

Thus, only the first data points of each sinter-forging experiment are plotted in figure 4.15 (i.e. it corresponds to DSF with a validity range of 0.5% relative density). These new results conform with our expectations: the true uniaxial viscosity increases with density. This increase is even more remarkable as the density approaches 100%.

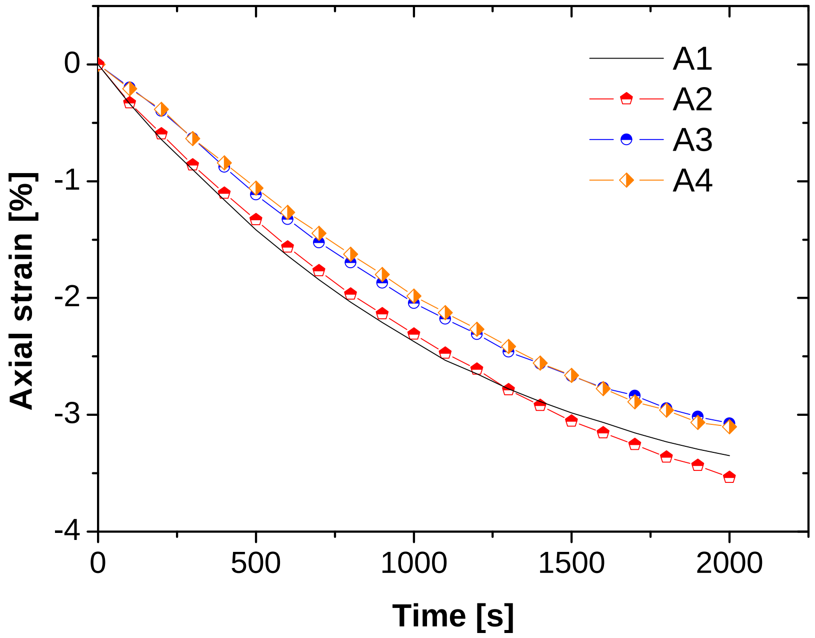

Figure 4.14: Axial strain, ε_z, as function of time from 90% of relative density on: for a freely sintered sample (A1), sinter-forged samples with a load of 40 N applied: between 89.5% and 90% (A2), between 85% and 90%(A3), and between 75% and 90% of relative density (A4).

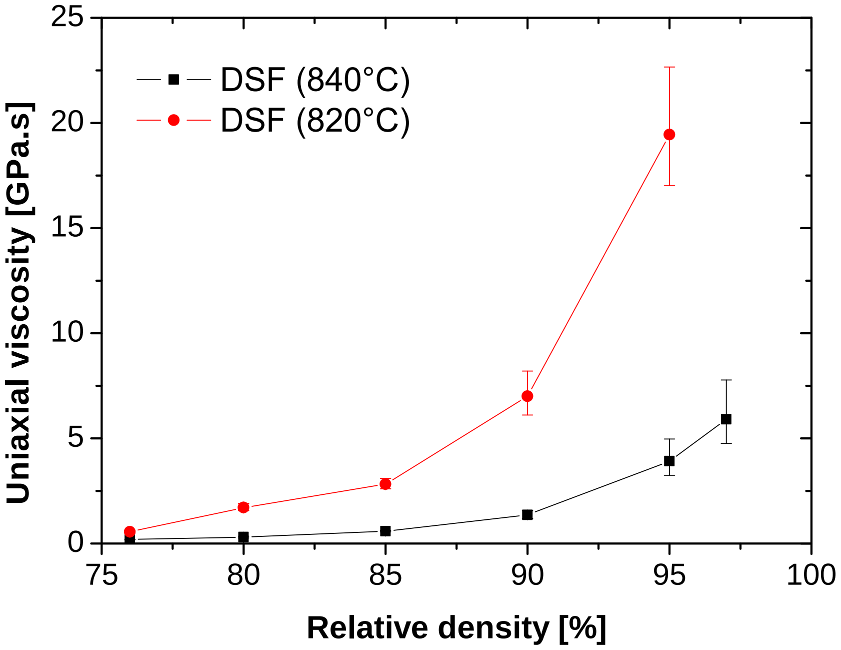

Figure 4.15: Uniaxial viscosity, E^p, as function of relative density from discontinuous sinter-forging experiments - isothermal temperature profile at 820 $^\circ$C and 840 $^\circ$C.

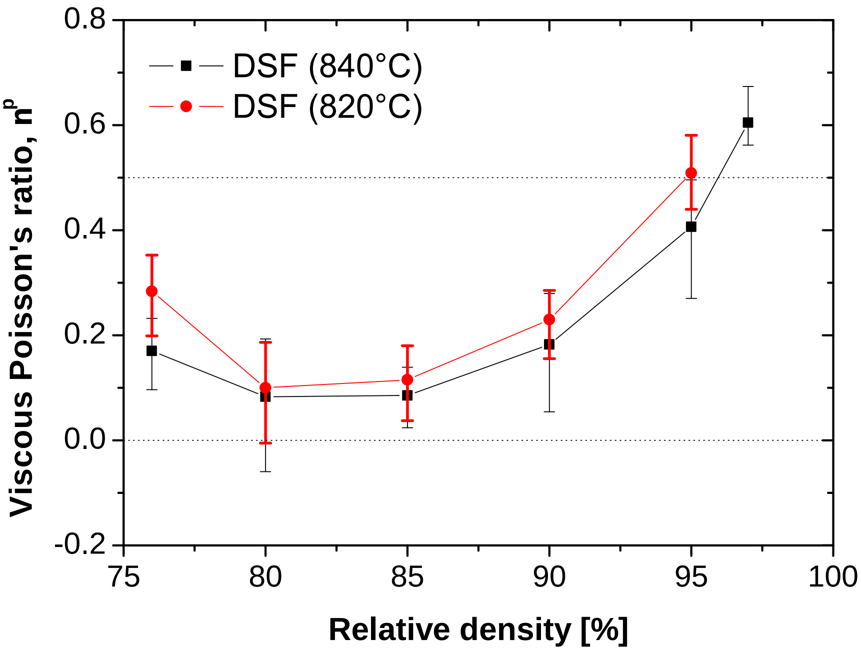

Figure 4.16: Viscous Poisson's ratio, ν^p, as function of relative density from discontinuous sinter-forging experiments - isothermal temperature profile at 820 ° C and 840 ° C.

Same procedure is used to determine the uniaxial viscosity at 820 ° C (figure 4.15). Both curves present the same trend and uniaxial viscosity at 840 ° C is lower than at 820 ° C, as expected for thermally activated properties.

Error bars increase as uniaxial viscosity increases as the uncertainty of the strain rate is larger at higher densities (strain rates are smaller).

4.2.1.3 Viscous Poisson's ratio

Bulk modulus is first computed (eq. 3.10) in order to calculate the viscous Poisson's ratio. As before, only the first data points of each CSF curves are computed in figure 4.16. Trend and values are in good agreement for both temperature profiles. Viscous Poisson's ratio decreases from about 0.25 to about 0.10 at low densities, remains constant up to 85% of relative density and further increases with density to reach values larger than 0.5.

4.2.1.4 Microstructure investigation

To correlate the microstructure and the effect of the load on the sintering parameters, microstructural characterization is performed on the samples A1, A3 and A4 sintered at 840 ° C. For the sample A2, since the load is applied only for a small increase of density, if the sample is cooled down under the load, the microstructure will be strongly affected

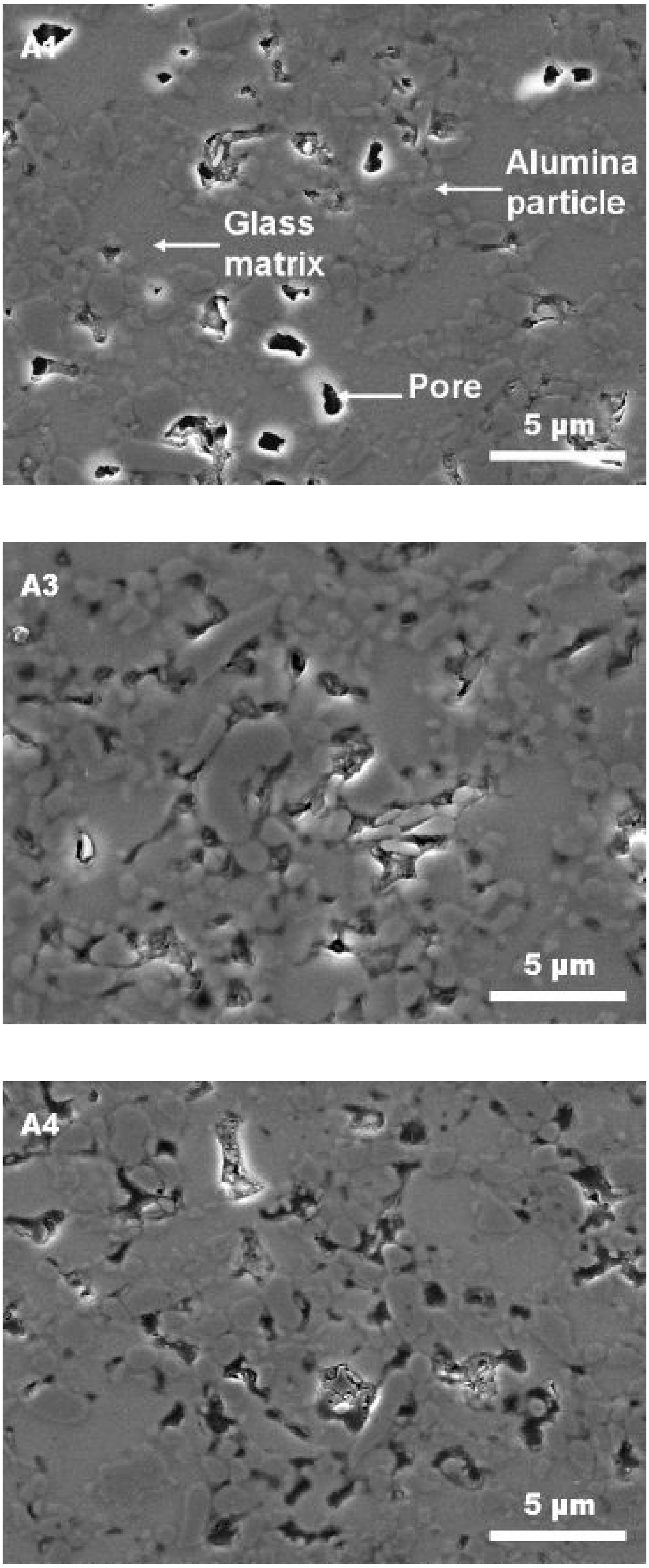

Figure 4.17: SEM micrographs of freely sintered sample until 90% of relative density (A1), sinter-forged samples with a load of 40 N applied: from 85% to 90% (A3) and from 75% to 90% (A4).

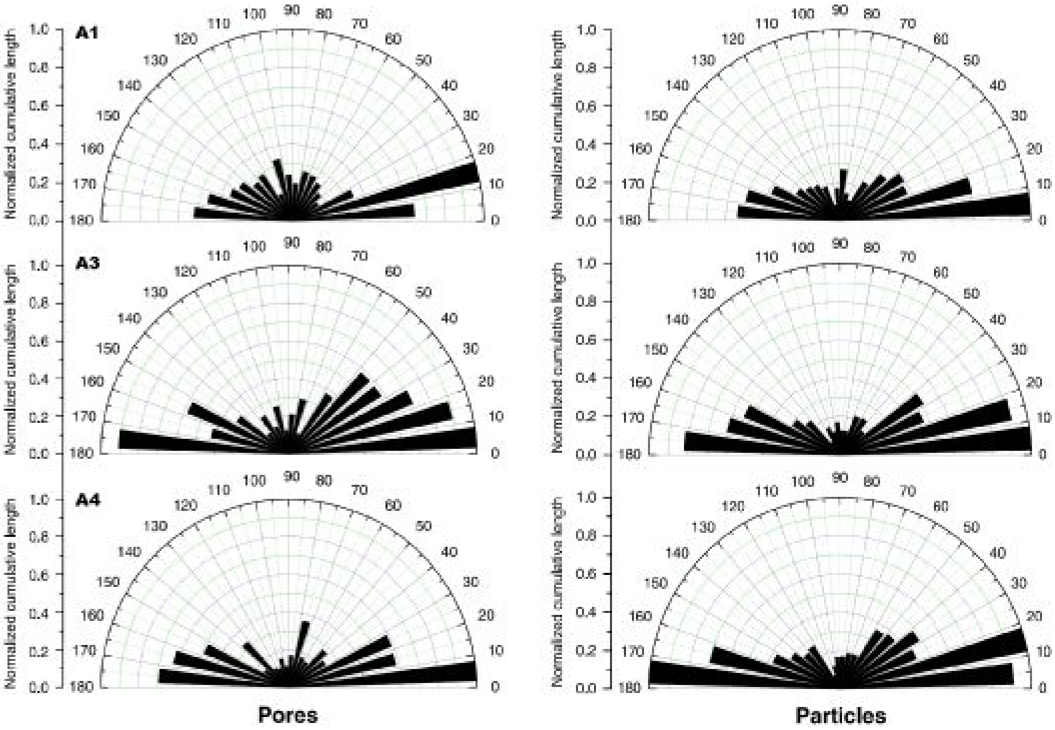

Figure 4.18: Pore and particle orientation of freely sintered sample until 90% of relative density (A1), sinter-forged samples with a load of 40 N applied: from 85% to 90% (A3) and from 75% to 90% (A4).

compared to the one before removal of the load (densification further takes place after shutting off the furnace). Thus, no microstructural characterization is performed on the sample A2. Micrographs are taken in the longitudinal plane parallel to the loading direction (figure 4.17). First, pore characteristics are considered in order to highlight the differences between the samples. Median pore area does not seem to be greatly affected by the sinter-forging conditions: 0.27, 0.29, and 0.24 μm^2 for A1, A3, and A4 samples, respectively. The shape of the pores is also considered and the proportion of elongated pores, λ, is 19%, 24%, and 26% for A1, A3, and A4 samples, respectively (eq. 3.14). This shows that highly anisometric pores exist after free sintering and that their proportion slightly increases as the load is applied for a larger density increment. Pore orientation is evaluated by cumulating pore length lying in a defined angle range. The calculation is restricted to pores that have an aspect ratio larger than 1.25, i.e. which show a sufficient degree of anisometry to determine a real orientation. The lengths are then normalized by the maximum value obtained for the specimen. Figure 4.18 shows for both sinter-forged samples a clear horizontal orientation of the pores, i.e. perpendicular to the load, whereas for the freely sintered sample, pores seem also to be oriented along the same direction, but to a smaller extent. The pore orientation factor (eq. 3.15) values for the samples A1, A3, and A4 are 2.3, 3.9, and 3.7, respectively (figure 4.19). For an isotropic material, k_p should be equal to 1. Similar results for both sinter-forged samples are obtained: anisotropy seems to develop asymptotically, so that the microstructure does not evolve

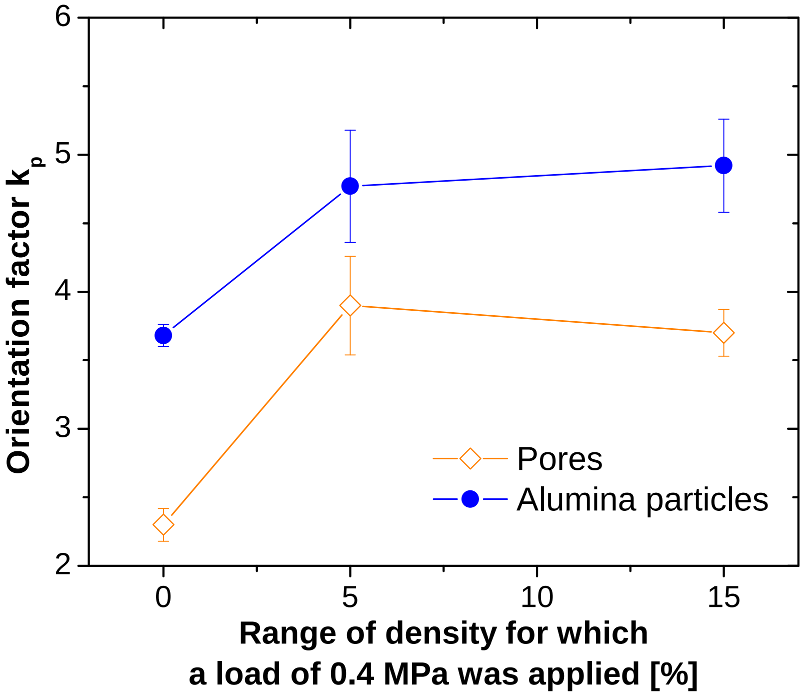

Figure 4.19: Pore and particle orientation factor k_p as function of the density range of load application.

further whatever the time of load application may be.

Orientation of alumina particles is also monitored. The same experimental procedure used to determine pore orientation is followed, using the same SEM micrographs (figure 4.17). The mean aspect ratio of alumina particles is found to be about 1.5: a particle orientation then can be defined. Results are presented in figure 4.18 and show similar results as the pore characteristics. For both sinter-forged samples, particle orientation is more pronounced than for the freely sintered sample. For the freely sintered sample, the particle orientation factor k_p is equal to 3.6 whereas it is 4.8 and 4.9 for sinter-forged specimens A3 and A4, respectively. If the particle orientation factor is plotted as function of density range for which the load is applied (figure 4.19), it can be clearly seen that pore and particle orientation follow the same trend. Moreover, the particle orientation factor is always higher than the pore orientation factor, which may signify that anisotropy is controlled by the orientation of the alumina particles.

4.2.2 Elastic properties of the LTCC material during sintering

In order to verify whether the sintering body can be considered as purely viscous during sintering, Young's modulus has to be determined. The density dependence of Young's modulus is first measured and is shown in figure 4.20. Between 76% and 100% of relative

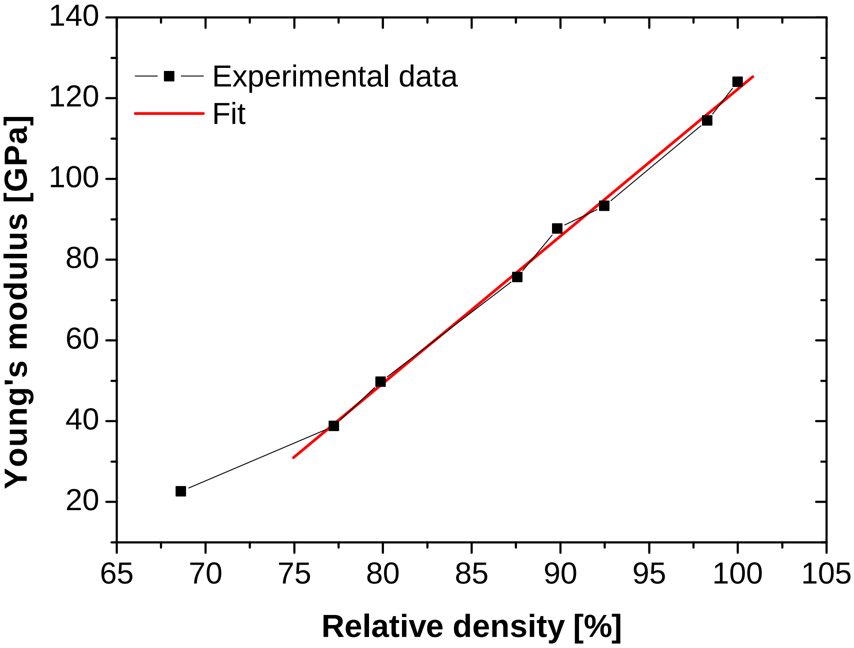

Figure 4.20: Young's modulus as function density (measured at RT).

density, Young's modulus increases linearly with density and varies from 23 GPa to 124 GPa.

$$E = E'(\rho) = -242.37 \cdot 10^9 + 364.68 \cdot 10^9 \rho \tag{4.2}$$

Young's modulus for a fully sintered laminate has been measured as function of temperature (figure 4.21). Up to about 600 $^\circ$ C, Young's modulus decreases linearly with temperature. Between 650 $^\circ$ C and 750 $^\circ$ C, there is an abrupt change of the tangent of the curve caused by the glass transition ($\sim$ 720 $^\circ$ C). At higher temperatures, the intensity peak of the resonance frequency decreased rapidly which explains the scatter of the results. The curve is fitted by a polynomial function of the 6^{th} order:

$$E = E''(T) \tag{4.3}$$

To determine Young's modulus of the porous body during sintering, it is assumed that the temperature dependence does not depend on density. Hence, we obtain:

$$E(\rho, T) = \frac{E'(\rho)E''(T)}{E_0} \tag{4.4}$$

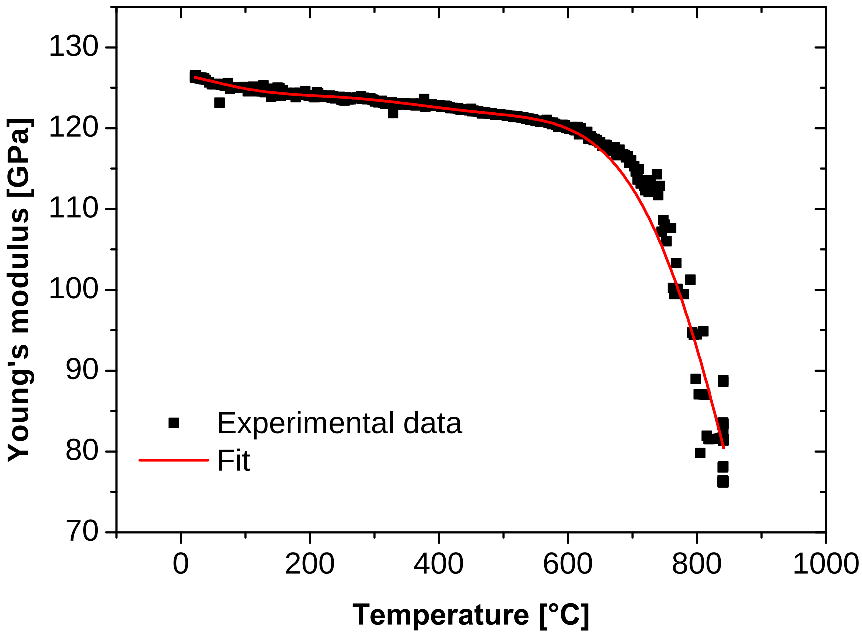

Figure 4.21: Young's modulus as function of temperature for a fully sintered laminate.

with $E_0 = E(100\%, 22^\circ C)$

Figure 4.22 provides Young's modulus as function of relative density at 840 ° C as well as the uniaxial viscosity. Young's modulus increases as relative density increases. At 76% of relative density, Young's modulus is 33 GPa whereas it reaches 71 GPa at 97% of relative density.

Relaxation time (eq. 2.8) is plotted in figure 4.23 for both temperatures of 820 ° C and 840 ° C. Relaxation time increases as density increases: as density increases, the uniaxial viscosity increase is stronger than the Young's modulus increase. Relaxation time is larger at lower temperatures: as the temperature decreases, the uniaxial viscosity decrease is stronger than the Young's modulus increase. However, relaxation time remains very low: under 0.1 s and 0.2 s for bulk samples sintered at 840 ° C and 820 ° C, respectively. Thus, the elastic behavior is negligible compared to the viscous behavior of the material.

4.2.3 Zero radial shrinkage

In figure 4.24, radial and axial shrinkage are plotted as function of loading time. Radial strain is maintained to 0 ± 0.15%. Compared to free sintering, axial strains are much larger in absolute value since densification takes place only in the axial direction. The applied uniaxial compressive load is recorded and plotted as function of density in figure 4.25. At low densities, the compressive load increases up to about 91% of relative density and further decreases to zero as relative density approaches 100%. By setting

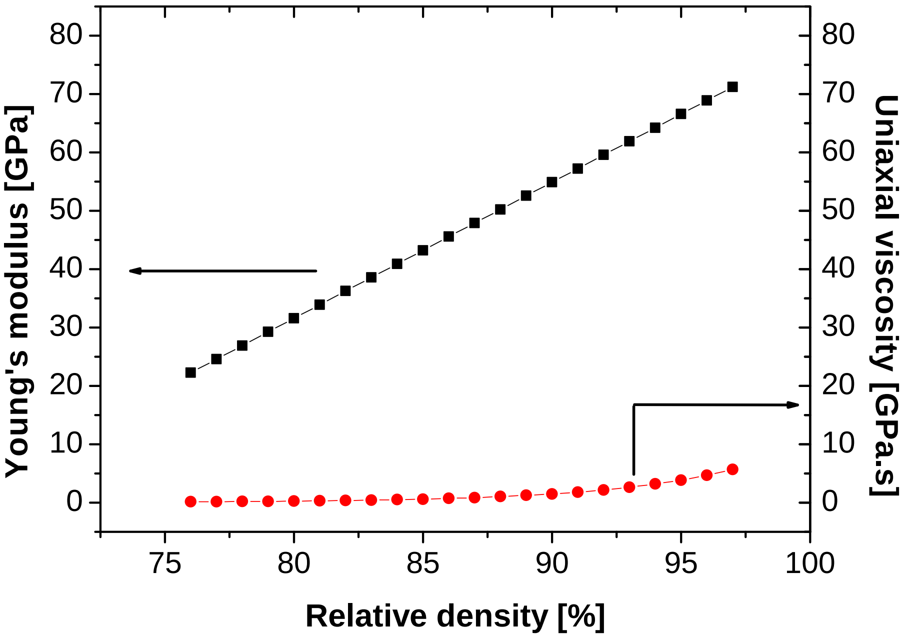

Figure 4.22: Young's modulus and uniaxial viscosity as function of relative density at 840 ° C.

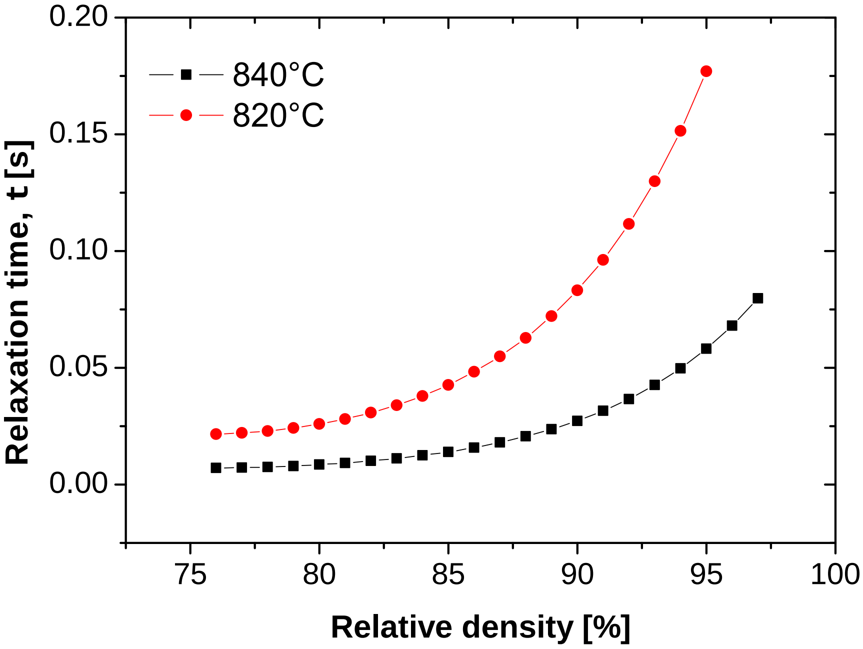

Figure 4.23: Relaxation time, τ, at 820 ° C and 840 ° C.

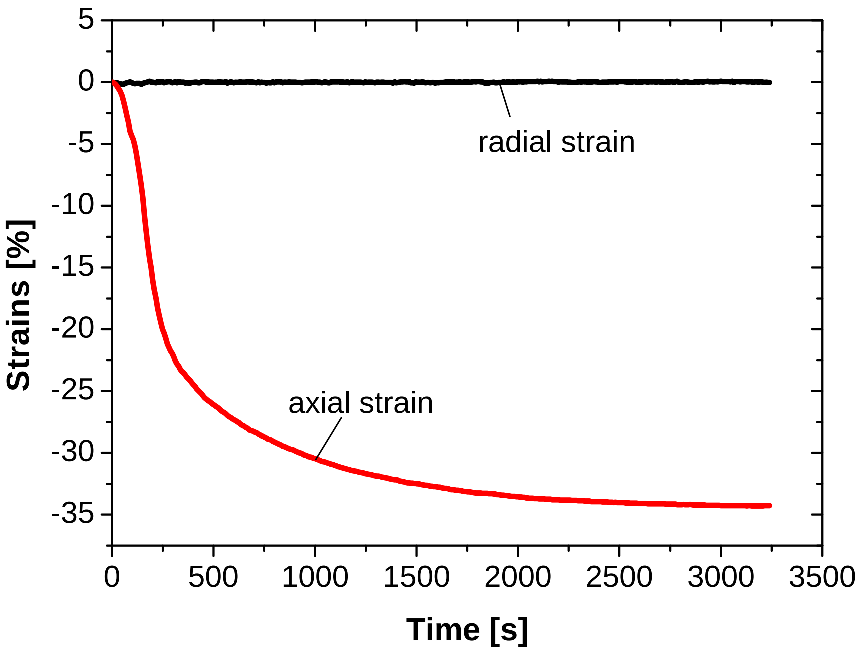

Figure 4.24: Radial and axial strain as function of time for zero radial shrinkage experiment.

$\dot{\varepsilon}_r = 0$ in eq. 3.5, the uniaxial compressive stress needed to obtain zero radial shrinkage is:

$$\sigma_z = \frac{\dot{\varepsilon}^{free} E^p}{\nu^p} \tag{4.5}$$

Knowing the sintering parameters previously measured, the predicted stress is plotted as function of density. Up to 80% of relative density, model and experiment agree quite well but at higher densities, predicted stresses are lower than the one measured (figure 4.25). The highest predicted compressive stress (0.6 MPa) is obtained at 80% of relative density and is almost three times lower than the highest measured compressive stress. During this experiment, a large degree of anisotropy may be induced and hence modify the sintering parameters.

In order to show that anisotropy is induced, the radial to axial strain rate ratio is plotted for subsequent free sintering experiments starting from 80%, 85%, 90% and 95% of relative density. As can be seen in figure 4.26, the ratio is larger than 1 for every experiment, i.e. radial strain rate is higher than axial strain rate. Anisotropy is not directly plotted after the load is removed ($t = 0$) because of the presence of the "recovery effect" (§ 4.2.1.2). The axial expansion is 0.1%, 0.25%, 0.5% and 0.65% for subsequent free sintering experiments starting from 80%, 85%, 90% and 95% of relative density, respectively.

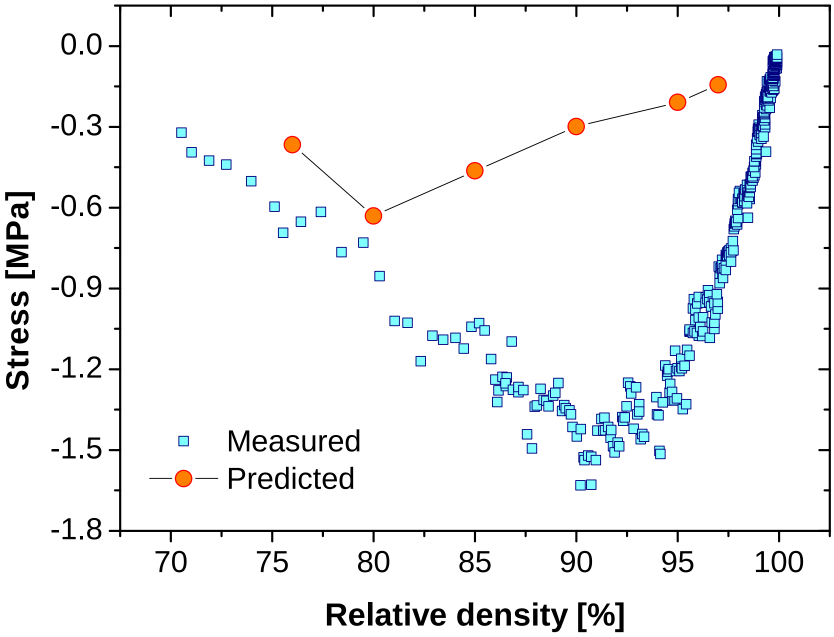

Figure 4.25: Uniaxial compressive stress needed to produce zero radial shrinkage experimentally measured and calculated.

The radial to axial strain rate ratio decreases rapidly after removing the load until reaching a plateau value. When the load is applied for a longer density range, the ratio of the anisotropy in the free strain rates decreases more slowly. The maximum increases with the density range where the load is applied. It indicates that the bulk sample becomes more anisotropic as the stress is applied for a longer time. This experiment is different from experiments A3 and A4 for which a maximum of anisotropy was found to be reached. For the samples A3 and A4, properties were compared at the same density and the magnitude of the load previously applied was identical for both experiments. This is not the case for the zero radial shrinkage experiment.

4.3 Sintering behavior of laminates

In this section, sintering behavior of symmetric and asymmetric laminates is studied. Three new models are derived to simulate the stress built into the LTCC layer for three different cases:

- asymmetric laminate: elastic substrate / LTCC material
- symmetric laminate: elastic substrate / LTCC material / elastic substrate
- symmetric laminate: viscous substrate / LTCC material / viscous substrate

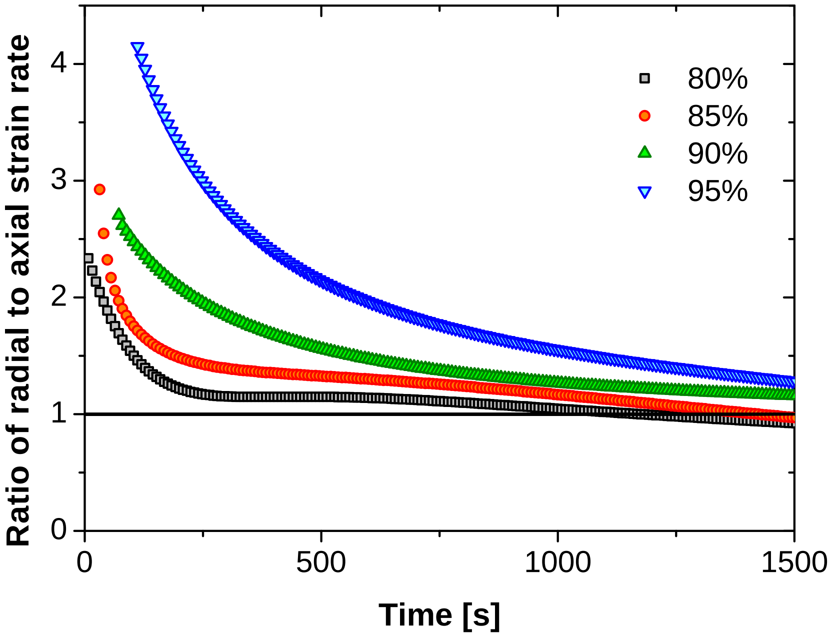

Figure 4.26: Radial to axial strain rate ratio for subsequent free sintering after zero radial shrinkage from 80%, 85%, 90% and 95% of relative density.

Models for the case "asymmetric laminate: viscous substrate / LTCC material" have been already developed by Cai[107;117] and Kanters[102] and have been presented in § 2.3.5.2.

Material parameters

In order to simulate the stress built into the LTCC for the different cases, viscous and elastic input data are needed. The Young's modulus of both types of constraining layers (dense alumina substrate and green alumina tape) has to be known as function of the heating program. For both materials, a constant Poisson's ratio of 0.26 is assumed.[163]

Young's modulus of the green alumina tape increases with temperature and holding time (figure 4.27). At these temperatures, surface diffusion occurs on the alumina particles and consolidates necks between them. From 700 ° C to 840 ° C (in the temperature range where the LTCC material densifies), the Young's modulus increases from 7.6 GPa to 12.7 GPa.

The Young's modulus of the dense alumina substrate at room temperature is given by the manufacturer: 340 GPa. The temperature dependence is expected to be similar to the one measured on the green alumina tape when no diffusion is occurring, i.e. during cooling (not represented in figure 4.27). The Young's modulus varies then from 340 GPa at room temperature to 303 GPa at 840 ° C.

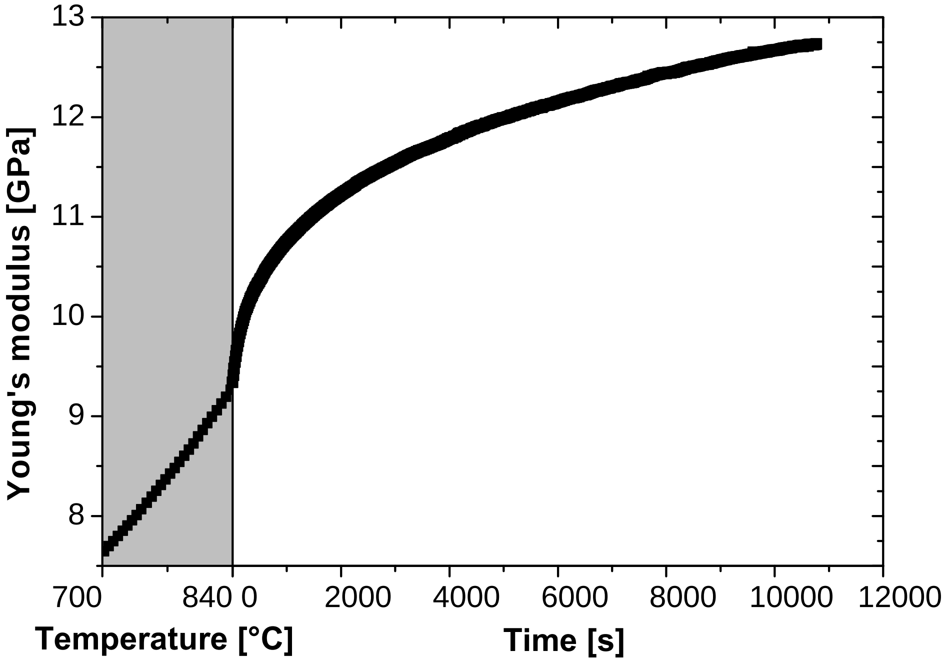

Figure 4.27: Young's modulus of the green alumina tape as function of temperature and as function of time at 840 ° C.

For the LTCC material, sintering parameters at low and high densities have to be known. Uniaxial viscosities obtained by DSF between 76% and 97% of relative density are fitted by an exponential growth function:

$$E^p = A + B \cdot exp(\rho/C) \tag{4.6}$$

with $A = 6.462 \cdot 10^7$, $B = 3.386 \cdot 10^1$ and $C = 5.153 \cdot 10^{-2}$. Uniaxial viscosities at low ($< 76\%$) and high densities ($> 97\%$) are extrapolated. As the laminates start to sinter below 840 ° C, uniaxial viscosity is determined along the heating ramp using the activation energy defined in eq. 4.1. Between 65 and 76% of relative density, values for the viscous Poisson's ratio are arbitrarly taken to be constant ($\nu^p = 0.17$). Between 76 and 97% of relative density, viscous Poisson's ratio is fitted by a polynomial function of the 2^{nd} order. Free strain rate is measured on laminates along the heating schedule. Free strain rate is further fitted by a polynomial function of 9^{th} order.

4.3.1 Sintering of an asymmetric laminate

4.3.1.1 LTCC layer on a viscous substrate

The camber of a bi-layer with an initial thickness ratio m of 10 is shown in figure 4.28. The shrinking LTCC material is on top. As the top layer wants to shrink and the dense LTCC material does not, a tensile stress in the shrinking layer near the interface will arise and lead to the camber of the sample. In figure 4.29, the camber experimentally measured for different starting thickness ratio is plotted as function of time. Camber depends to a great extent on the starting thickness ratio m, which decreases with time as only the thickness of the shrinking layer h_1 decreases (figure 2.16). A larger m leads to larger camber, as the shrinking layer exerts a higher force to bend the substrate. Bi-layers start to camber during the heating ramp. As the initial thickness ratio m decreases, samples start to camber at higher temperatures: at 793 $^\circ$C, 820 $^\circ$C and 840 $^\circ$C for an initial m of 10, 5 and 3, respectively. The camber increases up to a maximum and slightly decreases after 1000 seconds at 840 $^\circ$C. The maximal camber is 22, 8 and 2 m^{-1} for an initial m of 10, 5 and 3, respectively. In figure 4.28 a) the camber is 9 m^{-1} and b) 22 m^{-1}.

Microstructure investigation

SEM micrographs are taken at 3 different positions along the thickness of the shrinking LTCC material for the bi-layer with an initial thickness ratio m of 10 sintered at 840 $^\circ$C for 1 hour (position a, b and c in figure 2.16). As can be seen in figure 4.30, a gradient of porosity develops along the z direction. Porosity is varying from 2.3%, near the interface 1, 0.7% in the middle and to 0.3% near the top of the sample. Average pore area increases as porosity increases: 0.7 μm^2, 1.3 μm^2 and 2.0 μm^2 for regions near the top of the sample, in the middle and near interface 1, respectively. Average pore area is increased by a factor of about 3 near interface 1 compared to the region near the top of the sample.

4.3.1.2 LTCC layer on an elastic substrate

Instead of a viscous layer, the LTCC laminate can be constrained by an elastic material. Viscous properties of the material 1 (figure 2.16) are replaced by the elastic ones: the Young's modulus (E_1) and Poisson's ratio (ν_1). Similarly to Kanters' approach,[102] a new model is derived to take into account the elastic properties of the constraining substrate for the camber simulation of a bi-layer.

For the viscous layer, the stress along the laminate thickness is expressed by:

$$\sigma_{r2}(z) = \frac{E_2^p(z)}{1-\nu_2^p(z)}(\dot{\varepsilon}_0 - z\dot{\kappa}_K - \dot{z}\kappa_K - \dot{\varepsilon}_2^{free}(z)) \tag{4.7}$$

whereas in the elastic layer, the strain in the radial direction is equal to:

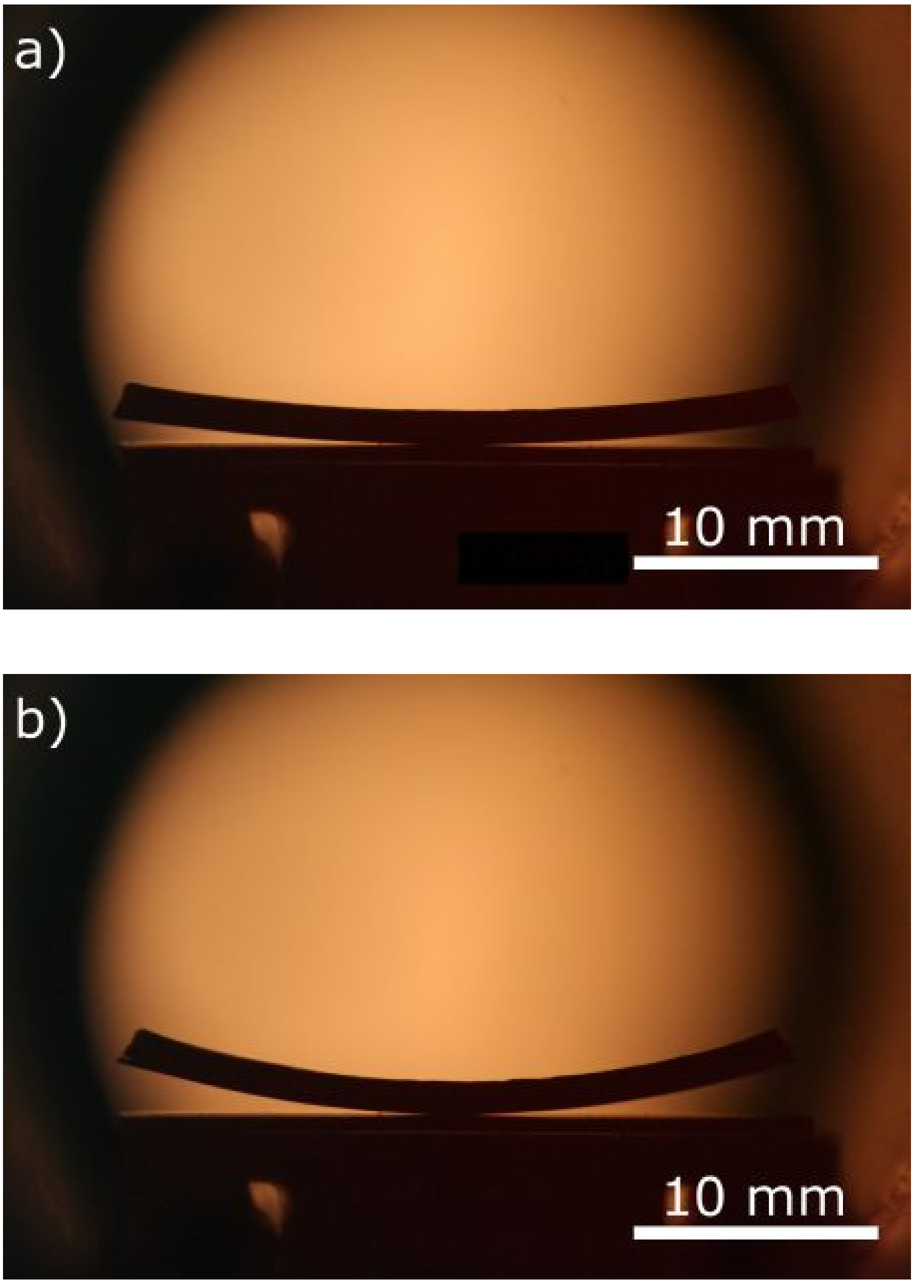

[redacted]

Figure 4.28: Pictures showing the camber development at 840 ° C for a) 0 min and b) 10 min. The initial thickness ratio m is 10.

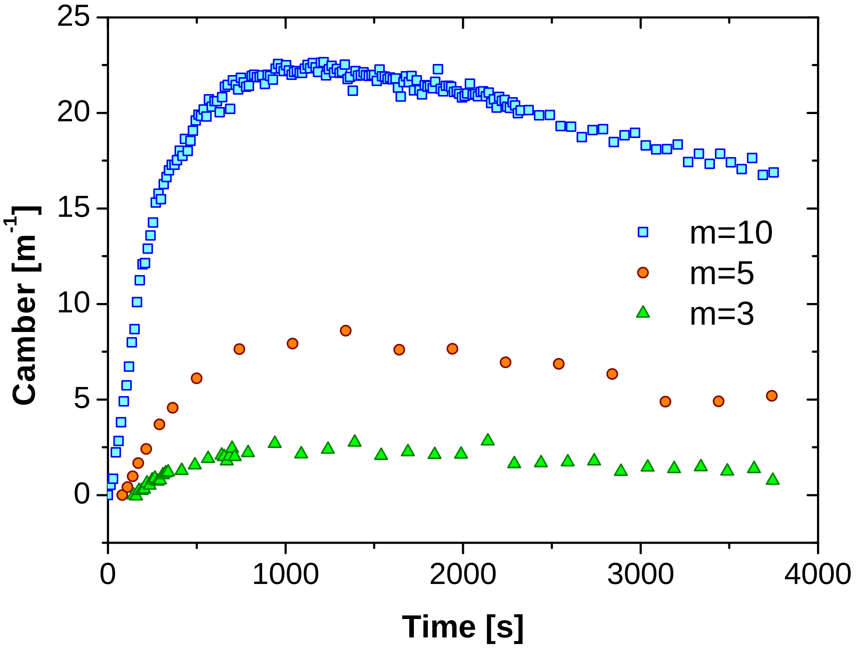

Figure 4.29: Camber experimentally measured for different initial thickness ratios m of 3, 5 and 10, as function of time.

$$\varepsilon_{r1}(z) = \frac{1-\nu_1(z)}{E_1(z)}\sigma_{r1}(z) \tag{4.8}$$

Rearranging eq. 4.8 and eq. 2.26, the stress along the laminate thickness is expressed by:

$$\sigma_{r1}(z) = \frac{E_1(z)}{1-\nu_1(z)}(\varepsilon_0 - z\kappa_K) \tag{4.9}$$

By solving the force and moment equilibrium (eq. 2.30 and eq. 2.31), κ_K and ε_0 are deduced. The integration procedure is the same as in Kanters' model (Appendix B). As mentioned before, to camber the bi-layer, the stiffness of the constraining layer at the sintering temperature should be low enough: either its thickness is small and/or the Young's modulus is small.

Figure 4.31 shows the camber experimentally measured and simulated as function of time for a bi-layer green alumina tape / LTCC material. Both curves differ from each other. The camber experimentally measured continuously increases up to 275 m^{-1} whereas the simulated camber increases abruptly in the early stage of the simulation until 4 m^{-1} and decreases to 0.

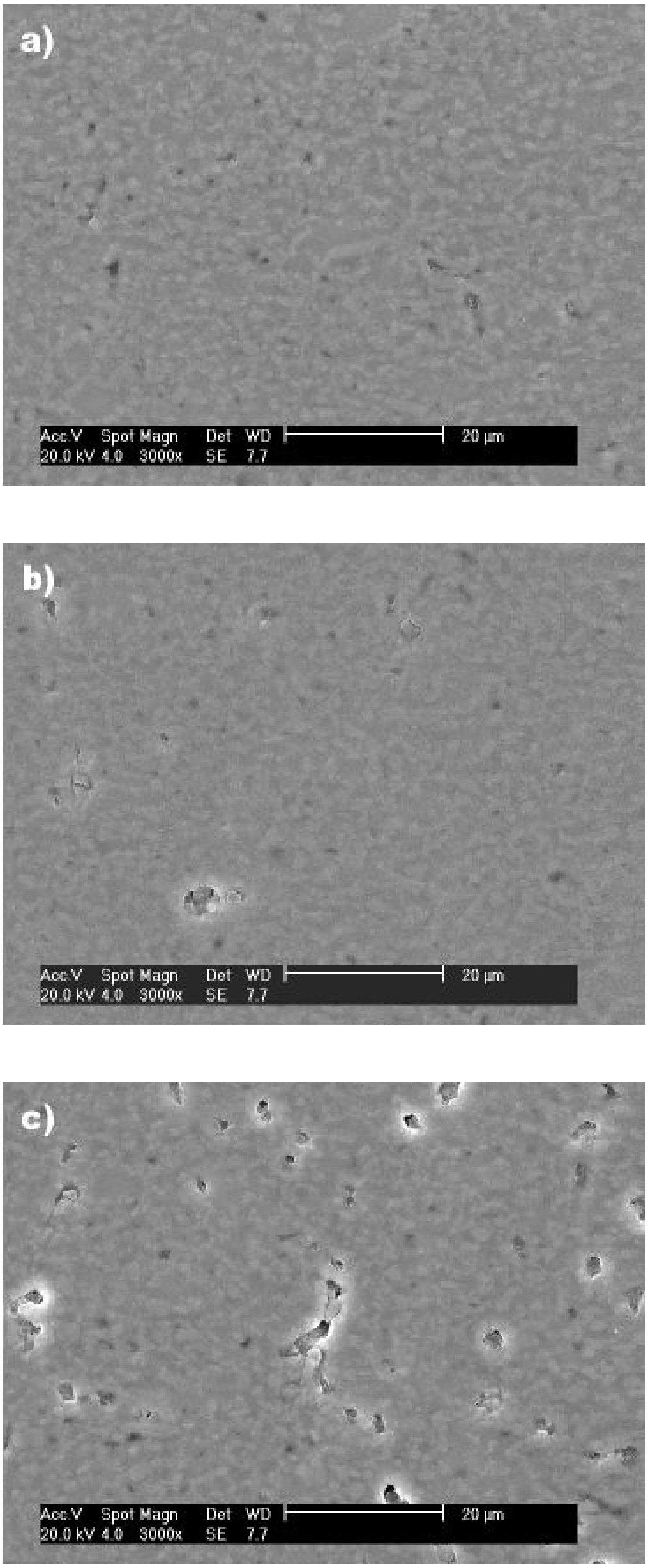

Figure 4.30: SEM micrographs along the thickness of the shrinking LTCC material after 1 hour at 840 ° C: a) at the top, position a, b) in the middle, position b and c) at interface 1, position c (figure 2.16).

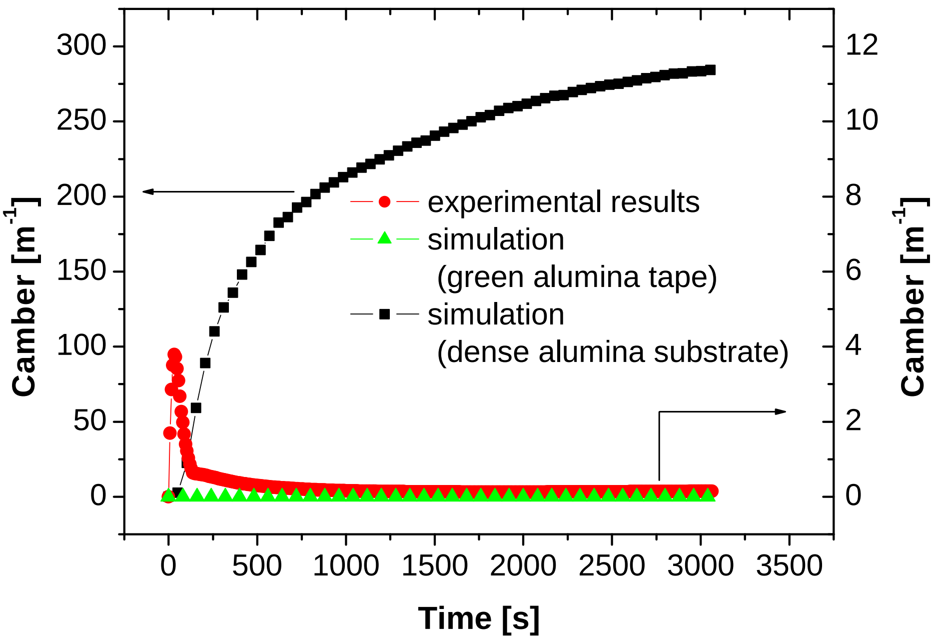

Figure 4.31: Camber experimentally measured and simulated for a LTCC laminate constrained by a green alumina tape with an initial thickness ratio of 3. Simulation for the camber of bi-layer LTCC / dense alumina tape is also plotted.

The simulated camber for the bi-layer, dense alumina substrate / LTCC material is also indicated in figure 4.31. The same dimensions have been used for the simulation as for the experiment with the rocking arm (§ 3.4.3). Experimentally, no camber has been observed. For the simulation, the camber remains extremely low. The highest camber obtained is $2.9 \cdot 10^{-3}$ m^{-1}, which corresponds to a curvature radius of 340 m.

4.3.2 Sintering of a symmetric laminate

4.3.2.1 LTCC layer between elastic substrates

Let's consider the following problem: a viscous layer (material 2) sinters between two elastic substrates (material 1) (figure 4.32). h_1 and h_2 are the thicknesses of the constraining and sintering layers, respectively and are much smaller than in plane dimensions (thin plate). The viscous layer has a uniaxial viscosity E_2^p, a viscous Poisson's ratio ν_2^p and a free sintering rate $\dot{\varepsilon}_2^{free}$, whereas the elastic material is characterized by Young's modulus E_1 and Poisson's ratio ν_1.

In the case where the viscous layer is totally constrained (i.e. Material 1 has a Young's modulus which tends to infinity), $\dot{\varepsilon}_r = 0$ and the built-in stress depends only on the sintering parameters of the shrinking viscous material:

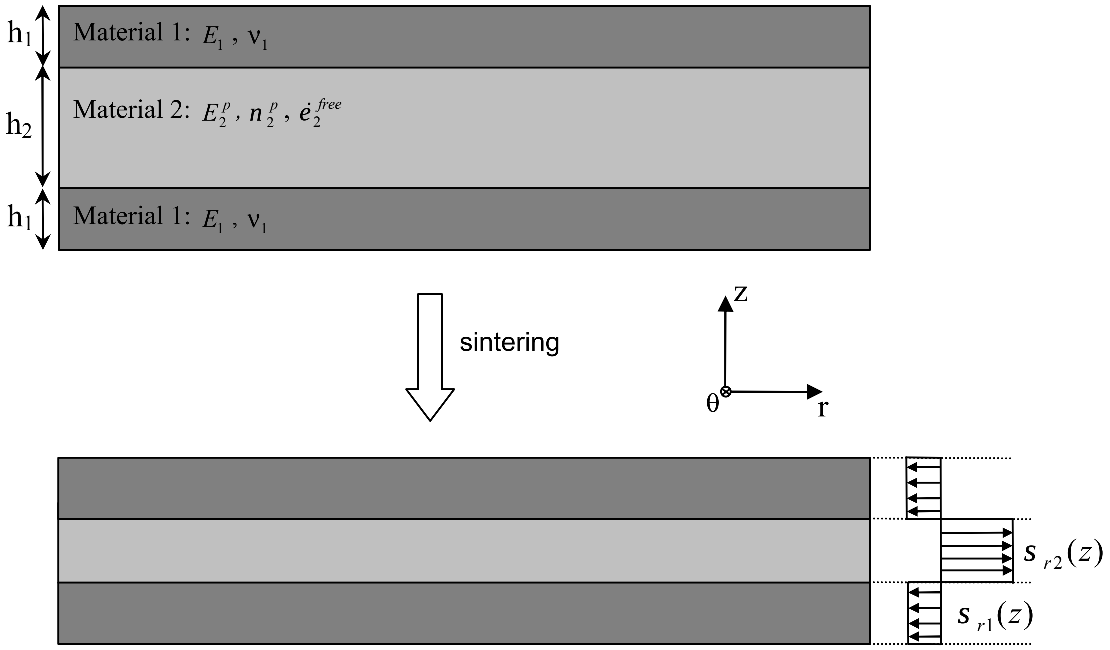

Figure 4.32: Schematic of a symmetric laminate.

$$\sigma_{r2} = \sigma^{\infty} = -\frac{\dot{\varepsilon}_2^{free} E_2^p}{1-\nu_2^p} \tag{4.10}$$

However, if the elastic modulus of the outside layers has a finite value, the stress developed in the viscous laminate will be reduced. This effect is quantified by calculating the elastic response of the substrates:

$$\varepsilon_{r1} = \sigma_{r1}\frac{1-\nu_1}{E_1} \tag{4.11}$$

The force balance equilibrium gives:

$$-2h_1\sigma_{r1} = h_2\sigma_{r2} \tag{4.12}$$

The following boundary condition is assumed:

$$\varepsilon_{r1} = \varepsilon_{r2} \quad \Leftrightarrow \quad \dot{\varepsilon}_{r1} = \dot{\varepsilon}_{r2} \tag{4.13}$$

Rearranging eq. 4.11, eq. 4.12 and eq. 4.13 gives:

$$\frac{d}{dt}\left[-\frac{h_2\sigma_{r2}}{2h_1}\frac{1-\nu_1}{E_1}\right] = \sigma_{r2}\frac{1-\nu_2^p}{E_2^p} + \dot{\varepsilon}_2^{free} \tag{4.14}$$

The viscous constitutive equation in the z direction is given by:

$$\frac{dh_2}{dt} = h_{20}\left[\dot{\varepsilon}_2^{free} - \frac{2\nu_2^p\sigma_{r2}}{E_2^p}\right] \tag{4.15}$$

where h_{20} is the initial thickness of the material 2.

Combining eq. 4.14 and eq. 4.15, a differential equation of the second order is obtained:

$$\begin{aligned} &\sigma_{r2}\left[\frac{\nu_1 - 1}{E_1}\frac{h_{20}\dot{\varepsilon}_2^{free}}{2h_1} + \frac{\nu_2^p - 1}{E_2^p}\right] + \sigma_{r2}^2\left[\frac{2\nu_2^p}{E_2^p}\frac{1-\nu_1}{E_1}\frac{h_{20}}{2h_1}\right] + \\ &\frac{d\sigma_{r2}}{dt}\left[\frac{(1-\nu_1)h_{20}}{2h_1E_1}\int\left(\dot{\varepsilon}_2^{free} - \frac{2\nu_2^p\sigma_{r2}}{E_2^p}\right)dt\right] = \dot{\varepsilon}_2^{free} \end{aligned} \tag{4.16}$$

h_1 is taken constant for the calculation. Eq. 4.16 is numerically solved with a constant $\Delta t = 2s$ and by taking the following boundary conditions: at $t = 0$, $\sigma_{r2} = 0$, $\dot{\varepsilon}_2^{free} = 0$. The integration procedure is the same as in Kanters' model (Appendix B).

Densification behavior of constrained laminates

Densification behavior of the laminates is measured with different techniques:

- for the freely sintered sample, the density is calculated by measuring radial and axial strains in the sinter-forging facility,
- for the laminate constrained with the green alumina tape, the density is determined by the Archimedes method for several samples heated at 840 ° C for different times.
- for the laminate constrained with the dense alumina substrate, the density is calculated by measuring the sample thickness using the rocking arm. The sample is constrained on one side but did not show any noticeable camber.

Large differences can be observed in the densification behavior (figure 4.33). After reaching the isothermal temperature plateau of 840 ° C, the samples are about 71 % dense after 1, 10 and 14 min, for the freely sintered sample, the laminate constrained with the green alumina tape and the laminate constrained with the dense alumina substrate, respectively. If the sample is freely sintered, the theoretical density is reached after about 8000 s, whereas if it is constrained with a dense alumina substrate, only a relative density of about 88% is reached after about 11000 s. On the other hand, when the laminate is constrained with the green alumina tape, a higher relative density is reached ($\sim$ 95%).

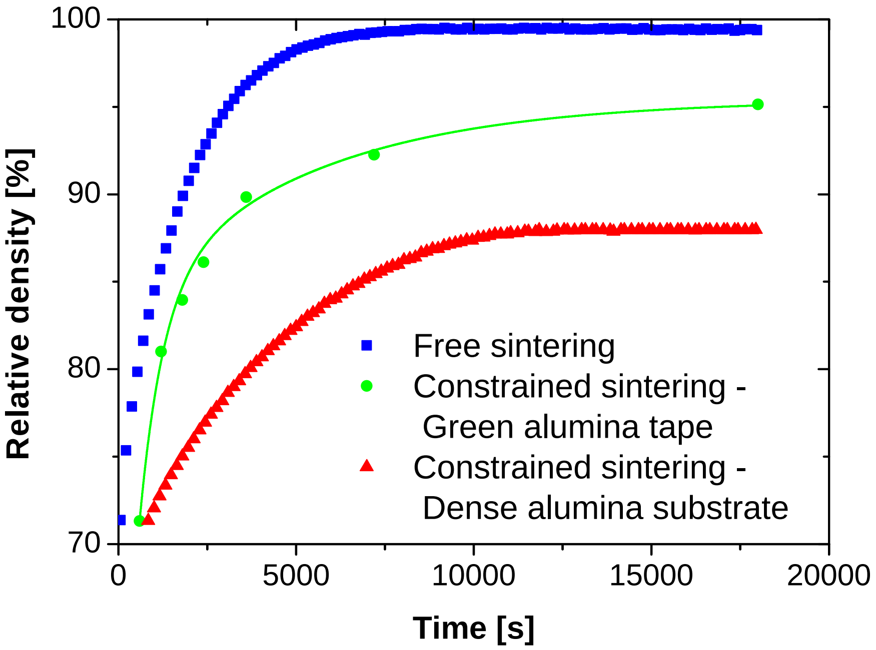

Figure 4.33: Densification behavior for laminates freely sintered, constrained with green alumina tapes and constrained with a dense alumina substrate at 840 ° C.

This would imply that, in this case, the sample is not fully constrained and that a limited degree of constraint exists.

Microstructure characterization

Microstructure investigation is performed on cross sections at the relative density of 86%. As can be seen in figure 4.34, the average pore area changes if the LTCC material is constrained or not, and is affected by the substrate type. It has also been observed that when the laminate is freely sintered, the average pore area remains approximately constant with density and is about the same order as the average particle area ($\sim$ 0.4 μm^2) - figure 4.35. If the sample is constrained by a green alumina tape, the average pore area is increased by a factor of 5 at 86% and 10 at relative densities larger than 92%. If the sample is constrained by a dense alumina substrate, this factor is higher than 25 and the average pore area is about 10 μm^2. Differences in the densification behavior and the microstructure can be directly correlated: the more densification is hindered and the lower the final density is, the larger the pores are.

In figure 4.36, the pore orientation factor is plotted as function of density for samples freely sintered, constrained with a green alumina tape and constrained with a dense alumina substrate. When the laminate is freely sintered or constrained, the pore orientation factor k_p remains the same and is equal to about 2.5. When the laminate is constrained

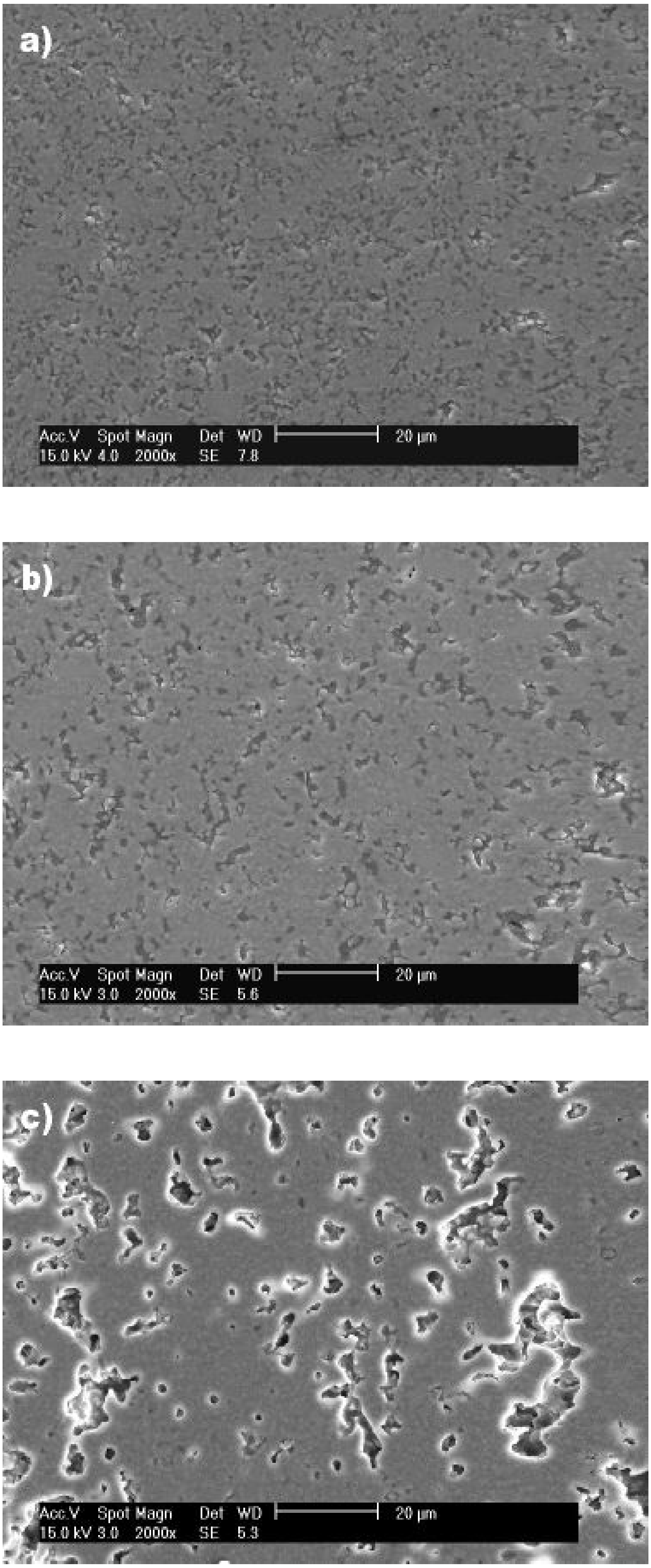

Figure 4.34: SEM micrographs of laminates a) freely sintered, b) constrained with green alumina tapes and c) constrained with a dense alumina substrate at a relative density of about 86%.

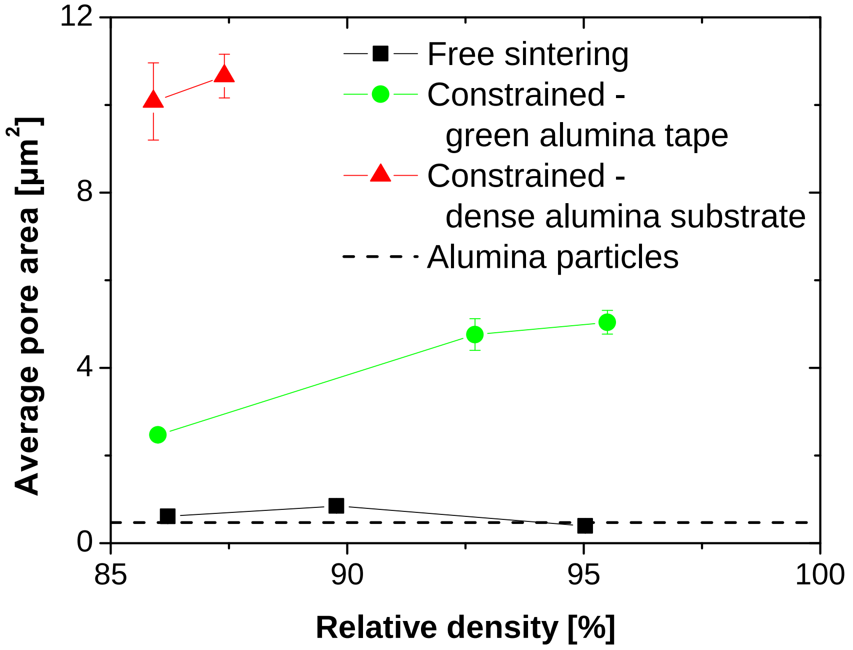

Figure 4.35: Average pore area as function of relative density for laminates freely sintered, constrained with green alumina tapes and constrained with a dense alumina substrate. Average area of alumina particles is indicated by a dash line.

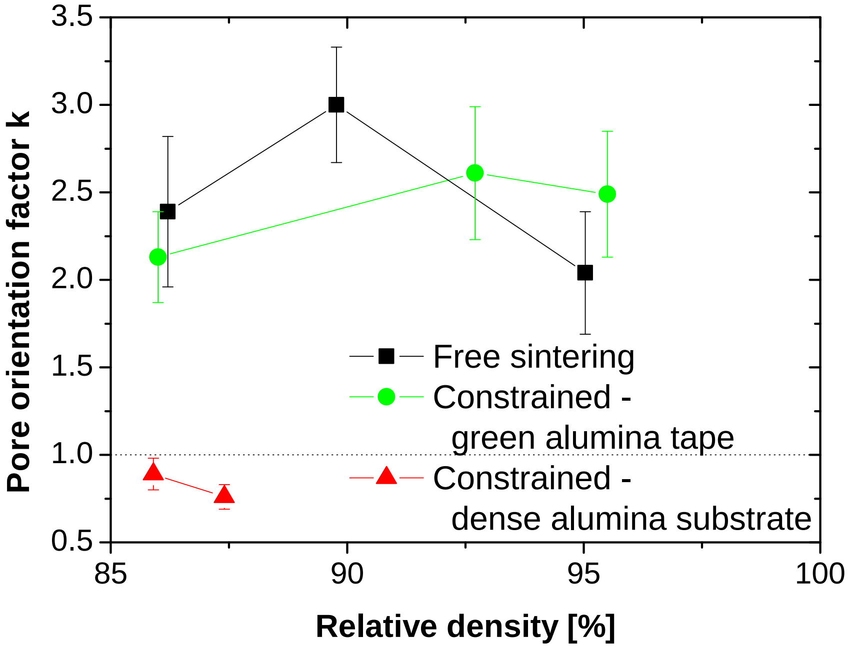

Figure 4.36: Pore orientation factor k_p as function of relative density for laminates freely sintered, constrained with green alumina tapes and constrained with a dense alumina substrate.

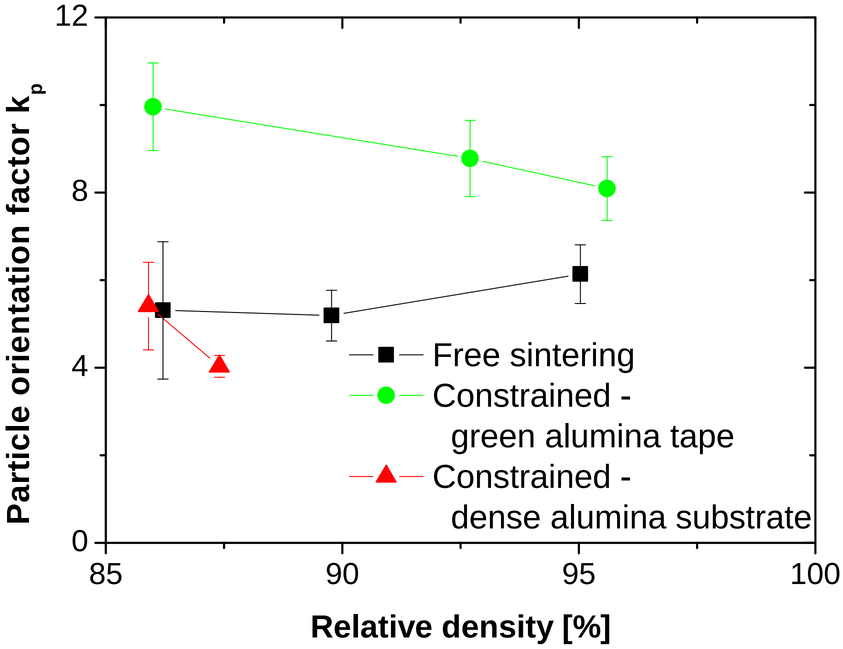

Figure 4.37: Particle orientation factor k_p as function of relative density for laminates freely sintered, constrained with green alumina tapes and constrained with a dense alumina substrate.

by a dense alumina substrate, the pore orientation factor becomes lower than 1, which means that the pores are oriented perpendicularly to the plane of the laminate.

Figure 4.37 displays the particle orientation factor as function of density for the various samples. In every case, particles have an orientation factor k_p larger than 1, lying between 4 and 10. When laminates are freely sintered or constrained by a dense alumina substrate, no difference in the orientation factor is observable. If the laminate is constrained by a green alumina tape, the orientation factor is larger (two times larger at 86% of relative density).

For both constrained laminates, no gradient of porosity, average pore area and pore orientation was observed along the thickness of the laminate. The orientation factor of the particles remained also constant.

Simulation

The built-in stress in the shrinking layer is calculated using eq. 4.16.

Figure 4.38 provides stress built into the LTCC material as function of relative density. A lower Young's modulus leads to a lower stress σ_L. To underline this effect, the normalized stress σ_N is defined as follows:

$$\sigma_N = \frac{\sigma_{r2}}{\sigma^\infty} \tag{4.17}$$

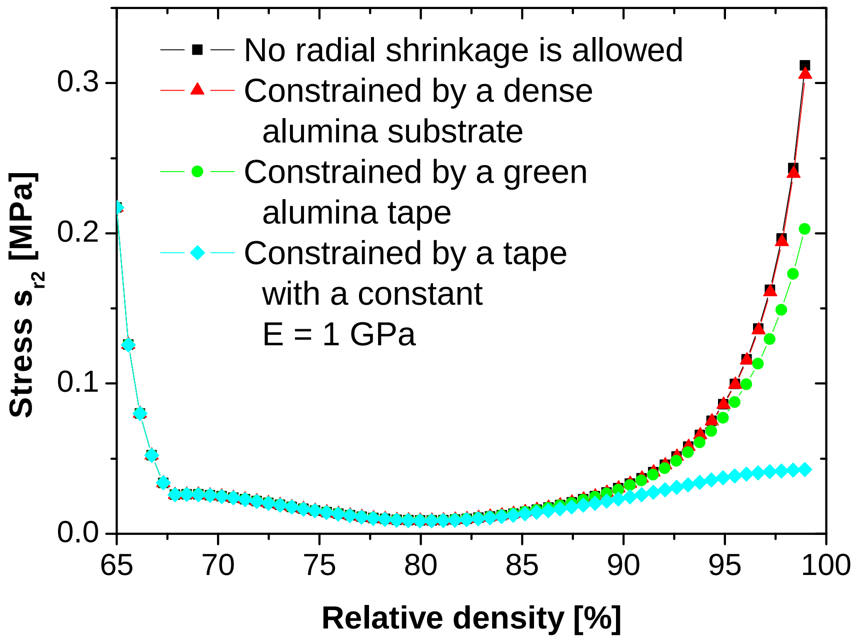

Figure 4.38: Stress built into the LTCC material as function of relative density for a LTCC laminate constrained by (i) a rigid substrate whose Young's modulus is infinite, (ii) a dense alumina substrate, (iii) a green alumina tape and (iv) a substrate whose Young's modulus is equal to 1 GPa.

where σ^{∞} corresponds to the stress calculated when the laminate is perfectly constrained (eq. 4.10) and is represented by the square dots (figure 4.38).

As can be seen in figure 4.39, when the LTCC material is constrained by the dense alumina substrate, the decrease of the built-in stress is very small and represents 3 % of σ^{∞}. When the laminate is constrained by the green alumina tape, the decrease starts from lower relative densities and is larger (about 33%). To give an order of magnitude of how built-in stress is affected by a lower value of Young's, the calculation for a Young's modulus of 1 GPa is represented by the round dots. In any case, relaxation of the stress is not observed at low relative densities (from 65 to 70 %).

4.3.2.2 LTCC layer between viscous substrates

Similarly to the previous model, a viscous model can be developed. The elastic equation 4.11 is replaced by the viscous one:

$$\dot{\varepsilon}_{r1} = \sigma_{r1}\frac{1-\nu_1^p}{E_1^p} + \dot{\varepsilon}_1^{free} \tag{4.18}$$

The radial strain rate in material 2 can be rewritten as:

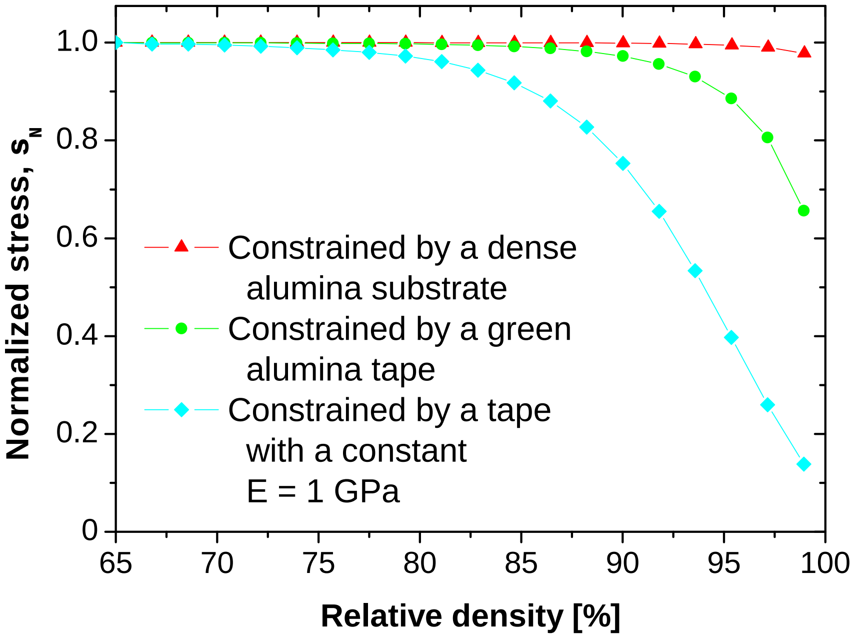

Figure 4.39: Normalized stress as function of relative density for a LTCC laminate constrained by (i) a dense alumina substrate, (ii) a green alumina tape and (iii) a substrate whose Young's modulus is equal to 1 GPa.

$$\dot{\varepsilon}_{r2} = \sigma_{r2}\frac{1-\nu_2^p}{E_2^p} + \dot{\varepsilon}_2^{free} \tag{4.19}$$

Applying the force balance equilibrium (eq. 4.12) and the boundary condition (eq. 4.13), the stress σ_{r2} built into the LTCC is given by:

$$\sigma_{r2} = \frac{\dot{\varepsilon}_1^{free} - \dot{\varepsilon}_2^{free}}{\dfrac{1-\nu_2^p}{E_2^p} + \dfrac{h_2}{2h_1}\dfrac{1-\nu_1^p}{E_1^p}} \tag{4.20}$$

The integration procedure is the same as in Kanters' model (Appendix B). For this model, no experimental data are available. However, the built-in stress, σ_{r2}, is simulated for a LTCC shrinking layer constrained by dense LTCC substrates with an initial thickness ratio h_2/h_1 of 4. Results are plotted in figure 4.40 and 4.41. Trends of the curves are similar to the simulation of a symmetric laminate constrained by elastic substrates: the stress is relaxed only at high densities. The normalized stress decreases up to 0.28.

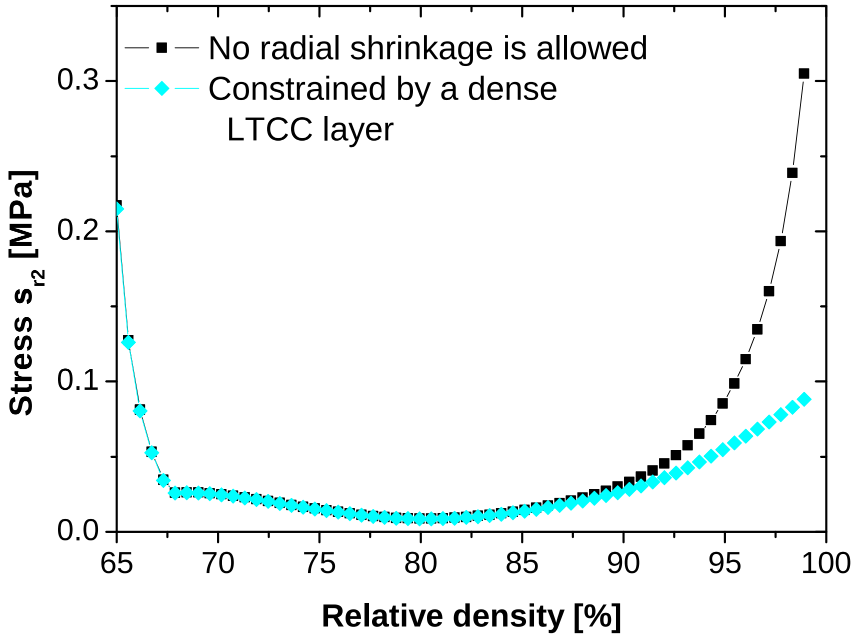

Figure 4.40: Stress built into the LTCC material as function of relative density for a LTCC laminate constrained by (i) a rigid substrate whose uniaxial viscosity is infinite, (ii) a dense LTCC layer.

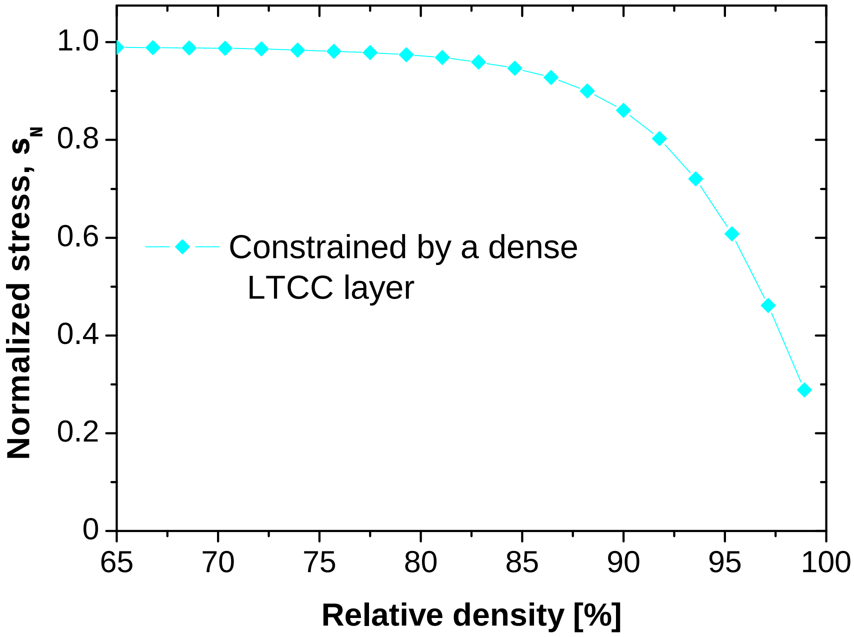

Figure 4.41: Normalized stress as function of relative density for a LTCC laminate constrained by a dense LTCC layer.

Chapter 5

Discussion

5.1 Free sintering

Contrary to uniaxially and subsequently isostatically pressed polycrystalline materials,[74] a slight anisotropic shrinkage behavior of bulk samples is observed (figure 4.1). Anisotropy is believed to be caused by the uniaxial pressing. For steel powder compacts, it was observed by in situ microtomography that pores are oriented perpendicular to the load.[164] It is expected here that pores should be oriented in the same direction, as the sample initially exhibits a higher densification rate in the radial direction: the high radius of curvature enhances densification in this direction.[134]

Concerning laminates, it was found in the literature that for alumina, the in-plane shrinkage remains higher than the axial shrinkage during densification.[63;136] It was attributed to the pore orientation (parallel to the in-plane) and the differences of packing in both directions (a higher density of packing is reached in the axial direction). A higher radial strain rate than axial strain rate is observed here only in the early stage of sintering. This initial anisotropy is even larger than for bulk samples, so that pores are expected to be further oriented.

Beyond a certain range of density, axial strain rate overtakes the radial strain rate for both kinds of samples. This occurs at a relatively low density: at 68% and 74% of relative density for laminates and bulk samples, respectively. However, at 90% of relative density, the pore orientation factor is approximately the same for laminates and bulk samples and is larger than 1 (figure 4.36), which means that pores are still oriented in the perpendicular plane to the axial direction. Therefore, pore orientation determined on 2D micrographs is not sufficient to explain the trend for strain rates. Two other possible reasons could be envisaged: sintering anisotropy may be influenced by (i) gravity[137;138] and (ii) the small alumina disc placed on the top of the sample which exerts a load of 60 Pa (figure 3.2). In the first case, for bulk samples, which are more prone to the gravity effect, no slumping of the sample is observed. Thus, gravity effect should be disregarded. In the second case, the force exerted by the alumina disc is smaller on a laminate than on a bulk sample (the contact area is larger on a laminate than on a bulk sample). Thus, it does not explain why, at higher densities, the anisotropy is magnified for laminates compared to bulk samples. A possible interaction between pores and particles may occur. This will be discussed in more detail for sinter-forged specimens (§ 5.2.1). A three-dimensional access to the microstructure may be needed to further explain the anisotropic sintering behavior. As the resolution obtained by microtomography is too low (a voxel or "volumetric pixel" is typically of the micrometer range)[165], sequential ablation by Focused Ion Beam (FIB) is the only method which could be used to better characterize the microstructure as a better resolution can be reached (1 voxel corresponds to about 2 nm^3).[166]

Although the glass does not wet the alumina particles,[143] theoretical density is obtained (figure 4.2). This observation is contrary to Ewsuk's model where it is stated that it is necessary that the glass wets the ceramic particles.[48] As Kemethmüller *et al.*[51] noticed, this indicates that the predominant mechanism for the densification is viscous flow (3^{rd} stage of Ewsuk's model).

Differences in the densification behavior between bulk samples and laminates (figure 4.2) could arise from two reasons: (i) microstructural differences (packing, pore orientation, particle orientation) and (ii) different initial densities. Guillon *et al.*[167] noticed the influence of green state processing on the densification behavior: the authors showed that if pores are smaller, sintering stress is larger. As can be seen in figure 4.4, median pore size for bulk samples is smaller than for laminates. Hence, the sintering stress is smaller for laminates (eq. 2.15). The median pore size remains about two times larger for laminates compared to bulk samples. Considering eq. 2.6, the time required to complete densification for a glass material is proportional to the pore size. This is in good agreement with the densification curves presented before (figure 4.2): as pore size is two times larger, the required time to complete densification is twice longer.

5.2 Sinter-forging

5.2.1 Uniaxial viscosity

The magnitude of the load and range of density for which the load was applied strongly influenced the measurement of the uniaxial viscosity (figure 4.9 and figure 4.11). In comparison, bulk alumina samples have been investigated by Zuo *et al.*[74] and larger stresses were applied: from 0.1 MPa to 2.5 MPa. The density range for which the load does not influence the sintering parameters was defined to be lower than 5% of relative density. In the current study, the density range for which sintering parameters are not affected by the load is smaller than 1% of relative density. As the LTCC material sinters at a temperature higher than the glass transition ($\sim 720\,^\circ$C), measured sintering viscosities are much lower than sintering viscosities for polycrystalline materials (between 30 and

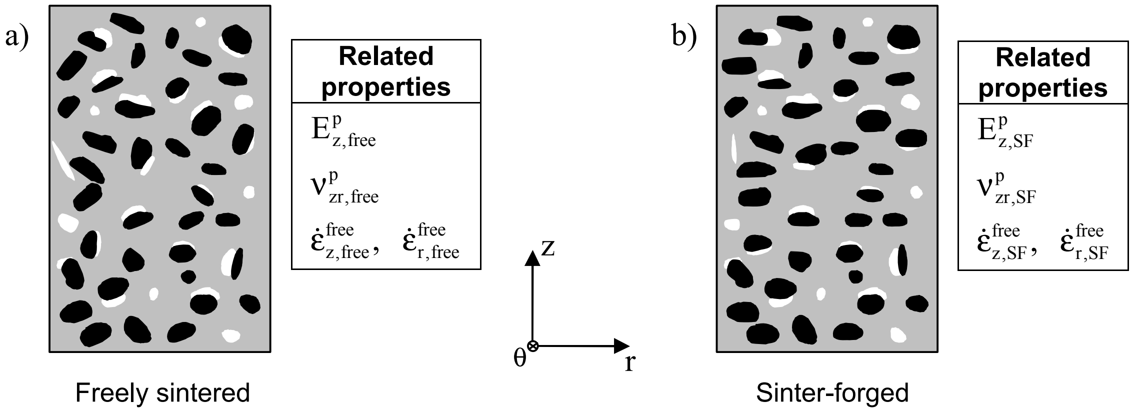

Figure 5.1: Schematic of microstructure for a) freely sintered bulk sample at 90% of relative density and b) sinter-forged bulk sample at 90% of relative density. Pores, alumina particles and glass matrix are represented in white, black and grey, respectively.

2500 GPa.s for alumina bulk samples).[74] Thus, stresses larger than 0.02 MPa (figure 4.11) significantly influence the apparent value of the uniaxial viscosity.

As the load is applied, pores become more oriented perpendicularly to the loading direction (figure 4.19). This observation is contrary to what was observed in the case of crystalline materials,[72] for which pores tend to be oriented parallel to the loading axis (figure 2.18). However, for our present material, it was noticed that pores are almost always in contact with alumina particles (figure 4.17). This is certainly due to the fact that the glass matrix does not wet the alumina particles.[143] Previous work[125;130;168] showed that sintering anisotropy could be affected by inclusions: it was noticed that the pores between matrix and particles will tend to have a preferred orientation and shape if the inclusions are oriented.

Macroscopic uniaxial viscosity and microstructure can be correlated. For alumina materials, although elongated pores along the loading direction cause a higher pore density distribution along the z-axis, uniaxial viscosity decreases as grain growth is hindered during CSF.[74] For sinter-forged and freely sintered LTCC bulk samples, microstructural tendencies can be distinguished at 90% of relative density:

- when the sample is freely sintered, the microstructure is slightly anisotropic: pores and particles are slightly oriented in the radial direction (figure 5.1 a)). The sintering body may be considered to be transversely isotropic (§ 2.3.1) as no differences in properties along the r and θ directions are expected. As strain rates for free sintering and DSF experiments match after release of the load (figure 4.14), the microstructures of freely sintered samples and DSF samples are considered to be identical. Thus, the sintering parameters previously measured are: $E^p_{z,free}$, $\nu^p_{zr,free}$, $\dot{\varepsilon}^{free}_{z,free}$ and $\dot{\varepsilon}^{free}_{r,free}$ (figure 5.1 a)). The subscript "$free$" refers to the case when the bulk sample is freely sintered.

- when an uniaxial load is applied for some density range, particles as well as pores tend to be aligned perpendicularly to the loading direction z (figure 5.1 b)). In this case, sintering parameters are altered. Sintering parameters of a sinter-forged body with high loads are then: $E^p_{z,SF}$, $\nu^p_{zr,SF}$, $\dot{\varepsilon}^{free}_{z,SF}$ and $\dot{\varepsilon}^{free}_{r,SF}$. The subscript "$SF$" refers to the case when the bulk sample is previously sinter-forged. With time, it is expected that the material recovers its pseudo-isotropic structure defined in figure 5.1 a) and thus its sintering parameters.[169]

Due to the mechanical load, orientation of anisometric alumina particles increases their fractional area in the plane perpendicular to the load. The alumina particles may thus act as barriers and hinder viscous flow of the glass, which increases the resistance against deformation in the axial direction. This observation may rationalize the fact that uniaxial viscosities determined by CSF were much higher than uniaxial viscosities determined by DSF. Other studies[56;85;142] showed that the uniaxial viscosity is overestimated with a constant load test because the strain rate in the direction parallel to the loading direction is underestimated: the driving force gradually decreases in the axial direction. The presence of the recovery effect supports this concept.

Mohanram *et al.*[142] found also microstructural differences between freely sintered and constant-loaded LTCC samples. In the case of the constant-loaded specimen, pore clusters are larger and the presence of low density regions is more pronounced. This has not been observed in this work since the pore size remained constant for freely sintered and DSF samples.

To take into account the anisotropy development during sinter-forging, the following formula is proposed :

$$E^p_{z,SF} = E^p_{z,free} + f(\rho_0, \Delta\rho, \sigma) \tag{5.1}$$

where $f(\rho_0, \Delta\rho, \sigma)$ is a function to take the stress history into account. This function should depend on: ρ_0, the initial density where the load was applied; $\Delta\rho$, the range of density where the load was applied and σ, the stress state.

Comparison with models

Uniaxial viscosities of other LTCC materials (GCC) measured by cyclic loading dilatometry have been found to follow the same trends and values were in the same range as those presented here, i.e. between 0.1 and 100 GPa.s (viscosities higher than ∼ 20 GPa.s were attributed to crystallization of the glass).[142;144;145;148;149] Uniaxial viscosities measured at 820 °C and 840 °C can be both fitted by an exponential growth function (eq. 4.6). By normalizing the obtained viscosities by the value extrapolated to 100%, uniaxial viscosities present the same trend and match: differences remain less than 15% over the whole

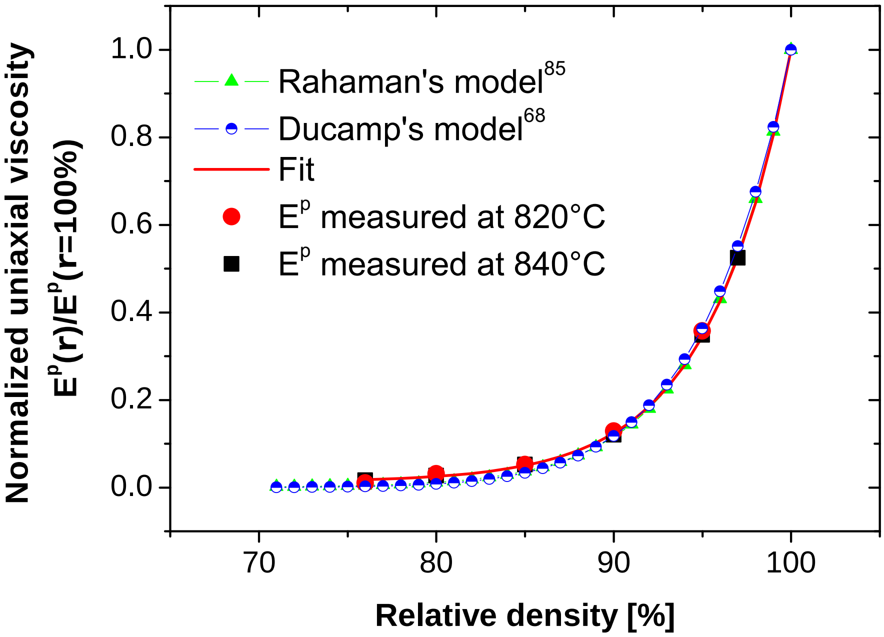

Figure 5.2: Density dependence of uniaxial viscosity normalized by the value obtained at full density for Ducamp's model[68], Rahaman's model[85] and experimental values obtained at 820 and 840 ° C.

density range (figure 5.2). This is expected since the uniaxial viscosity is only thermally activated.

Most of the models predict a quasi linear increase of the uniaxial viscosity with density (figure 2.11). However, two models show good agreement with the measured data: the models by Ducamp[68] and Rahaman.[85] Pore shape is taken into account in both models including it in a fitting parameter. Ducamp's predictions are plotted for an $\alpha = 19$ and Rahaman's predictions for an $a_0 = 11$ (Appendix A). As both fitting parameters are quite high, the load bearing area in the early stage of sintering is believed to be low. This is in good agreement with pore orientation defined for freely sintered sample. As densification proceeds, models predict an exponential increase of the load bearing area. Ducamp's model[68] is derived empirically from viscosities measured on glass. This indicates that the alumina particles do not affect the trend of the curve. This concept is supported by the experimental work from Salamone *et al.*[76] since the addition of ceramic particles did not change the uniaxial viscosity trend but just shifted it to higher values.

5.2.2 Viscous Poisson's ratio

For the density range above 80%, experimentally measured values for the viscous Poisson's ratio (figure 4.16) agree with available models and other experimental results which predict a continuous increase of ν^p as function of density (figure 2.12).[31;32;57;71;73;76;92;94;147;170] Below 80% of relative density, the viscous Poisson's ratio decreases with increasing density, which has been reported only for Rahaman's model.[85] However, the initial anisotropy should be taken into account. As the pores are believed to become more oriented perpendicular to the load (pores will orientate along the alumina particles), the mechanical coupling between the axial and the radial direction may be larger than in the isotropic case and hence the viscous Poisson's ratio should be larger. As densification proceeds, the viscous Poisson's ratio increases as density increases. At high densities, values are slightly larger than 0.5, which is not consistent with the isotropic constitutive equations of the continuum mechanical description of sintering. Nevertheless, Poisson's ratio for anisotropic elastic materials can have no bounds.[171] Numerical sintering simulations could also predict viscous Poisson's ratio higher than 0.5.[65] These higher values may be attributed to the fact that the material is still not isotropic.

As anisotropy is induced (during CSF), the apparent viscous Poisson's ratio ($\nu^p_{zr,SF}$) increases and remains lower than 1. The increase of the viscous Poisson's ratio is supported by the simulations from Wonisch *et al.*[65] and experimental work of Chang *et al.*.[172] However, for alumina[71] as soon as anisotropy was induced, viscous Poisson's ratio decreased abruptly to negative values. A characteristic of the formed anisotropy is that radial shrinkage was promoted.

Viscous Poisson's ratio of a LTCC material has been measured by Mohanram *et al.*[147] Values of viscous Poisson's ratio were found to be in good agreement with the models of Venkatachari[73] and Scherer.[31] However, as wee will see later (§ 5.3.2.1), the method they used to calculate the viscous Poisson's ratio cannot lead to satisfactory results for our material.

5.2.3 Hydrostatic sintering stress

The hydrostatic sintering stress, obtained from eq. 2.14, is plotted as function of density (figure 5.3). For both isothermal temperatures, the hydrostatic sintering stress presents similar trends and values. In the early stage of densification, the absolute value of the hydrostatic sintering stress, Σ, was found to decrease slightly with density and then to increase strongly as the density approaches 95%. Note that for DSF at 840 °C at 95% of relative density, the error bar is very large. This is due to the fact that as viscous Poisson's ratio approaches 0.5 and the free strain rate is still not negligible, the hydrostatic sintering stress will tend to infinity (eq. 2.14). The trend of the hydrostatic sintering stress is comparable with that observed on alumina for which the sintering stress was obtained for a range of temperatures until a density of 98%.[167] For this case, it showed little change until a density of about 88%, then increased in absolute value up to a density of 97% and then decreased again. It is also expected for our material that the hydrostatic sintering stress will decrease at high densities, as densification rate decreases. Theoretical models

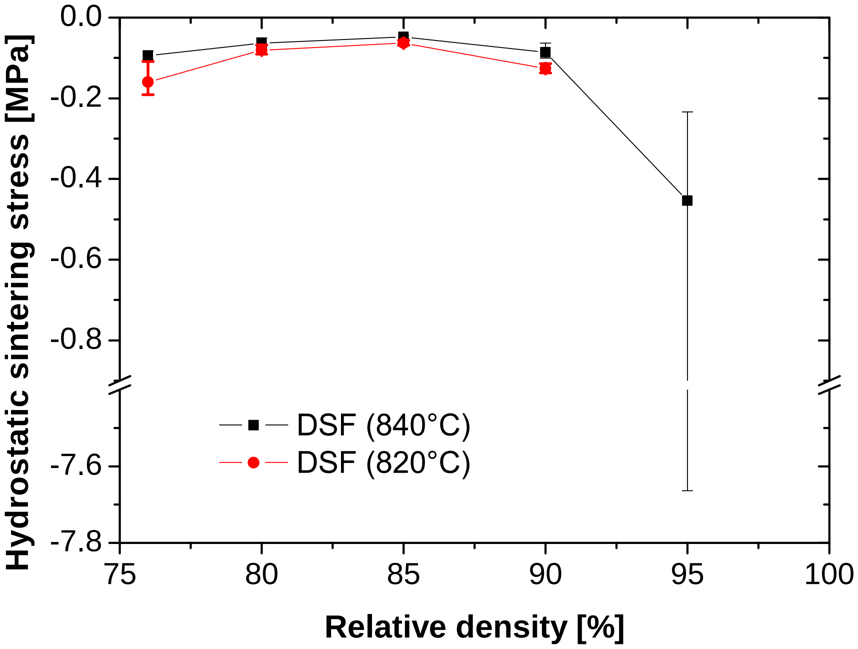

Figure 5.3: Hydrostatic sintering stress Σ as function of relative density from discontinuous sinter-forging experiments - isothermal temperature profile at 820 ° C and 840 ° C.

and numerical simulations predict an increase of the absolute value of the hydrostatic sintering stress with density.[81] For glass materials, eq. 2.14 can be limited only to its curvature term and becomes:[62]

$$\Sigma = \frac{\gamma_s}{r} \tag{5.2}$$

Σ depends to a great extent on the radius of the pores for a glass material. Measurement of pore size distribution showed that the mean pore radius (figure 4.4) did not change significantly for a range of density between 75% and 90% of relative density for bulk samples. At higher densities, the average pore radius may be reduced and the absolute value of the sintering stress increases. At a still later stage, the density of pores is expected to be reduced and the absolute value of the sintering stress to be decreased again.[167] Finally, a smaller sintering stress for glass than for polycrystalline ceramics is obtained (≈13 MPa for dry-pressed alumina at 85% of relative density[71]). However, the surface energy of glass and alumina are about the same order of magnitude. The mean pore size of a sample 85% of relative density of alumina is 0.04 μm,[72] which is five times smaller than the mean pore size for our LTCC material (0.23 μm). This difference in pore size distribution may not completely explain the differences observed between the two materials. The capillary pressure of the grains is needed to be taken into account for polycrystalline materials (eq. 2.15).

Note that at 95% of relative density at 820 ° C and at 97% of relative density at 840 ° C, the measured viscous Poisson's ratio is larger than 0.5. Thus, the calculated hydrostatic sintering stresses are positive. This is not correct as the driving force for sintering is still negative at these densities: the material further densifies. This shows one of the limits of the isotropic modeling. The hydrostatic sintering stress in the transversely isotropic case is much more complex:

$$\Sigma = \frac{1}{3}\left[\frac{-2\dot{\varepsilon}_r^{free} - \dot{\varepsilon}_z^{free}}{\frac{1}{E_r^p}\left(1-\nu_{r\theta}^p - \frac{E_r^p}{E_z^p}\nu_{zr}^p\right) + \frac{1}{E_z^p}\left(1 - 2\frac{E_z^p}{E_r^p}\nu_{rz}^p\right)}\right] \tag{5.3}$$

As can be noticed in eq. 5.3, not only ν_{zr}^p is needed but also a second viscous Poisson's ratio $\nu_{r\theta}^p$. Thus, it is expected that the hydrostatic sintering stress remains negative up to the theoretical density.

5.2.4 Zero radial shrinkage sintering

Between 75% and 80%, measured and predicted stresses needed to produce zero radial shrinkage are in good agreement (figure 4.25). This could be explained by the fact that at these relative densities, uniaxial viscosities determined by CSF and DSF are close to each other (figure 4.9). At higher densities, large discrepancies are believed to be related to the development of anisotropy. As a comparison, for alumina, isotropic modeling leads to values of stresses needed to produce zero radial shrinkage also about three times smaller than the measured one.[64] Eq. 4.5 becomes in the transversely isotropic case:

$$\sigma_z = \frac{E_z^p \dot{\varepsilon}_r^{free}}{\nu_{zr}^p} \tag{5.4}$$

According to eq. 5.4, either E_z^p and/or $\dot{\varepsilon}_r^{free}$ may be underestimated and/or ν_{zr}^p overestimated. It has been shown that under a uniaxial load, the uniaxial viscosity increases significantly, the free strain rate in the radial direction is enhanced, and the viscous Poisson's ratio increases. Thus, all conditions are fulfilled.

Values for the required stress to maintain a zero radial shrinkage vary between 0 and 1.6 MPa. They are larger than the hydrostatic sintering stress calculated from the isotropic modeling in the density range from 76% to 90%. At high densities, two considerations can be taken into account: (i) the uniaxial viscosity is so high such that huge stresses are required to affect the radial shrinkage and (ii) as it is believed that the sintering stress decreases, smaller stresses are needed to keep zero radial strains. As the stress needed to produce zero radial shrinkage decreases after 91% of relative density (figure 4.25), the second consideration is believed to be accurate.

After removal of the load, the sample sinters faster in the radial direction as compared to the axial direction (figure 4.26). Van der Vorst[38] found a possible explanation for expansion during viscous sintering: if pores have a large concave boundary part, pores will first expand to reduce the pore boundary length. This could be envisaged since pores oriented in the $r\theta$ plane have a larger boundary part in this plane. However, more experimental work needs to be done to further confirm it. As expected, the longer the load is maintained, the higher the anisotropy in the free strain rates. Higher ratios of the anisotropy of the free strain rates are obtained for LTCC materials than for alumina: the initial radial to axial strain rate ratio varies between 1.1 to 1.65 for alumina,[64] whereas, it varies between 2.4 to 4.5 in this study. This is in good agreement with the previous results since the ratio load / uniaxial viscosity is higher for the LTCC material than for alumina. Moreover, the longer the load is applied (i.e. for a larger increase of density), the longer the time to recover an almost isotropic state is needed.

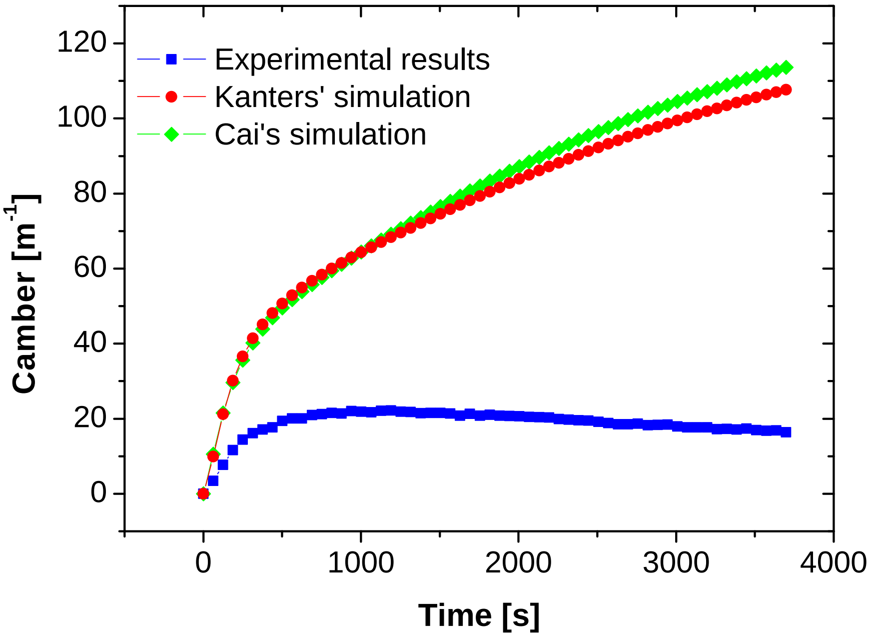

Figure 5.4: Camber experimentally measured and simulated by Cai's and Kanters' model.

5.3 Sintering behavior of laminates

5.3.1 Sintering of an asymmetric laminate

5.3.1.1 LTCC layer on a viscous substrate

Two models are used to predict the camber of a bi-layer: the models by Cai[107;117] and Kanters[102] (figure 5.4). Although both models are based on the same kinematical approach (eq. 2.26), differences can be noticed. Cai *et al.*[107;117] applied directly the viscous analogy on the derived elastic solution for the camber.[122;123] Thus, the term $\dot{z}\kappa_G$ which should have appeared in eq. 2.27, is unintentionally omitted. Moreover, retardation in densification caused by the built-in stress in the shrinking layer is not taken into account (see appendix B). As the stress hinders densification, the sintering parameters (E^p, ν^p and $\dot{\varepsilon}^{free}$) are consequently modified.

Two additional simplifications in Cai's model were made by many researchers using this approach:

- the thickness ratio m is taken as a constant
- viscous Poisson's ratio effect is neglected in the calculation, i.e. the term n depends only on the uniaxial viscosities

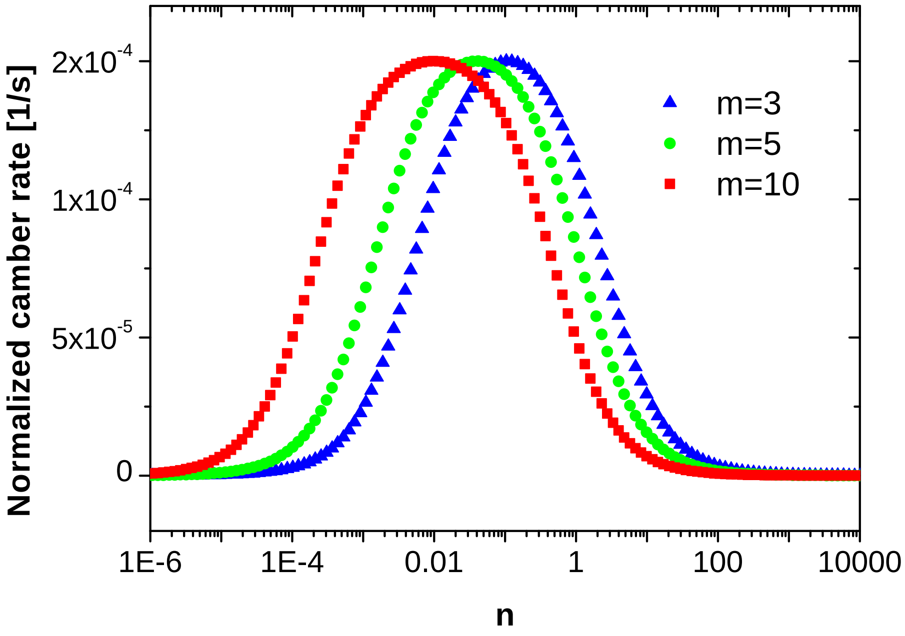

Figure 5.5: Normalized camber rate as function of n for different thickness ratios m of 3, 5 and 10.

In fact, the thickness ratio varies during sintering of the bi-layer and can significantly modify the calculated solution. This can be seen in figure 5.5 where the normalized camber rate is plotted as function of n for different thickness ratios m. For a constant $n = 1$, the normalized camber rate decreases from $1.1{\cdot}10^{-4}$ to $5.0{\cdot}10^{-5}$ for $m = 3$ and 10, respectively. The camber rate is thus more as two times larger. The viscous Poisson's ratio can also largely influence the term n. If a layer is already fully sintered and another has a relatively low density, the viscous Poisson's ratio of the dense layer will be close to 0.5, whereas the shrinking layer will have a lower viscous Poisson's ratio. In the case where the viscous Poisson's ratio of the densifying layer is 0.1, the term n can be multiplied by a factor 5. Depending on the uniaxial viscosity ratio, the camber rate could have a strong influence (figure 5.5).

To sum up, Kanters' model[102] is more rigorous but Cai's model[107;117] is much easier to compute as no temporal integration and spatial discretization is needed to compute the camber.

For the calculations presented in figure 5.4, both models present similar values as the built-in stresses do not influence densification to a large extent. Comparing predictions to the experimental data, it can be seen that both models overestimate the camber. In the following part of this paragraph, experimental values are only compared to Kanters' model.[102] For the sake of comparison, the normalized camber rate will be plotted:

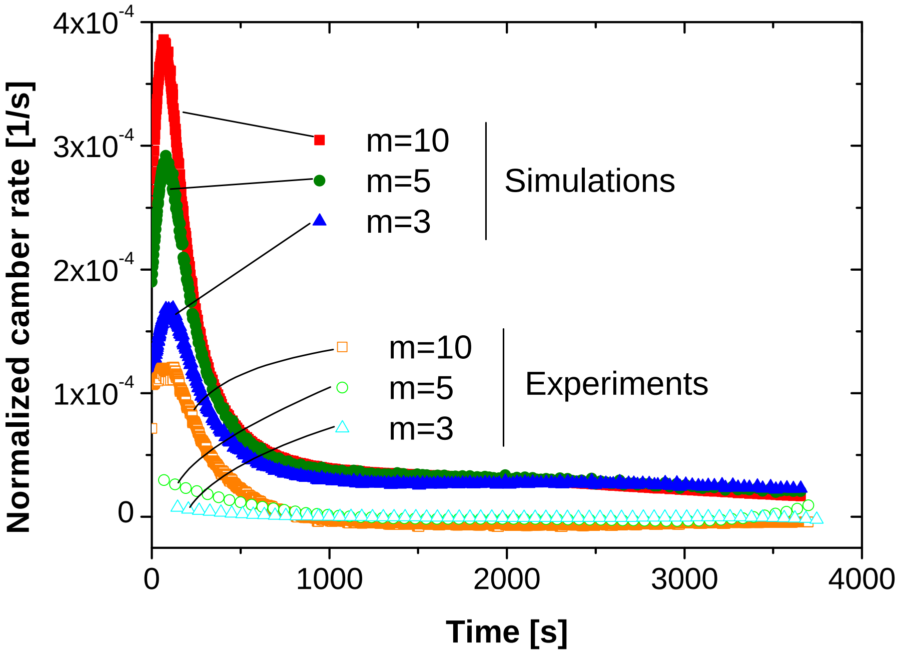

Figure 5.6: Normalized camber rate experimentally measured and simulated as function of time for different initial thickness ratios m of 3, 5 and 10.

$$\dot{\kappa}_{k,n} = \frac{\partial\left(\dfrac{h_1 + h_2}{R}\right)}{\partial t} = \frac{\partial\left[(h_1 + h_2)\kappa_k\right]}{\partial t} \tag{5.5}$$

where $\dot{\kappa}_{k,n}$ is the normalized camber rate and t is the time. Thus, the effect of the overall thickness is not taken into account in the calculation of the camber rate

Predictions and experimental normalized camber are plotted for different starting thickness ratios as function of time in figure 5.6. Predictions lead to larger camber rate values than experimentally measured. The model reproduces qualitatively but not quantitatively the experiments. Discrepancies between predictions and experiments could be due to: (i) the development of anisotropy which is not taken into account in this isotropic model, (ii) heating rate effect and (iii) gravity which impedes the camber.

Anisotropy

The sintering parameters become anisotropic and differ from the ones measured previously on bulk specimens. To understand the effect of the sintering parameters on the camber rate, figure 5.5 is considered. Different cases could explain why predicted values overestimate the warpage: (i) the shrinking layer becomes too viscous and thus impedes the camber (n decreases); (ii) the shrinking layer becomes less viscous so that the in plane stresses can be easily relaxed and thus cambers less (n increases); (iii) the free strain rate decreases and (iv) the viscous Poisson's ratio in the plane of the shrinking layer increases (n decreases). We have previously seen that the viscosity of this LTCC material is very sensitive to external stresses: when a load is applied, the microstructure is altered and the sintering parameters are highly modified.

As can be seen in figure 4.34, when the LTCC layer is constrained with the dense alumina, pores tend to orientate perpendicular to the plane. In this case, the apparent uniaxial viscosity as well as the free strain rate in the plane $r\theta$ decreases. Thus, conditions (ii) and (iii) are fulfilled. Concerning the fourth case, evolution of the viscous Poisson's ratio will be later discussed (§ 5.3.2.2).

Moreover, as the initial thickness ratio m is smaller, the difference between simulation and experiments in camber rate is larger: a ratio of 20, 10, and 4 between simulation and experiments were found for m of 3, 5 and 10, respectively. A possible explanation is that the sample is less constrained when the camber is larger. Thus, a lower degree of anisotropy will be induced and as a result, the isotropic modeling agrees better with the experimental curve. This explanation will be further validated by calculating the stress state for the different experiments.

Heating rate effect

Kanters noticed a dependence of the camber on the heating rate: simulations failed to predict the experimental camber for high heating rates.[102] The reason proposed was that a high heating rate leads to a large error in temperature measurement. The heating rate was decreased here from 20 °C/min to 5 °C/min for the experiment with an initial thickness ratio m of 5. However, this did not have any influence on the overall camber.

Gravity effect

The gravity effect on camber can also be investigated. As soon as the bi-layer starts to camber, i.e. the ends lift up, gravity will exert a moment which tends to camber in the opposite direction. The moment, $M_{gravity}$, due to gravity at the ends of the bi-layer can be expressed by:[173]

$$M_{gravity} = \int_0^{L/2} g \cdot \rho \cdot b \cdot h \cdot x \cdot dx \tag{5.6}$$

where $g = 9.8\ m.s^{-2}$ is the gravity, ρ the density, L, b and h are the length, width and thickness of the bi-layer, respectively.

The moment due to camber M_r can be expressed by:[173]

$$M_r = I\dot{\kappa}E^p \tag{5.7}$$

where $I = bh^3/12$ is the moment of inertia of the cross-section of the bi-layer.

To compare both moments, the ratio, ϖ, has been introduced:

$$\varpi = \frac{M_r}{M_{gravity}} \tag{5.8}$$

The following assumption for the calculation of M_r is made: in the worst case (the moment M_r is the smallest), the uniaxial viscosity of the entire bi-layer is assimilated to the uniaxial viscosity of the shrinking layer. In fact, the constraining substrate will increase the moment M_r as the substrate is stiffer than the shrinking layer. Initial values of ϖ are 10, 17 and 50 for the experiments with $m = 3$, 5 and 10, respectively. At the beginning of sintering, the gravity does not influence in large proportions the camber. As densification proceeds, ϖ decreases: camber rate decreases faster than the uniaxial viscosity increases, whereas $M_{gravity}$ remains identical as the constraining substrate does no shrink ($M_{gravity} \approx 1 \cdot 10^{-5}$ N.m^{-1}). Thus, it explains why for longer sintering times the experimental camber rate is slightly negative. Furthermore, the heaviest sample (for an initial thickness ratio $m = 10$) shows the highest negative normalized camber rate (figure 5.6).

Stress state

Kanters' simulation[102] allows calculating the built-in stresses at different position along the thickness of the shrinking LTCC material (eq. 2.29). Stresses are plotted at different positions as function of density in figure 5.7. As in figure 2.16, the calculated stress state is asymmetric. It is found that the material near the free side of the sample is in a compressive state: densification will then be enhanced. It explains why a minor porosity has been observed at this location (figure 4.30 a)), whereas, near the interface 1 a tensile stress slightly lower than the stress built into the LTCC layer, when no radial shrinkage is allowed (σ^∞), is calculated. This tensile stress hinders the densification and thus a higher porosity is noticed (figure 4.30 c)). Pores with an average pore area of 2 μm^2 are found in the vicinity of the substrate which is about 4 times larger than the average pore area of freely sintered laminates.

Similar microstructural observations have been made in the literature: larger pores in constrained glass films have already been observed and the pore size decreases as pores are located far from the constraining substrate.[116;174] However, pore size does not increase to such a large extent: pores in the vicinity of the constraining substrate remain 1.6[116] and 2-3[174] times larger than for freely sintered samples. Moreover, like in this study, pores did

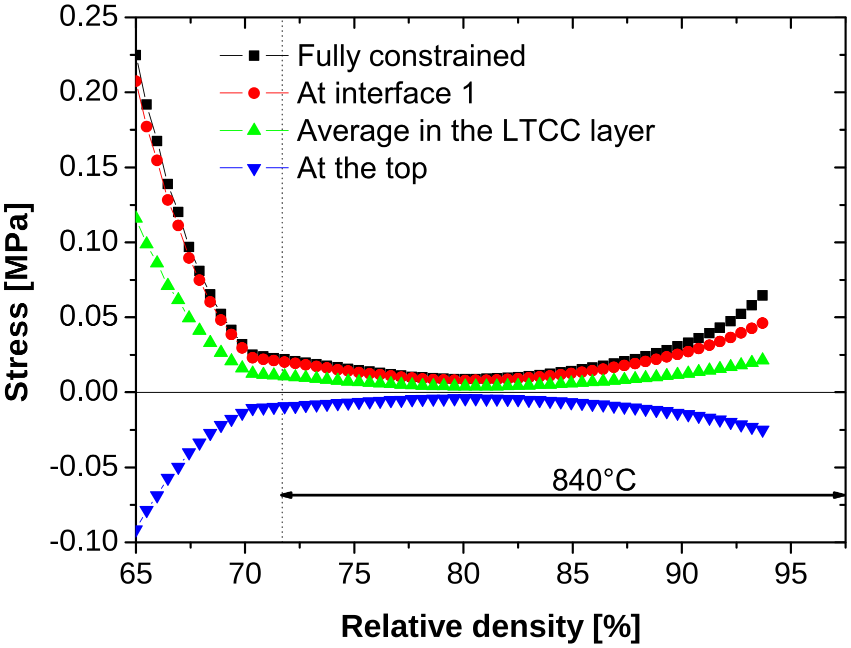

Figure 5.7: Stresses at different z positions: at interface 1 and at the top. The average stress in the LTCC layer as well as the stress built into the LTCC layer when no radial shrinkage is allowed are also plotted.

not show any preferred orientation. Pore growth was attributed to the combined effect of constraint and poor wetting of the substrate by the glass. As we will see in §5.3.2, this explanation is disregarded since in symmetric laminates, large pores are also found far from the constraining substrates.

The average stresses built into the shrinking LTCC layer are plotted as function of relative density for the different initial thickness ratios (figure 5.8). For each experiment, the average stress state is lower than σ^{∞}. At 65% of relative density, the average stress is lower by a factor 3.9, 2.3 and 1.5 for $m = 10$, 5 and 3, respectively. This factor further increases to values of about 5 for all three experiments at 92% of relative density. These calculations match with the fact that a lower degree of anisotropy is induced when the camber is larger.

In the dense LTCC substrate, tensile stresses as high as 4.18 MPa and compressive stresses as low as - 4.84 MPa are predicted (for the experiment with an initial thickness ratio of $m = 10$). High stresses are reached at the beginning of the simulation. They further decrease as densification proceeds. Stresses are higher in the substrate than in the shrinking LTCC layer due to the higher uniaxial viscosity of the substrate. For lower initial thickness ratio, the stresses built into the dense LTCC substrate increase in the substrate so that eq. 2.30 is verified.

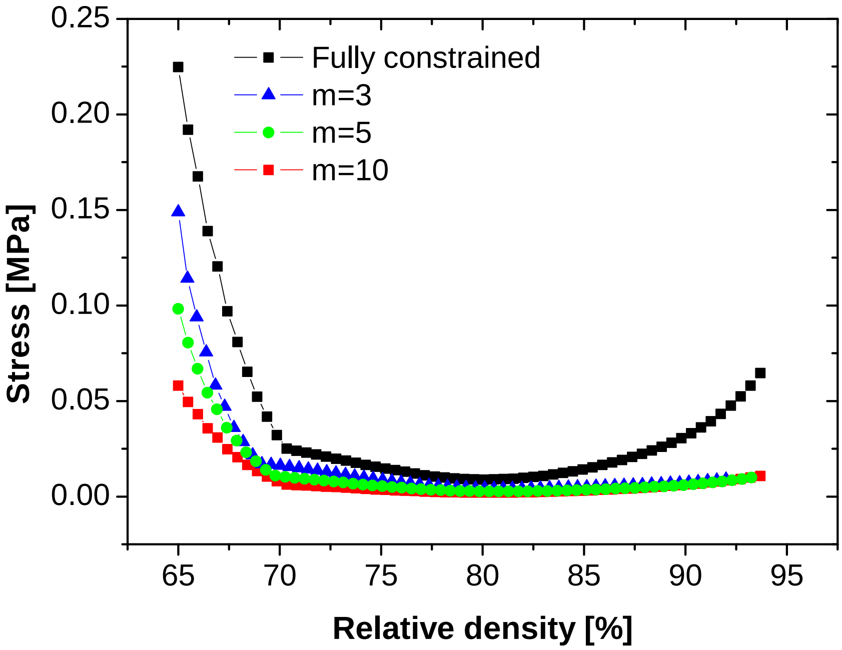

Figure 5.8: Average stresses built into in the shrinking LTCC layer as function of relative density for initial thickness ratios m of 3, 5 and 10. The stress built into the LTCC layer when no radial shrinkage is allowed is indicated.

For the camber prediction of other bi-layer systems, Cai's model[107;117] and the Stoney formula were successfully applied.[120;145;175] The following reasons can be envisaged to explain why the above models succeeded to give accurate predictions: (i) magnitude of the built-in stresses is much lower than the sintering stress, (ii) the material does not exhibit such an anisotropic behavior under constraint.

In the first case, stresses cannot induce anisotropy so that the sintering parameters of the constraining layer do not deviate from the one experimentally measured using an isotropic modeling. In the second case, sintering parameters does not change abruptly under constraint. Alumina fulfills both conditions: it has been shown that anisotropy was induced after an increase of 5% of relative density and uniaxial viscosities remained sensibly similar at low densities whatever the applied load.[74] Thus, the camber of a bi-layer composed of two alumina layers with a different starting green density has been correctly predicted.[175] Chang *et al.*[145] successfully predicted the camber of a bi-layer with two different LTCC materials. As the temperature range of densification is for both materials similar, built-in stresses are small compared to the sintering potential.

The two conditions mentioned before are not fulfilled for the experiments presented in this thesis. Therefore, it shows another limit of the isotropic modeling.

5.3.1.2 LTCC layer on an elastic substrate

Constrained by a green alumina tape

As can be seen in figure 4.31, the simulation fails to predict the camber of a bi-layer green alumina tape / LTCC layer. Experimentally, camber increases continuously, whereas the simulation predicts an increase of the camber at low densities and a further decrease as densification proceeds. Huge discrepancies between the simulation and the experimental results cannot be only attributed to the development of anisotropy during sintering.

At low densities, simulation predicts that the maximal tensile stress observed at the bottom of the sample is around 7 MPa. Ostrowski *et al.*[176] determined the bending strength for alumina sintered to low densities. For a sintered alumina at 1100 ° C with a relative density of 56%, the bending strength is about 5 MPa. In our case, the green density is slightly higher: 59% of relative density, but the sintering temperature is lower: 840 ° C. Moreover, the sample starts to camber around 760 ° C. At this stage, the diffusion process is less advanced than at 1100 ° C : as shown in figure 4.27, Young's modulus increases significantly with temperature, which indicates that necks between particles are being consolidated. Consolidation without densification is believed to be increased up to the sintering temperature. Thus, it is expected that the green alumina tape has a smaller bending strength at 760 ° C than at 1100 ° C and therefore, during sintering of the bi-layer, that numerous microcracks are formed in the elastic substrate. At longer sintering times, when the camber is extremely large ($\approx$ 250 m^{-1}), the substrate shows some macroscopic cracks. The substrate does not fulfill anymore its role, and the LTCC layer is only constrained at some locations.

Simulation for various Young's modulus for the constraining substrate

The simulation can give an insight for which range of the Young's modulus of the constraining substrate the camber is negligible. The following geometrical parameters are taken for the simulation: $h_1 = 240$ μm and $h_2 = 720$ μm. The maximal camber is found to (i) strongly decay with moderate values of the Young's modulus of the constraining substrate (below 10 GPa) and (ii) converge to zero for larger Young's moduli (figure 5.9). If the Young's modulus has values below 10 GPa, a substantial camber can be observed. If the Young's modulus of the constraining substrate is 400 GPa, the maximal camber calculated is 0.11 m^{-1}.

For the simulated cambers with different Young's moduli, the camber increases in the early stage of the simulation and then decreases as time increases. This can be directly correlated to the stress built into the shrinking layer: the highest average transient stress is always observed at low densities.

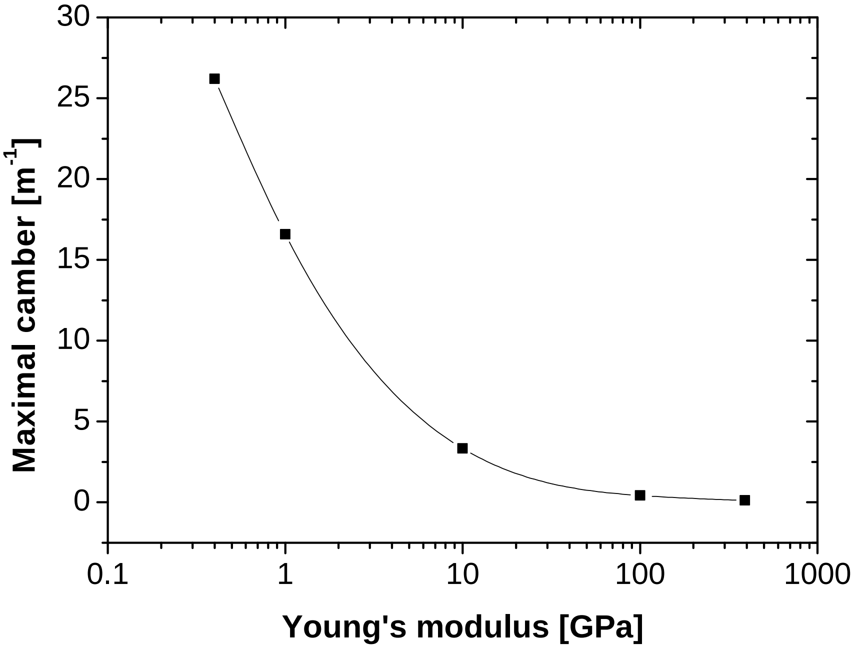

Figure 5.9: Maximal camber as function of Young's modulus of the elastic substrate.

In figure 5.10, the stress built into the LTCC is represented for different values of Young's modulus. When the Young's modulus has a value of 400 GPa, the stress built into the LTCC is identical to the case of the fully constrained LTCC (i.e. the Young's modulus of the constraining substrate tends to infinity) and remains approximately constant along the thickness: the difference between the stress at the top and at the interface 1 reaches a maximum of 12 kPa in the early stages of densification and at relative densities larger than 68%, this difference does not exceed 20 Pa. If the constraining substrate has a lower Young's modulus, the stress is relaxed mainly in the beginning of densification when high incompatibility stresses develop and when the camber is the largest (figure 5.10). As the camber decreases, the stress built into the LTCC remains approximately constant along the thickness and match with the stress calculated for the fully constrained case.

The predicted built-in stress in the LTCC layer for the simulation of the experiment described in § 3.4.3 is also found to be constant along the thickness: the difference between the stress at the top and at the interface 1 reaches a maximum of 115 Pa (which represents 0.05% of the average stress) in the early stages of densification. At relative densities larger than 69%, this difference does not exceed 0.4 Pa. This is in good agreement with the SEM observations where no microstructural differences are found along the thickness.

It is also expected that anisotropy does not influence significantly the camber when the Young's modulus of the constraining substrate is large and the uniaxial viscosity of the shrinking layer is small: changes in the uniaxial viscosity induced by anisotropy remain

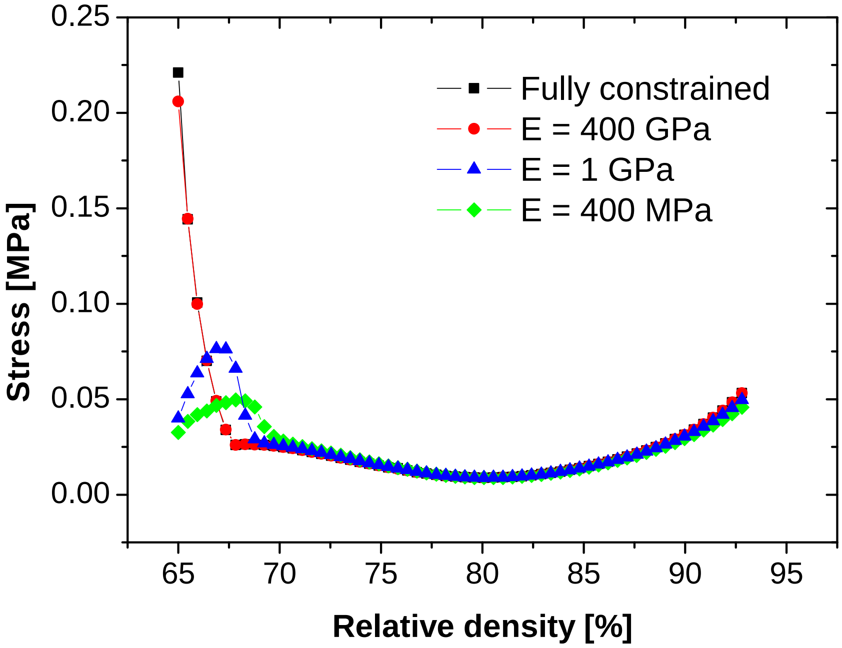

Figure 5.10: Average stresses built into the LTCC layer as function of relative density for elastic substrates with Young's modulus of 400 MPa, 1 GPa, 400 GPa and infinity (fully constrained).

limited.

5.3.2 Sintering of a symmetric laminate

5.3.2.1 Fully constrained

As we have seen before, a shrinking layer can be fully constrained on one side if the Young's modulus is high enough. The stress state is almost identical as if the shrinking layer was constrained from both sides. This validates the assumption that a LTCC layer sintered on a dense alumina substrate can be considered as fully constrained (experiment with the rocking arm - figure 3.4).

By constraining a LTCC layer by a dense alumina substrate, it appears that the densification behavior of a viscous composite like this LTCC is as limited as for polycrystalline alumina films (figure 4.33). According to the continuum mechanical description of sintering, the densification rate of a constrained sample can be predicted from the densification rate of freely sintered laminates and the viscous Poisson's ratio (eq. 2.25). Results are shown in figure 5.11. Discrepancies exist between prediction and the measured curve: predicted values are larger than the ones experimentally measured. Moreover, no early saturation of densification is predicted.

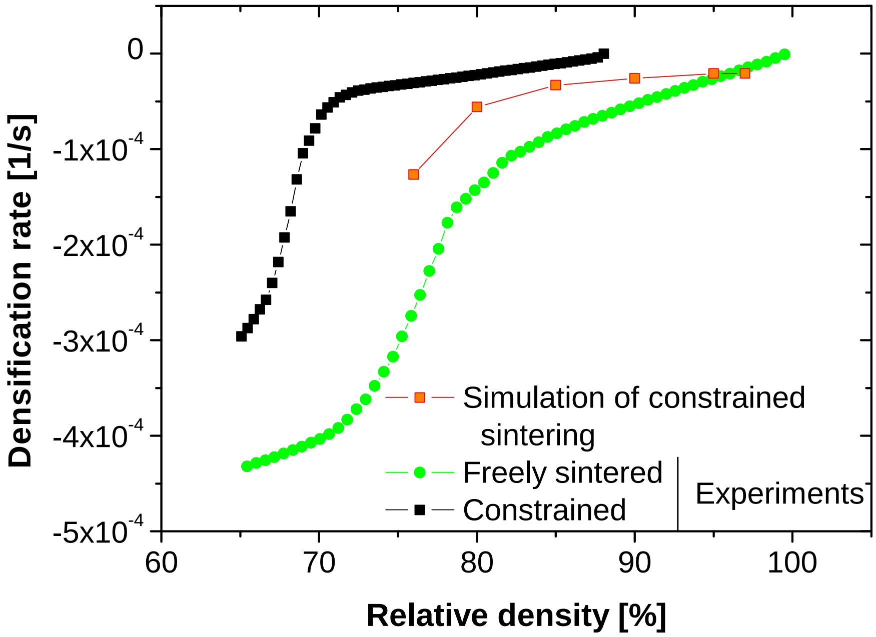

Figure 5.11: Densification rate for laminates (i) freely sintered laminate (ii) constrained by a dense alumina substrate and (iii) simulated when no in-plane shrinkage is allowed.

By taking the opposite approach, the viscous Poisson's ratio can be expressed as a function of the ratio densification rate of a constrained laminate to densification rate of a freely sintered laminate (eq. 2.25):

$$\nu^p = \frac{3\left(\frac{\dot{\rho}^{cons}}{\dot{\rho}^{free}}\right) - 1}{3\left(\frac{\dot{\rho}^{cons}}{\dot{\rho}^{free}}\right) + 1} \tag{5.9}$$

Equation 5.9 is derived considering that the shrinking layer remains isotropic during sintering. For an isotropic material it is widely accepted that the viscous Poisson's ratio varies between 0 and 0.5.[92] The viscous Poisson's ratio obtained from eq. 5.9 is plotted as a function of the ratio densification rate of a constrained laminate to densification rate of a freely sintered laminate in figure 5.12. Viscous Poisson's ratio varies from -1 to +1. In the case where the densification rate of the constrained film is much lower than the densification of a freely sintered laminate, the viscous Poisson's ratio tends to -1. For constrained laminates which exhibit a limit of densification, the apparent viscous Poisson's ratio will thus tend necessarily to -1: as the density of the constrained laminate tends to its limit, the densification rate will tend to zero whereas the free densification rate has a finite value. To predict a viscous Poisson's value larger than 0.5, the densification rate of a constrained laminate needs to be larger than the densification of a freely sintered

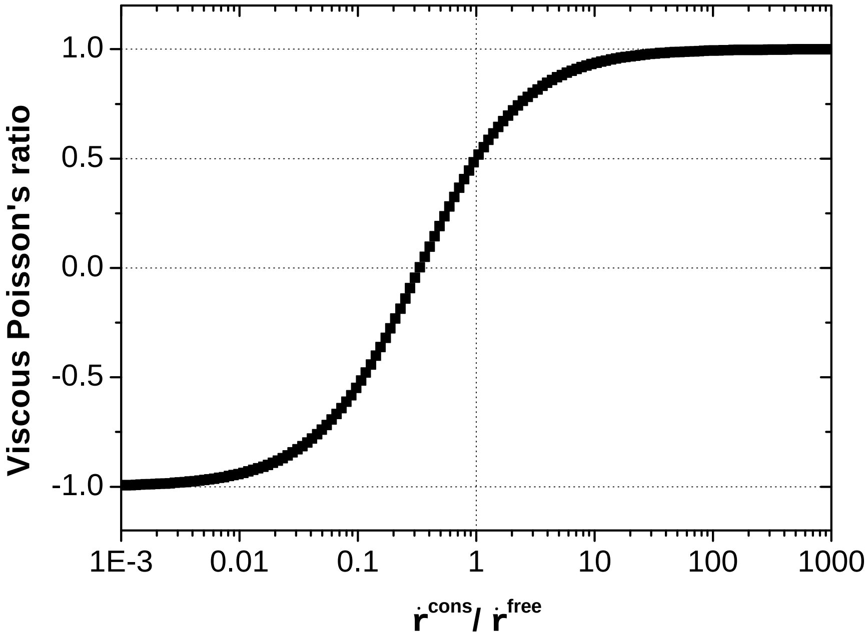

Figure 5.12: Viscous Poisson's ratio as function of the ratio densification rate of a constrained laminate to densification rate of a freely sintered laminate.

laminate. This can be seen for the simulated point at 97% of relative density for which the viscous Poisson's ratio is equal to 0.6 (figure 5.11).

In the literature, it has been found that densification of constrained glasses can be only retarded[147;177] or limited.[105;116;156;178;179] In the first case, Mohanram *et al.*[147] measured the viscous Poisson's ratio using a very similar equation (eq. 2.25). As the material sintered to full density, the viscous Poisson's ratio did not tend to -1. This indicates that anisotropy was not induced during constrained sintering. In the second case, Jagota *et al.*[83] noticed that above 75% of relative density densification of constrained glass films deviates from Scherer's theory. Moreover, it was reported that the presence of silica particles in a borosilicate glass decreases the limit of densification when the film is constrained.[116;156]

In-plane stresses reported in the literature for glasses are calculated either (i) by using eq. 2.24[150;155;179] or (ii) by measuring the camber[116;118;174]. However, it has been previously shown that the second method leads to smaller values than in the reality (figure 5.8). With the first method, values of 10-15 kPa[155], 100 kPa[179] and 200 kPa[150] were reported. With the second method, values of 20 kPa[116], 200 kPa[174] and 0.06 to 6 MPa[118] were reported. They show good agreement with the values reported here (eq. 2.24) which are less than 300 kPa. Moreover, it has been noticed that when a fast heating rate is used (like in this study), the highest stresses develop in the early stage of sintering[116;174], whereas if the heating rate is small the highest tensile stress peak is shifted to higher relative densities where the densification rate is the fastest.[150;151;179]

In the case of constrained sintering of polycrystalline films[63;105;180], isotropic modeling always failed to predict the densification behavior of a constrained film. It has also been attributed to the anisotropy development. For alumina, pores are found to be oriented along the thickness and 4 times larger than the pore size when the film is freely sintered.[63]

5.3.2.2 Degree of constraint

During constrained sintering, two factors in competition influence the densification: the sintering stress which is the driving force for densification and the in-plane tensile stress which develops due to the constraint (eq. 2.24). If the sample is fully constrained, both stresses are equal. In the case where the laminate is allowed to shrink in the plane to some extent, the in-plane tensile stress is lower than the sintering stress. As a result, the shrinking layer is constrained to a certain extent.

Viscous model

In order to relax stresses built-in in the shrinking layer, the substrate needs to shrink in the radial direction (eq. 4.19). For the viscous model (§ 4.3.2.2), the normalized stress σ_N can be calculated using eq. 4.20 and eq. 4.10:

$$\sigma_N = \frac{1}{1 + \frac{h_2}{2h_1} \frac{1-\nu_1^p}{E_1^p} \frac{E_2^p}{1-\nu_2^p}} \tag{5.10}$$

Interestingly, the normalized stress does not depend on the free strain rate of the shrinking layer (the strain rate of the material 1 is zero since the dense LTCC is already dense). It can be noticed that the ratio is much lower than 1 if E_2^p is of the same order than E_1^p. In the early stage of sintering, the uniaxial viscosity of the shrinking layer is too low compared to the uniaxial viscosity of the substrate. It accounts for the inability to relax stresses at such densities. Additionally, the normalized stress can be significantly smaller than 1 if ν_2^p increases.

Elastic model

When the LTCC layer is constrained by a green alumina tape, the densification behavior differs significantly as compared to the case where it is constrained by a dense alumina substrate. Adhesion between the dense alumina substrate and the LTCC layer and between the green alumina tape and the LTCC layer is supposed to be the same as, for both cases, no sliding was observed. Moreover, since the green alumina tape can be easily removed, it is assumed that the glass does not penetrate the constraining layer.

Thus, the different sintering behaviors are supposed to be directly correlated to the elastic properties of the constraining substrate.

For a symmetric laminate constrained by a green alumina tape, the stress predicted by the simulation is only relaxed at high densities (figure 4.38 and 4.39). Radial strains are 0.02%, 0.54% and 3.1% for constrained LTCC layer with a dense alumina substrate, a green alumina tape and a substrate with a Young's modulus of 1 GPa, respectively. Trends and values are comparable to the prediction of the viscous model. If the LTCC layer is constrained by a dense LTCC substrate or by an elastic substrate of 1 GPa, trends and values are similar. Same conclusions can be drawn: in the early stage of sintering, the LTCC is not fluid enough to relax the stresses.

Microstructural observations

Based on experimental observations, the microstructure for laminates freely sintered, partially constrained (constraining substrate is a green alumina tape) and fully constrained (constraining substrate is a dense alumina substrate) are represented schematically in figure 5.13 at the same relative density of 86%. Microstructures were chararacterized far from the free edges. Large microstructural differences are observed which are believed to affect the sintering parameters:

- in the case of laminates freely sintered, pores and particles are slightly oriented in the plane $r\theta$. A transversely isotropic model can be used. The parameters of interest to characterize this microstructure are $E^p_{r,free}$, $\nu^p_{r\theta,free}$, $\dot{\varepsilon}^{free}_{z,free}$ and $\dot{\varepsilon}^{free}_{r,free}$.

- when the LTCC layer is partially constrained, the particles are slightly more oriented and the pore size increases. The new parameters are: $E^p_{r,p.cons}$, $\nu^p_{r\theta,p.cons}$, $\dot{\varepsilon}^{free}_{z,p.cons}$ and $\dot{\varepsilon}^{free}_{r,p.cons}$. Compared to the microstructure of a freely sintered sample, uniaxial viscosity is expected to decrease since the fractional area of alumina particles decreases in the plane $z\theta$ and the free strain rates are expected to be lower as the pores are larger (pore aspect ratio remains similar for both microstructures).

- when the LTCC layer is fully constrained, we observed that the particles keep the same orientation but the pore size increases and pores are elongated in the z direction. The new parameters are: $E^p_{r,f.cons}$, $\nu^p_{r\theta,f.cons}$, $\dot{\varepsilon}^{free}_{z,f.cons}$ and $\dot{\varepsilon}^{free}_{r,f.cons}$. Compared to the microstructure of a freely sintered sample, the uniaxial viscosity in the plane is believed to decrease since elongated pores cause a lower density distribution in the plane. Free strain rate in the plane is also believed to decrease because of the high radius of curvature.

Consistently with numerous works,[155;177;179] it was observed for both degrees of constraining that porosity increases from the free edges to the center of the sample. However,

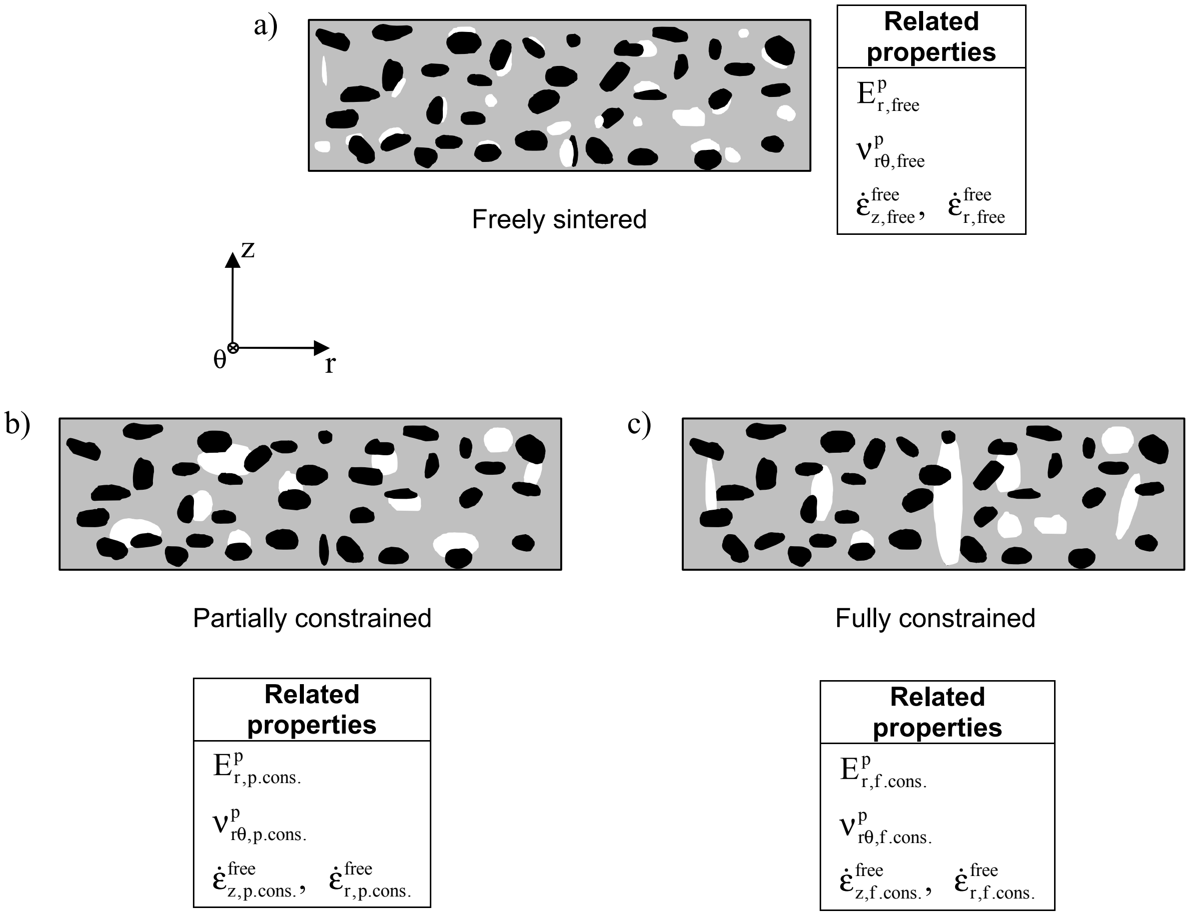

Figure 5.13: Schematic of microstructure at 86% of relative density for a) freely sintered laminate, b) partially constrained laminate and c) fully constrained laminate. Pores, alumina particles and glass matrix are represented in white, black and grey, respectively.

far from the edge, no porosity gradient was observed. Tzeng *et al.*[155] found that pore size does not vary along the thickness but pore density decreases from the interface to the middle. This may be due to the fact that the free edges still influence the stress state at this location.

Compared to the sintering of bi-layers, pores are larger when no camber is allowed: it has been found that pores are 4 times larger in the vicinity of the constraining substrate when the sample is allowed to camber, whereas a factor of 5 to 20 is observed when the sample is not allowed to camber. A relationship can be seen between pore size and predicted stresses: if predicted stresses are larger (case of sintering of symmetric laminates), pores are larger and vice versa. The mechanism suggested by Bordia *et al.*[52] that coalescence of the pores is more likely to produce defects during constrained sintering is then believed to be accurate.

Pore area, pore orientation and particle orientation can be correlated. If the pore area is below a critical size (somewhere between 5 and 10 μm^2), pores will orientate preferentially along the orientation of the particles. If the pores are large enough, alumina particles will not influence anymore the pore orientation, and pores will preferentially orientate perpendicular to the built-in stresses.

Finally, the limit of densification can arise from the fact that the sintering stress is too small to lead to pore shrinkage.[109] This is verified since the highest density reached increases as pore size decreases.

Despite the large microstructural differences, if the LTCC layer is constrained by a green alumina tape, the simulation predicts that the stress is relaxed only to a small extent. However, the calculation is performed by taking the isotropic sintering parameters and evidences of anisotropy development have been found (figure 5.13). Since anisotropy is induced, it is expected that the built-in stress is larger than the isotropic simulation. Thus, higher stresses are reached in the elastic substrates and the stresses built-in in the shrinking layer can be relaxed to a higher extent. In the transversely isotropic case, eq. 2.24 becomes:[64]

$$\sigma^{\infty} = -\frac{\dot{\varepsilon}_r^{free} E_r^p}{1-\nu_{r\theta}^p} \tag{5.11}$$

Considering the microstructural observations of free and constrained laminates (figure 5.13), LTCC materials fully or partially constrained exhibit a smaller uniaxial viscosity as well as a smaller free strain rate in the plane. These two terms tend to lower the built-in stress (eq. 5.11). Therefore, it is expected that the viscous Poisson's ratio in the isotropic plane is larger when the film is constrained.

A possible cause of error could be mentioned: the input sintering parameters for the simulation were measured for the microstructure in figure 5.1 a). The sintering parameters related to this microstructure are indeed different from the sintering parameters related to microstructure in figure 5.13 a), b) and c).

5.4 Prospects

As we have seen, the isotropic model shows some limitations and fails to predict the sintering behavior under constraint. A transversely isotropic model could be used for both sinter-forging and constrained film sintering. However, various difficulties need to be adressed:

- Measurement of the anisotropic sintering parameters
- Quantification of anisotropy, especially at low and high relative densities
- Comparison of anisotropy induced by sinter-forging to anisotropy developed during constrained sintering

Measurement of the seven sintering parameters may be very time consuming.[65] DSF should be performed on square shaped samples with rounded edges for both directions (axial direction - parallel to the pressing direction - and the transverse direction) to determine the sintering parameters when no anisotropy is induced. A second set of experiments should also be performed on samples previously loaded and where the anisotropy induced would have been quantified. Thus, the function f in eq. 5.1 could be calculated and similar expressions could be derived for the 6 other sintering parameters. Some preliminary experimental work from Wonisch *et al.*[65] showed the complexity of the task. However, some experiments can be carried out to calibrate and validate numerical simulations (using for example dissipative particle dynamics).[65]

There is a need to characterize the anisotropy at lower densities. When pores are interconnected, it is particularly difficult to define a pore orientation. Investigation on the recovery effect could be envisaged as a solution. Axial strains and time for recovery may give some hints to define a degree of anisotropy.

The effect of a compressive or a tensile stress is not identical. This is even more critical in the particular case of LTCC where particle and pore orientation as well as pore size are influenced by anisotropy. Thus, microstructures from figure 5.1 and figure 5.13 are not analogous. Moreover, pore size is not influenced by sinter-forging whereas it substantially increases when the film is constrained. Sintering parameters could be measured on laminates instead of bulk samples in order to have the same initial microstructure.

Chapter 6

Summary and outlook

6.1 Summary

Results of this thesis were divided into two parts: sintering under compressive stresses (measurement of the sintering parameters on bulk samples) and sintering under geometrical constraint where built-in stresses develop within the shrinking layer (sintering of laminates).

Sintering parameters

Uniaxial viscosity and viscous Poisson's ratio of an LTCC system were successfully determined in the isotropic case as function of density. Sintering parameters of LTCC glass-ceramic composites were very sensitive to loads. The magnitude of the loads and range of density for which they were applied was crucial for the anisotropy development. Anisotropy changed drastically the apparent value of the uniaxial viscosity and reached a maximum soon after applying large loads. Sintering parameters were further correlated to microstructure: the microstructure became more anisotropic since pores and alumina particles oriented to a large extent perpendicular to the applied load. As a result, the apparent uniaxial viscosity increased.

In order to avoid such mechanically induced anisotropy, discontinuous sinter forging for a validity range of 0.5% of relative density was performed. The obtained uniaxial viscosities increased with density and by decreasing the sintering temperature. The viscous Poisson's ratio presented the same trend for both sintering temperature profiles with a small initial decrease, attributed to the anisotropic free sintering behavior and then an increase, attributed to the increase of density. The hydrostatic sintering stress was calculated and absolute values between 0.1 and 0.4 MPa were small compared to other materials. A large increase in absolute sintering stress was found in the density regime from 90% to 95% and was consistent with recent work on alumina and the expected reduction in pore radius in this density regime.

Sintering of laminates

Two case studies have been investigated experimentally and theoretically: (i) asymmetrical bi-layers and (ii) symmetrical sandwich structures. For each case, elastic and viscous materials were used as constraining substrates. It was shown that built-in stresses were in the first case relaxed by camber and in the second case by an in-plane shrinkage of the constraining substrate.

In the first case, an asymmetric stress state arose due to the differential shrinkage and lead to the camber of the sample. With a viscous constraining substrate, two available models (models by Cai and Kanters) were discussed and compared to experiments. The isotropic simulation failed to reproduce quantitatively the experimental results. It was mainly attributed to the significant anisotropy development due to the constraint. A new model was developed to describe the camber of a viscous layer on an elastic substrate. The effect of the Young's modulus of the elastic substrate was shown to have a strong influence on the camber. For constraining substrates with a high Young's modulus, the model predicted a very small camber and a stress state in the shrinking layer comparable to the one in a symmetric laminate. This was confirmed since no density gradient was observed along the thickness of the shrinking layer. However, due to the limited bending strength of low Young's modulus elastic substrates, the model could not be validated for low Young's moduli.

In the second case, when the constraining substrate did not allow any in-plane shrinkage, the shrinking layer was fully constrained. Isotropic modeling failed to predict the densification behavior of such laminate since it exhibited a limit of densification. Evidences of anisotropy were highlighted: (i) pore area increased by a factor of about 20 at 86% of relative densities compared to pore area determined for freely sintered samples and (ii) pores were oriented in the perpendicular direction to the plane of the laminate. It was further experimentally observed that the densification behavior and microstructure depended to a large extent on the Young's modulus of the outer layers of a sandwich structure. By constraining the shrinking LTCC layer by green alumina tapes, the highest density reached was smaller than the theoretical density but larger than the one obtained when the shrinking layer was fully constrained. Moreover, the pore area was found to be multiplied only by a factor 5 to 10 compared to the pore area determined for freely sintered samples. A simple theoretical approach was developed to account for the elastic deformation of the constraining layers. It was determined that the stress built into the shrinking layer was reduced by this effect. Although this effect was small, it is believed that stresses are more reduced due to the development of anisotropy.

6.2 Outlook

This PhD thesis shows some first evidences of the importance of anisotropy development for glass ceramic composites under compressive and tensile stresses. Nevertheless, future challenges and some improvement can be made. Possible future research fields are listed here:

- First, dielectric properties could be measured for the different microstructures defined in this work. Thus, the maximal degree of constraint could be defined so that the material still meets the requirements to be used for industrial applications.
- Further materials, ideally remaining isotropic under constraint, could be tested to validate the models developed in this thesis.
- Anisotropic constitutive laws for sintering bodies could be used to characterize the sintering behavior of the LTCC material. As we mentioned, a transversely isotropic model should apply to both study cases: sintering under compressive stresses and sintering under geometrical constraint. Models developed by Kanters and the ones in this thesis should be then upgraded in order to implement the anisotropic sintering parameters.
- The model predicting the camber of the bi-layer "viscous layer / elastic substrate" could be adapted to other experiments such as drying of ceramic films.
- Since limitations of the 2D microstructural characterization were shown, there is a need to better characterize the microstructure. A 3D approach is therefore required and the sequential ablation by Focused Ion Beam could be considered as a suitable technique. From this perspective, anisotropy could be then better quantified.
- Finally, numerical simulations could be carried out by using the finite element method or dissipative particle dynamics. Comparison between experimental results and simulations could help to further improve the numerical codes.

Appendix A

Equations for different models

The equations to plot the normalized uniaxial viscosity, $\frac{E^p(\rho)}{E^p(1)}$ and the viscous Poisson's ratio, ν^p in figure 2.11 and 2.12 for the different models are presented below:

1=Raj and Bordia[57]

For $\rho_0 = 0.5$,

$$\frac{E^p(\rho)}{E^p(1)} = \frac{3ln(2)}{3ln(2) - ln(\rho)} \tag{A.1}$$

$$\nu^p(\rho) = \frac{3ln(2) + ln(\rho)}{6ln(2) - 2ln(\rho)} \tag{A.2}$$

2=Venkatachari[73]

$$\frac{E^p(\rho)}{E^p(1)} = (\nu^p(\rho) + 1)\rho \tag{A.3}$$

$$\nu^p(\rho) = \frac{21[\ln(1-\rho) + 0.5\rho(\rho+2)] + 4\rho^2}{42[\ln(1-\rho) + 0.5\rho(\rho+2)] - 4\rho^2} \tag{A.4}$$

3=MacKenzie and Shuttleworth[32]

$$\frac{E^p(\rho)}{E^p(1)} = \frac{4\rho[1 - 5/3(1-\rho)]}{3\rho + 1} \tag{A.5}$$

$$\nu^p(\rho) = \frac{6\rho - 2}{6\rho + 2} \tag{A.6}$$

4=Scherer[31]

$$\frac{E^p(\rho)}{E^p(1)} = \frac{\rho}{3-2\rho} \tag{A.7}$$

$$\nu^p(\rho) = \frac{1}{2}\left(\frac{\rho}{3-2\rho}\right)^{1/2} \tag{A.8}$$

5=Skorokhod[94]

$$\frac{E^p(\rho)}{E^p(1)} = \frac{3\rho^5}{4\rho^3+\rho^2(1-\rho)} \tag{A.9}$$

$$\nu^p(\rho) = \frac{4\rho^3-2\rho^2(1-\rho)}{8\rho^3+2\rho^2(1-\rho)} \tag{A.10}$$

6=Ducamp[68]

The exponential factor α is experimentally evaluated. From Ducamp's results, $\alpha = 4$. Note that no model was proposed for the viscous Poisson's ratio.

$$\frac{E^p(\rho)}{E^p(1)} = \frac{4\rho\exp(-\alpha(1-\rho)/\rho)}{3\rho+1} \tag{A.11}$$

7=Rahaman[85]

The exponential factor a_0 is experimentally evaluated. From Rahaman's results, $a_0 = 11$.

$$\frac{E^p(\rho)}{E^p(1)} = \frac{4\rho\exp(-2a_0(1-\rho)}{3+\exp(-a_0(1-\rho)} \tag{A.12}$$

$$\nu^p(\rho) = \frac{1}{2}\left(\frac{3\exp(-a_0(1-\rho))-2}{3+\exp(-a_0(1-\rho))}\right) \tag{A.13}$$

8=Hsueh[89]

The values for the following parameters derived from Hsueh's model were taken: $\rho_0 = 0.5$ $\tau = 190.5$ s $\gamma = 1.67$ $\lambda = 1.67$ $p = 0.5$ $\Sigma = -1.0$ MPa $\eta_0 = 100$ GPa.s
The uniaxial viscosity is normalized at 99% of relative density as it tends to infinity when the relative density approaches full density.

$$\frac{E^p(\rho)}{E^p(0.99)} = \frac{(\nu^p(\rho)+1)2\rho^p(1-\rho)^{-\lambda}}{(\nu^p(0.99)+1)2\times 0.99^p(1-0.99)^{-\lambda}} \tag{A.14}$$

$$\nu^p(\rho) = \frac{-3\tau\Sigma\gamma\rho(1-\rho_0)^\gamma(1-\rho)^\lambda - 2\eta_0 1\rho^p(1-\rho)^{1+\gamma}}{2\left[\eta_0\rho^p(1-\rho)^{1+\gamma} - 3\tau\Sigma\gamma\rho(1-\rho_0)^\gamma(1-\rho)^\lambda\right]} \tag{A.15}$$

Appendix B

Kanters' model / integration procedure

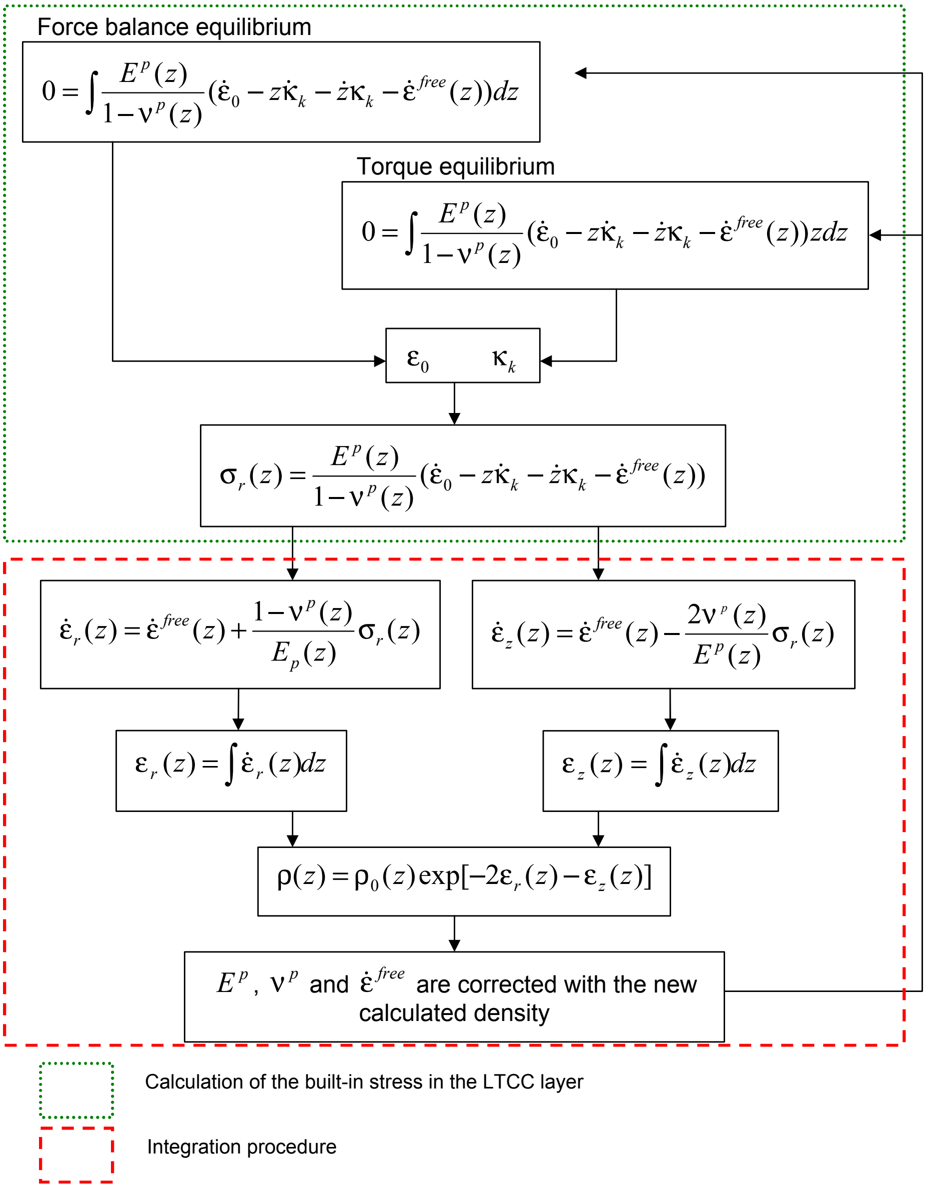

Figure B.1: Calculation of the built-in stress according to Kanters in the LTCC layer with the integration procedure: the built-in stresses influence densification and the sintering parameters.

References

[1] R. Kulke, V. Wahle, D. Sollbach, P. Uhlig, M. Rittweger, S.-P. Schmitz, and P. Waldow. High level of integration for bluetooth modules on LTCC. In *14th European Microelectronics and Packaging conference & Exhibition*, Friedrichshafen, Germany, June 2003.

[2] R. R. Tummala. Ceramic and glass-ceramic packaging in the 1990s. *Journal of the American Ceramic Society*, 74(5):895–908, May 1991.

[3] Y. Shimada, K. Utsumi, M. Suzuki, H. Takamizawa, M. Nitta, and T. Watari. Low firing temperature multilayer glass ceramic substrate. *IEEE Transactions on Components, Hybrids and Manufacturing Technology*, 6(4):382–388, 1983.

[4] N. Ilkov, W. Bakalski, R. Matz, W. Simbürger, O. Dernovsek, and P. Weger. A 5 to 6.5 GHz LTCC power amplifier module. *Advancing microelectronics*, 31(2):7–9, 2004.

[5] T. G. Reynolds. Application space influences electronic ceramic materials. *American Ceramic Society Bulletin*, 80(10):29–33, October 2001.

[6] K.-L. Wu and Y. Huang. LTCC technology and its applications in high frequency front end modules. In *Antennas, Propagation and EM Theory, 2003. Proceedings. 2003 6th International Symposium on*, pages 730–734, 2003.

[7] Y. G. Wang, G. N. Zhang, and J. S. Ma. Research of LTCC/Cu, Ag multilayer substrate in microelectronic packaging. *Materials Science and Engineering B-Solid State Materials for Advanced Technology*, 94(1):48–53, June 2002.

[8] C.Q. Scrantom and J.C. Lawson. LTCC technology: where we are and where we're going. II. In *Technologies for Wireless Applications, 1999. Digest. 1999 IEEE MTT-S Symposium on*, pages 193–200, 1999.

[9] M. Valant and D. Suvorov. Glass-free low-temperature cofired ceramics: calcium germanates, silicates and tellurates. *Journal of the European Ceramic Society*, 24(6):1715–1719, 2004.

[10] H. Jantunen, T. Kangasvieri, J. Vähäkangas, and S. Leppävuori. Design aspects of microwave components with LTCC technique. *Journal of the European Ceramic Society*, 23(14):2541–2548, 2003.

[11] F. Lautzenhiser and E. Amaya. Self-constrained LTCC tape. *American Ceramic Society Bulletin*, 81(10):27–32, October 2002.

[12] S. X. H. Dai, R. F. Huang, and D. L. Wilcox. Use of titanates to achieve a temperature-stable low-temperature cofired ceramic dielectric for wireless applications. *Journal of the American Ceramic Society*, 85(4):828–832, April 2002.

[13] H. Jantunen. *A novel low temperature co-firing ceramic (LTCC) material for telecommunication devices*. PhD thesis, Department of Electrical Engineering and Infotech Oulu, University of Oulu, 2001.

[14] M. R. Gongora-Rubio, P. Espinoza-Vallejos, L. Sola-Laguna, and J. J. Santiago-Aviles. Overview of low temperature co-fired ceramics tape technology for meso-system technology (MsST). *Sensors and Actuators A-Physical*, 89(3):222–241, April 2001.

[15] P. K. Khanna, B. Hornbostel, M. Burgard, W. Schafer, and J. Dorner. Studies on three-dimensional moulding, bonding and assembling of low-temperature-cofired ceramics for MEMS and MST applications. *Materials Chemistry and Physics*, 89(1):72–79, January 2005.

[16] M. Eberstein, J. Möller, J. Wiegmann, and W. A. Schiller. Modification and simulation of dielectric properties of glass/crystal phase-composites for LTCC-applications. *Cfi-Ceramic Forum International*, 80(5):E39–E46, May 2003.

[17] M. Valant and D. Suvorov. Microstructural phenomena in low-firing ceramics. *Materials Chemistry and Physics*, 79(2-3):104–110, April 2003.

[18] Y. J. Choi, J. H. Park, J. H. Park, and J. G. Park. Middle-permittivity LTCC dielectric compositions with adjustable temperature coefficient. *Materials Letters*, 58(25):3102–3106, October 2004.

[19] T. Rabe, M. Gemeinert, and W. A. Schiller. Development of advanced low temperature co-fired ceramics (LTCC). *Euro Ceramics Viii, Pts 1-3*, 264-268:1181–1184, 2004.

[20] T. Rabe, W. A. Schiller, T. Hochheimer, C. Modes, and A. Kipka. Zero shrinkage of LTCC by self-constrained sintering. *International Journal of Applied Ceramic Technology*, 2(5):374–382, 2005.

[21] Y. Cho, J.R. Rellick, and K.W. Hang. LTCC tape composition - Patent EP1509479, March 2005.

[22] A.K. Kumar, S. Knickerbocker, and R.R. Tummala. Sinterable glass-ceramics for high-performance substrates. In *Electronic Components and Technology Conference, 1992. Proceedings., 42nd*, pages 678–681, 1992.

[23] K. P. Surendran, P. Mohanan, and M. T. Sebastian. The effect of glass additives on the microwave dielectric properties of $Ba(Mg_{1/3}Ta_{2/3})O_3$ ceramics. *Journal of Solid State Chemistry*, 177(11):4031–4046, November 2004.

[24] M. Hrovat, J. Holc, S. Drnovsek, D. Belavic, J. Bernard, M. Kosec, L. Golonka, A. Dziedzic, and J. Kita. Characterization of PZT thick films fired on LTCC substrates. *Journal of Materials Science Letters*, 22(17):1193–1195, September 2003.

[25] P. C. Panda and R. Raj. Sintering and crystallization of glass at constant heating rates. *Journal of the American Ceramic Society*, 72(8):1564–1566, August 1989.

[26] J.R. Reed. *Principles of ceramics processing.* Wiley & Sons, 1995.

[27] M. O. Prado and E. D. Zanotto. Glass sintering with concurrent crystallization. *Comptes Rendus Chimie*, 5(11):773–786, November 2002.

[28] J. Frenkel. Viscous flow of crystalline bodies. *Zhurnal Eksperimentalnoi I Teoreticheskoi Fiziki*, 16(1):29–38, 1946.

[29] W. D. Kingery, H. K. Bowen, and D. R. Uhlmann. *Introduction to ceramics.* Wiley & Sons, 1976.

[30] G. W. Scherer. Cell models for viscous sintering. *Journal of the American Ceramic Society*, 74(7):1523–1531, July 1991.

[31] G. W. Scherer. Sintering of low-density glasses. I. Theory. *Journal of the American Ceramic Society*, 60(5-6):236–239, 1977.

[32] J. K. MacKenzie and R. Shuttleworth. A phenomenological theory of sintering. *Proc. Phys. Soc. B*, 62(12):833–852, 1949.

[33] M. O. Prado, E. D. Zanotto, and R. Muller. Model for sintering polydispersed glass particles. *Journal of Non-Crystalline Solids*, 279(2-3):169–178, February 2001.

[34] M. J. Pascual, A. Duran, M. O. Prado, and E. D. Zanotto. Model for sintering devitrifying glass particles with embedded rigid fibers. *Journal of the American Ceramic Society*, 88(6):1427–1434, June 2005.

[35] E. D. Zanotto and M. O. Prado. Isothermal sintering with concurrent crystallisation of monodispersed and polydispersed glass particles. part I. *Physics and Chemistry of Glasses*, 42(3):191–198, June 2001.

[36] A. Jagota and P. R. Dawson. Simulation of the viscous sintering of 2 particles. *Journal of the American Ceramic Society*, 73(1):173–177, January 1990.

[37] A. Jagota. Simulation of the viscous sintering of coated particles. *Journal of the American Ceramic Society*, 77(8):2237–2239, August 1994.

[38] A. van de Vorst. Numerical simulation of viscous sintering by a periodic lattice of a representative unit cell. *Journal of the American Ceramic Society*, 81(8):2147–2156, August 1998.

[39] H. Zhou and J. J. Derby. An assessment of a parallel, finite element method for three-dimensional, moving-boundary flows driven by capillarity for simulation of viscous sintering. *International Journal for Numerical Methods in Fluids*, 36(7):841–867, August 2001.

[40] S. Bordere, D. Gendron, J. M. Heintz, and D. Bernard. Monte carlo prediction of non-newtonian viscous sintering: Experimental validation for the two-glass-cylinder system. *Journal of the American Ceramic Society*, 88(8):2071–2078, August 2005.

[41] R. W. Hopper. Coalescence of 2 equal cylinders - exact results for creeping viscous plane flow driven by capillarity. *Journal of the American Ceramic Society*, 67(12):C262–C264, 1984.

[42] J. W. Ross, W. A. Miller, and G. C. Weatherly. Dynamic computer-simulation of viscous-flow sintering kinetics. *Journal of Applied Physics*, 52(6):3884–3888, 1981.

[43] E. Wittman and E. D. Zanotto. Surface nucleation and growth in anorthite glass. *Journal of Non-Crystalline Solids*, 271(1-2):94–99, June 2000.

[44] M. Ferraris and E. Verne. Viscous phase sintering of particle-reinforced glass matrix composites. *Journal of the European Ceramic Society*, 16(4):421–427, 1996.

[45] Rahaman. *Ceramic processing and sintering.* Marcel Dekker, 2003.

[46] E. Bernardo, F. Andreola, L. Barbieri, and I. Lancellotti. Sintered glass-ceramics and glass-ceramic matrix composites from CRT panel glass. *Journal of the American Ceramic Society*, 88(7):1886–1891, July 2005.

[47] Y. Imanaka. *Multilayered Low Temperature Cofired Ceramics (LTCC) Technology.* Springer, 2005.

[48] G. Ewsuk and L. W. Harrison. *Densification of Glass-Filled Alumina.* Ceramic Transactions - Editor C. A. Handwerker, J. E. Blendell, and W. A. Kaysser., 1990.

[49] H. M. Jaeger and S. R. Nagel. Physics of the granular state. *Science*, 255(5051):1523–1531, March 1992.

[50] K.G. Ewsuk and L.W. Harrison. Manufacturing tailored property ceramic composites. In *Design for Manufacturability and Manufacture of Ceramic Components Symposium (96th: 1994: Indianapolis, Indiana)*, 1994.

[51] S. Kemethmüller, M. Hagymasi, A. Stiegelschmitt, and A. Roosen. Viscous flow as the driving force for the densification of low-temperature co-fired ceramics. *Journal of the American Ceramic Society*, 90(1):64–70, January 2007.

[52] R. K. Bordia and R. Raj. Sintering behavior of ceramic films constrained by a rigid substrate. *Journal of the American Ceramic Society*, 68(6):287–292, 1985.

[53] G. W. Scherer and T. Garino. Viscous sintering on a rigid substrate. *Journal of the American Ceramic Society*, 68(4):216–220, 1985.

[54] G. W. Scherer. Sintering with rigid inclusions. *Journal of the American Ceramic Society*, 70(10):719–725, October 1987.

[55] Z. Z. Du and A. C. F. Cocks. Constitutive models for the sintering of ceramic components. I. Material models. *Acta Metallurgica et Materialia*, 40(8):1969–1979, August 1992.

[56] P. Z. Cai, G. L. Messing, and D. L. Green. Determination of the mechanical response of sintering compacts by cyclic loading dilatometry. *Journal of the American Ceramic Society*, 80(2):445–452, February 1997.

[57] R. Raj and R. K. Bordia. Sintering behavior of bi-modal powder compacts. *Acta Metallurgica*, 32(7):1003–1019, 1984.

[58] R. K. Bordia and G. W. Scherer. On constrained sintering. I. Constitutive model for a sintering body. *Acta Metallurgica*, 36(9):2393–2397, September 1988.

[59] G. W. Scherer and S. M. Rekhson. Viscoelastic-elastic composites. I. General-theory. *Journal of the American Ceramic Society*, 65(7):352–360, 1982.

[60] R.M. Christiansen. *Theory of Viscoelasticity, An introduction.* Academic Press, New-York, 1982.

[61] W. Beere. Second stage sintering kinetics of powder compacts. *Acta Metallurgica*, 23(1):139–145, 1975.

[62] R. Raj. Analysis of the sintering pressure. *Journal of the American Ceramic Society*, 70(9):C210–C211, September 1987.

[63] O. Guillon, S. Krauss, and J. Rödel. Influence of thickness on the constrained sintering of alumina films. *Journal of the European Ceramic Society*, 27(7):2623–2627, 2007.

[64] R. K. Bordia, R. Z. Zuo, O. Guillon, S. M. Salamone, and J. Rödel. Anisotropic constitutive laws for sintering bodies. *Acta Materialia*, 54(1):111–118, January 2006.

[65] A. Wonisch, O. Guillon, T. Kraft, M. Moseler, H. Riedel, and J. Rödel. Stress-induced anisotropy of sintering alumina: Discrete element modelling and experiments. *Acta Materialia*, 55(15):5187–5199, September 2007.

[66] S. H. Lee, G. L. Messing, and D. J. Green. Bending creep test to measure the viscosity of porous materials during sintering. *Journal of the American Ceramic Society*, 86(6):877–882, June 2003.

[67] H. Kim, O. Gillia, and D. Bouvard. A phenomenological constitutive model for the sintering of alumina powder. *Journal of the European Ceramic Society*, 23(10):1675–1685, September 2003.

[68] V. C. Ducamp and R. Raj. Shear and densification of glass powder compacts. *Journal of the American Ceramic Society*, 72(5):798–804, May 1989.

[69] M. N. Rahaman and L. C. De Jonghe. Sintering of spherical glass powder under a uniaxial-stress. *Journal of the American Ceramic Society*, 73(3):707–712, March 1990.

[70] M. N. Rahaman, L. C. De Jonghe, G. W. Scherer, and R. J. Brook. Creep and densification during sintering of glass powder compacts. *Journal of the American Ceramic Society*, 70(10):766–774, October 1987.

[71] R. Z. Zuo, E. Aulbach, and J. Rödel. Viscous Poisson's coefficient determined by discontinuous hot forging. *Journal of Materials Research*, 18(9):2170–2176, September 2003.

[72] R. Z. Zuo, E. Aulbach, R. K. Bordia, and J. Rödel. Critical evaluation of hot forging experiments: Case study in alumina. *Journal of the American Ceramic Society*, 86(7):1099–1105, July 2003.

[73] K. R. Venkatachari and R. Raj. Shear deformation and densification of powder compacts. *Journal of the American Ceramic Society*, 69(6):499–506, June 1986.

[74] R. Z. Zuo, E. Aulbach, and J. Rödel. Experimental determination of sintering stresses and sintering viscosities. *Acta Materialia*, 51(15):4563–4574, September 2003.

[75] R. Z. Zuo and J. Rödel. Temperature dependence of constitutive behaviour for solid-state sintering of alumina. *Acta Materialia*, 52(10):3059–3067, June 2004.

[76] S. M. Salamone, L. C. Stearns, R. K. Bordia, and M. P. Harmer. Effect of rigid inclusions on the densification and constitutive parameters of liquid-phase-sintered $YBa_2Cu_3O_{6+x}$ powder compacts. *Journal of the American Ceramic Society*, 86(6):883–892, June 2003.

[77] M. M. R. Boutz, L. Winnubst, A. J. Burggraaf, M. Nauer, and C. Carry. Low-temperature sinter forging of nanostructured Y-TZP and YCe-TZP. *Journal of the American Ceramic Society*, 78(1):121–128, January 1995.

[78] J. Chang, O. Guillon, J. Rödel, and S. J. L. Kang. Uniaxial viscosity of gadolinium-doped ceria determined by discontinuous sinter forging. *Journal of the European Ceramic Society*, 27(10):3127–3133, 2007.

[79] J. Svoboda, H. Riedel, and H. Zipse. Equilibrium pore surfaces, sintering stresses and constitutive-equations for the intermediate and late stages of sintering. I. Computation of equilibrium surfaces. *Acta Metallurgica et Materialia*, 42(2):435–443, February 1994.

[80] H. Riedel, H. Zipse, and J. Svoboda. Equilibrium pore surfaces, sintering stresses and constitutive-equations for the intermediate and late stages of sintering. II. Diffusional densification and creep. *Acta Metallurgica et Materialia*, 42(2):445–452, February 1994.

[81] F. Wakai, Y. Shinoda, and T. Akatsu. Methods to calculate sintering stress of porous materials in equilibrium. *Acta Materialia*, 52(19):5621–5631, November 2004.

[82] F. Parhami and R. M. MacMeeking. A network model for initial stage sintering. *Mechanics of Materials*, 27(2):111–124, February 1998.

[83] A. Jagota, K. R. Mikeska, and R. K. Bordia. Isotropic constitutive model for sintering particle packings. *Journal of the American Ceramic Society*, 73(8):2266–2273, August 1990.

[84] T. Kraft and H. Riedel. Numerical simulation of solid state sintering; model and application. *Journal of the European Ceramic Society*, 24(2):345–361, 2004.

[85] M. N. Rahaman, L. C. De Jonghe, and R. J. Brook. Effect of shear-stress on sintering. *Journal of the American Ceramic Society*, 69(1):53–58, January 1986.

[86] M. N. Rahaman and L. C. De Jonghe. Creep-sintering of zinc oxide. *Journal of Materials Science*, 22(12):4326–4330, December 1987.

[87] F. Wakai, K. Chihara, and M. Yoshida. Anisotropic shrinkage induced by particle rearrangement in sintering. *Acta Materialia*, 55(13):4553–4566, August 2007.

[88] R. M. MacMeeking and L. T. Kuhn. A diffusional creep law for powder compacts. *Acta Metallurgica et Materialia*, 40(5):961–969, May 1992.

[89] C. H. Hsueh, A. G. Evans, R. M. Cannon, and R. J. Brook. Viscoelastic stresses and sintering damage in heterogeneous powder compacts. *Acta Metallurgica*, 34(5):927–936, May 1986.

[90] C. L. Martin, L. C. R. Schneider, L. Olmos, and D. Bouvard. Discrete element modeling of metallic powder sintering. *Scripta Materialia*, 55(5):425–428, September 2006.

[91] B. Henrich, A. Wonisch, T. Kraft, M. Moseler, and H. Riedel. Simulations of the influence of rearrangement during sintering. *Acta Materialia*, 55(2):753–762, January 2007.

[92] R. K. Bordia and G. W. Scherer. On constrained sintering. II. Comparison of constitutive models. *Acta Metallurgica*, 36(9):2399–2409, September 1988.

[93] G. W. Scherer. Sintering with rigid inclusions - reply. *Journal of the American Ceramic Society*, 71(6):C315–C316, June 1988.

[94] V.V. Skorokhod. On phenomenological theory in the sintering of porous bodies. *Poroskova Metall.*, 2:14–20, 1961.

[95] R. L. Coble and W. D. Kingery. Effect of porosity on physical properties of sintered alumina. *Journal of the American Ceramic Society*, 39(11):377–385, 1956.

[96] W. Beere. Unifying theory of stability of penetrating liquid-phases and sintering pores. *Acta Metallurgica*, 23(1):131–138, 1975.

[97] V. M. Sura and P. C. Panda. Viscosity of porous glasses. *Journal of the American Ceramic Society*, 73(9):2697–2701, September 1990.

[98] L. F. Nielsen. Elastic properties of 2-phase materials. *Materials Science and Engineering*, 52(1):39–62, 1982.

[99] R. Raj. Separation of cavitation-strain and creep-strain during deformation. *Journal of the American Ceramic Society*, 65(3):C46–C46, 1982.

[100] M. Y. Chu, L. C. De Jonghe, and M. N. Rahaman. Effect of temperature on the densification-creep viscosity during sintering. *Acta Metallurgica*, 37(5):1415–1420, May 1989.

[101] R. K. Bordia and R. Raj. Analysis of sintering of a composite with a glass or ceramic matrix. *Journal of the American Ceramic Society*, 69(3):C55–C57, March 1986.

[102] J. Kanters, U. Eisele, and J. Rödel. Cosintering simulation and experimentation: Case study of nanocrystalline zirconia. *Journal of the American Ceramic Society*, 84(12):2757–2763, December 2001.

[103] A. Jagota and C. Y. Hui. Mechanics of sintering thin-films. I. Formulation and analytical results. *Mechanics of Materials*, 9:107–119, 1990.

[104] T. J. Garino and H. K. Bowen. Deposition and sintering of particle films on a rigid substrate. *Journal of the American Ceramic Society*, 70(11):C315–C317, November 1987.

[105] T. J. Garino and H. K. Bowen. Kinetics of constrained-film sintering. *Journal of the American Ceramic Society*, 73(2):251–257, February 1990.

[106] T. N. Cheng and R. Raj. Flaw generation during constrained sintering of metal-ceramic and metal glass multilayer films. *Journal of the American Ceramic Society*, 72(9):1649–1655, September 1989.

[107] P. Z. Cai, D. J. Green, and G. L. Messing. Constrained densification of alumina/zirconia hybrid laminates. I. Experimental observations of processing defects. *Journal of the American Ceramic Society*, 80(8):1929–1939, August 1997.

[108] A. Jagota and C. Y. Hui. Mechanics of sintering thin-films. II. Cracking due to self-stress. *Mechanics of Materials*, 11(3):221–234, May 1991.

[109] C. H. Hsueh. Sintering of a ceramic film on a rigid substrate. *Scripta Metallurgica*, 19(10):1213–1217, 1985.

[110] J. W. Choe, J. N. Calata, and G. Q. Lu. Constrained-film sintering of a gold circuit paste. *Journal of Materials Research*, 10(4):986–994, April 1995.

[111] M. Stech, P. Reynders, and J. Rödel. Constrained film sintering of nanocrystalline TiO_2. *Journal of the American Ceramic Society*, 83(8):1889–1896, August 2000.

[112] D. R. Carroll and M. N. Rahaman. An initial-stage model for the sintering of constrained polycrystalline thin-films. *Journal of the European Ceramic Society*, 14(5):473–479, 1994.

[113] R. K. Bordia and A. Jagota. Crack-growth and damage in constrained sintering films. *Journal of the American Ceramic Society*, 76(10):2475–2485, October 1993.

[114] D.J. Green, O. Guillon, and J. Rödel. Constrained sintering: A delicate balance of scales. *Journal of the European Ceramic Society*, 28(7):1451–1466, 2008.

[115] C. R. Chang and J. H. Jean. Effects of silver-paste formulation on camber development during the cofiring of a silver-based, low-temperature-cofired ceramic package. *Journal of the American Ceramic Society*, 81(11):2805–2814, November 1998.

[116] J. Bang and G. Q. Lu. Constrained-film sintering of a borosilicate glass - in-situ measurement of film stresses. *Journal of the American Ceramic Society*, 78(3):813–815, March 1995.

[117] P. Z. Cai, D. J. Green, and G. L. Messing. Constrained densification of alumina/zirconia hybrid laminates. II. Viscoelastic stress computation. *Journal of the American Ceramic Society*, 80(8):1940–1948, August 1997.

[118] G. Q. Lu, R. C. Sutterlin, and T. K. Gupta. Effect of mismatched sintering kinetics on camber in a low-temperature cofired ceramic package. *Journal of the American Ceramic Society*, 76(8):1907–1914, August 1993.

[119] J. H. Jean and C. R. Chang. Camber development during cofiring Ag-based low-dielectric-constant ceramic package. *Journal of Materials Research*, 12(10):2743–2750, October 1997.

[120] J. H. Jean and C. R. Chang. Cofiring kinetics and mechanisms of an Ag-metallized ceramic-filled glass electronic package. *Journal of the American Ceramic Society*, 80(12):3084–3092, December 1997.

[121] R. Szilard. *Theories and Applications of Plate Analysis: Classical Numerical and Numerical Methods*. Wiley & Sons, 2004.

[122] A. G. Evans and J. W. Hutchinson. The thermomechanical integrity of thin-films and multilayers. *Acta Metallurgica et Materialia*, 43(7):2507–2530, July 1995.

[123] S. Suresh, A. E. Giannakopoulos, and M. Olsson. Elastoplastic analysis of thermal cycling - layered materials with sharp interfaces. *Journal of the Mechanics and Physics of Solids*, 42(6):979–1018, June 1994.

[124] B.B. Stoney. The tension of metallic films deposited by electrolysis. *Proceedings of the Royal Society London A*, 82:172–175, 1909.

[125] R. K. Bordia and G. W. Scherer. On constrained sintering. III. Rigid inclusions. *Acta Metallurgica*, 36(9):2411–2416, September 1988.

[126] M. N. Rahaman and L. C. De Jonghe. Effect of rigid inclusions on the sintering of glass powder compacts. *Journal of the American Ceramic Society*, 70(12):C348–C351, December 1987.

[127] C. H. Hsueh. Sintering with rigid inclusions - comment. *Journal of the American Ceramic Society*, 71(6):C314–C315, June 1988.

[128] Z. Hashin and S. Shtrikman. A variational approach to the theory of the elastic behaviour of multiphase materials. *Journal of the Mechanics and Physics of Solids*, 11(2):127–140, 1963.

[129] R. E. Dutton and M. N. Rahaman. Sintering, creep, and electrical-conductivity of model glass-matrix composites. *Journal of the American Ceramic Society*, 75(8):2146–2154, August 1992.

[130] A. R. Boccaccini and E. A. Olevsky. Processing of platelet-reinforced glass matrix composites: effect of inclusions on sintering anisotropy. *Journal of Materials Processing Technology*, 96(1-3):92–101, November 1999.

[131] L. H. He and J. H. Zhao. Influence of inclusion shape on viscous sintering. *Journal of Non-Crystalline Solids*, 316(2-3):384–388, February 2003.

[132] E. A. Giess, J. P. Fletcher, and L. W. Herron. Isothermal sintering of cordierite-type glass powders. *Journal of the American Ceramic Society*, 67(8):549–552, 1984.

[133] H. E. Exner and E. A. Giess. Anisotropic shrinkage of cordierite-type glass powder cylindrical compacts. *Journal of Materials Research*, 3(1):122–125, January 1988.

[134] E. A. Olevsky. Theory of sintering: from discrete to continuum. *Materials Science and Engineering R-Reports*, 23(2):41–100, June 1998.

[135] P. M. Raj and W. R. Cannon. Anisotropic shrinkage in tape-cast alumina: Role of processing parameters and particle shape. *Journal of the American Ceramic Society*, 82(10):2619–2625, October 1999.

[136] J. S. Sung, K. D. Koo, and J. H. Park. Lamination and sintering shrinkage behavior in multilayered ceramics. *Journal of the American Ceramic Society*, 82(3):537–544, March 1999.

[137] E. A. Olevsky and R. M. German. Effect of gravity on dimensional change during sintering. I. Shrinkage anisotropy. *Acta Materialia*, 48(5):1153–1166, March 2000.

[138] E. A. Olevsky, R. M. German, and A. Upadhyaya. Effect of gravity on dimensional change during sintering. II. Shape distortion. *Acta Materialia*, 48(5):1167–1180, March 2000.

[139] A. R. Boccaccini and E. A. Olevsky. Anisotropic shrinkage during sintering of glass-powder compacts under uniaxial stresses: Qualitative assessment of experimental evidence. *Metallurgical and Materials Transactions A-Physical Metallurgy and Materials Science*, 28(11):2397–2404, November 1997.

[140] A. R. Boccaccini. Shrinkage anisotropy of glass powder compacts sintered in dilatometers. *Journal of Materials Research*, 13(6):1693–1697, June 1998.

[141] A. R. Boccaccini and B. Hamann. In situ high-temperature optical microscopy. *Journal of Materials Science*, 34(22):5419–5436, November 1999.

[142] A. Mohanram, G. L. Messing, and D. J. Green. Measurement of viscosity of densifying glass-based systems by isothermal cyclic loading dilatometry. *Journal of the American Ceramic Society*, 87(2):192–196, February 2004.

[143] M. Rauscher and A. Roosen. Influence of low-temperature co-fired ceramics green tape characteristics on shrinkage behavior. *International Journal of Applied Ceramic Technology*, 4(5):387–397, 2007.

[144] J. C. Chang and J. H. Jean. Self-constrained sintering of mixed low-temperature-cofired ceramic laminates. *Journal of the American Ceramic Society*, 89(3):829–835, March 2006.

[145] J. C. Chang and J. H. Jean. Camber development during the cofiring of bi-layer glass-based dielectric laminate. *Journal of the American Ceramic Society*, 88(5):1165–1170, May 2005.

[146] R. J. Xie, R. Z. Zuo, E. Aulbach, U. Mackens, N. Hirosaki, and J. Rödel. Uniaxial viscosity of low-temperature cofired ceramic (LTCC) powder compacts determined by loading dilatometry. *Journal of the European Ceramic Society*, 25(4):417–424, April 2005.

[147] A. Mohanram, S. H. Lee, G. L. Messing, and D. J. Green. A novel use of constrained sintering to determine the viscous Poisson's ratio of densifying materials. *Acta Materialia*, 53(8):2413–2418, May 2005.

[148] A. Mohanram, G. L. Messing, and D. J. Green. Densification and sintering viscosity of low-temperature co-fired ceramics. *Journal of the American Ceramic Society*, 88(10):2681–2689, October 2005.

[149] C. D. Lei and J. H. Jean. Effect of crystallization on the stress required for constrained sintering of CaO-B_2O_3-SiO_2 glass-ceramics. *Journal of the American Ceramic Society*, 88(3):599–603, March 2005.

[150] C. C. Huang and J. H. Jean. Stress required for constrained sintering of a ceramic-filled glass composite. *Journal of the American Ceramic Society*, 87(8):1454–1458, August 2004.

[151] Y. C. Lin and J. H. Jean. Constrained sintering of silver circuit paste. *Journal of the American Ceramic Society*, 87(2):187–191, February 2004.

[152] W. X. Li and J. J. Lannutti. Curvature evolution in LTCC tapes and laminates. *IEEE Transactions on Components and Packaging Technologies*, 28(1):149–156, March 2005.

[153] M. Wagner, A. Roosen, A. Stiegelschmitt, D. Schwanke, and F. Bechtold. In-situ shrinkage measurements of LTCC multilayers by means of an optical dilatometer. *Euro Ceramics VII, Pt 1-3*, 206-2:1281–1284, 2002.

[154] K.R. Mikeska, D.T. Schaefer, and R.H. Jensen. Method for reducing shrinkage during firing of green ceramic bodies - Patent 5085720, February 1992.

[155] S. Y. Tzeng and J. H. Jean. Stress development during constrained sintering of alumina/glass/alumina sandwich structure. *Journal of the American Ceramic Society*, 85(2):335–340, February 2002.

[156] J. Bang and G. Q. Lu. Densification kinetics of glass-films constrained on rigid substrates. *Journal of Materials Research*, 10(5):1321–1326, May 1995.

[157] R. Z. Zuo, E. Aulbach, and J. Rödel. Shrinkage-free sintering of low-temperature cofired ceramics by loading dilatometry. *Journal of the American Ceramic Society*, 87(3):526–528, March 2004.

[158] M. Hintz, H. Thust, and E. Polzer. Generic investigation on 0-shrinkage processed LTCC. In *IMAPS Nordic Conference*, 2002.

[159] ASTM C 20. Standard test method for apparent porosity, water adsorption, apparent specific gravity and bulk density of burned refractory brick and shapes by boiling water, 1992.

[160] E. Aulbach, R. Zuo, and J. Rödel. Laser-assisted high-resolution loading dilatometer and applications. *Experimental Mechanics*, 44(1):71–75, February 2004.

[161] ASTM D 4284. Pore volume distribution of catalysts by mercury intrusion porosimetry, 1992.

[162] ASTM C 1259. Standard test method for dynamic Young´s modulus, shear modulus, and Poisson´s ratio for advanced ceramics by impulse excitation of vibration, 1998.

[163] S. Sakaguchi, N. Murayama, Y. Kodama, and F. Wakai. The Poisson's ratio of engineering ceramics at elevated-temperature. *Journal of Materials Science Letters*, 10(5):282–284, March 1991.

[164] A. Vagnon, O. Lame, D. Bouvard, M. Di Michiel, D. Bellet, and G. Kapelski. Deformation of steel powder compacts during sintering: Correlation between macroscopic measurement and in situ microtomography analysis. *Acta Materialia*, 54(2):513–522, January 2006.

[165] P. J. Withers and J. J. Lewandowski. Three-dimensional imaging of materials by microtomography. *Materials Science and Technology*, 22(9):1009–1010, September 2006.

[166] T. S. Yeoh, N. A. Ives, N. Presser, G. W. Stupian, M. S. Leung, J. L. MacCollum, and F. W. Hawley. Focused ion beam tomography of a microelectronic device with sub-2-nm resolution. *Journal of Vacuum Science & Technology B*, 25(3):922–925, May 2007.

[167] O. Guillon, J. Rödel, and R. K. Bordia. Effect of green-state processing on the sintering stress and viscosity of alumina compacts. *Journal of the American Ceramic Society*, 90(5):1637–1640, May 2007.

[168] I. O. Ozer, E. Suvaci, B. Karademir, J. M. Missiaen, C. P. Carry, and D. Bouvard. Anisotropic sintering shrinkage in alumina ceramics containing oriented platelets. *Journal of the American Ceramic Society*, 89(6):1972–1976, June 2006.

[169] O. Gillia, C. Josserond, and D. Bouvard. Viscosity of WC-Co compacts during sintering. *Acta Materialia*, 49(8):1413–1420, May 2001.

[170] G. W. Scherer. Sintering inhomogeneous glasses - Application to optical-waveguides. *Journal of Non-Crystalline Solids*, 34(2):239–256, 1979.

[171] T. C. T. Ting and T. Y. Chen. Poisson's ratio for anisotropic elastic materials can have no bounds. *Quarterly Journal of Mechanics and Applied Mathematics*, 58:73–82, February 2005.

[172] J. Chang, S. J. L. Kang, O. Guillon, and J. Rödel. Characterization of warpage behavior of Gd-doped ceria/NiO-YSZ bi-layer samples for SOFC application. *To be published.*

[173] J. Kanters. *Sinterverhalten von Verbunden aus nanokristallinem Zirconiumdioxid.* PhD thesis, TU Darmstadt, 2000.

[174] J. N. Calata, A. Matthys, and G. Q. Lu. Constrained-film sintering of cordierite glass-ceramic on silicon substrate. *Journal of Materials Research*, 13(8):2334–2341, August 1998.

[175] D. Ravi and D. J. Green. Sintering stresses and distortion produced by density differences in bi-layer structures. *Journal of the European Ceramic Society*, 26(1-2):17–25, 2006.

[176] T. Ostrowski and J. Rödel. Evolution of mechanical properties of porous alumina during free sintering and hot pressing. *Journal of the American Ceramic Society*, 82(11):3080–3086, November 1999.

[177] Y. C. Lin and J. H. Jean. Constrained densification kinetics of alumina/borosilicate glass plus alumina/alumina sandwich structure. *Journal of the American Ceramic Society*, 85(1):150–154, January 2002.

[178] J. N. Calata, G. Q. Lu, and T. J. Chuang. Constrained sintering of glass, glass-ceramic and ceramic coatings on metal substrates. *Surface and Interface Analysis*, 31(7):673–681, July 2001.

[179] A. Mohanram, S. H. Lee, G. L. Messing, and D. J. Green. Constrained sintering of low-temperature co-fired ceramics. *Journal of the American Ceramic Society*, 89(6):1923–1929, June 2006.

[180] O. Guillon, E. Aulbach, J. Rödel, and R. K. Bordia. Constrained sintering of alumina thin films: Comparison between experiment and modeling. *Journal of the American Ceramic Society*, 90(6):1733–1737, June 2007.

List of Figures

List of Tables

Eidesstattliche Erklärung

Hiermit versichere ich an Eides Statt, dass ich die vorliegende Dissertation selbständig und nur unter Verwendung der angegebenen Hilfsmittel angefertigt habe. Von mir wurde weder an der Technischen Universität Darmstadt noch an einer anderen Hochschule ein Promotionsversuch unternommen.

Darmstadt, den 21.05.2008

Jean-Baptiste Ollagnier

Curriculum Vitae

EMPLOYMENT HISTORY

Feb. - Aug. 2004: Internship as an engineer in Sandvik Coromant (cutting tools supplier) - RD department, Stockholm - Sweden.
Project: Influence of milling parameters on SiAlON properties.

Summer 2001: Internship working for Valeo (automotive supplier), Móstoles - Spain.

EDUCATION AND QUALIFICATIONS

Sept. - Dec. 2006: Visiting researcher at Penn State University, Pennsylvania, USA.

Dec. 2004 - Mai 2008: PhD student at the Technical University of Darmstadt, Germany.

Sept. - Dec. 2003: Research project at the Luleå Technical University (LTU), Sweden.
Synthesis of the MAX phase Ti_3SiC_2.

Feb. - June 2003: Barcelona School of Engineering (ETSEIB: Escuela Técnica Superior de Ingeniería Industrial de Barcelona), Spain.

1999 - 2004: European School of Materials Science and Engineering - Master's degree
(EEIGM: Ecole Européenne d'Ingénieurs en Génie des Matériaux) in Nancy, France.

1996 - 1999: High school "Edouard Branly" in Lyon, France.

REFEERED PUBLICATIONS

J.-B. Ollagnier, O. Guillon, J. Rödel, "Viscosity of LTCC Determined by Discontinuous Sinter-Forging", Int. J. Appl. Ceram. Technol. 3 [6], 437-441 (2006)

J.-B. Ollagnier, O. Guillon and Jürgen Rödel, "Effect of Anisotropic Microstructure on the Viscous Properties of an LTCC Material" J. Am. Ceram. Soc., 90 [12] 3846-3851 (2007)

ORAL PRESENTATION

J.-B. Ollagnier, O. Guillon, J. Rödel, "Discontinuous Sinter-Forging of a Glass-Ceramic Composite Used in LTCC Technology", CICMT, Grand Hyatt Hotel, Denver, Colorado USA, April 24-27, 2006.

POSTERS

J.-B. Ollagnier, O. Guillon, J. Rödel, A. Wonisch, T. Kraft, M. Rauscher, A. Roosen, "Anisotropy development during sintering of a glass-ceramic composite used in the LTCC technology", Euromat, Nürnberg, Germany, September 10-13, 2007.

J.-B. Ollagnier, O. Guillon, J. Rödel, "Effect of the degree of constraint on densification and microstructure of LTCC films", CICMT, München, Germany, April 21-24, 2008.